# MODELING AND CONTROL OF BOOST CONVERTERS WITH APPLICATION TO ENERGY HARVESTING

by

Reza Sabzehgar

M.Sc., Amirkabir University of Technology (Tehran Polytechnic), 2001

A Thesis submitted in partial fulfillment
of the requirements for the degree of

Doctor of Philosophy

in the
School of Engineering Science
Faculty of Applied Sciences


SIMON FRASER UNIVERSITY
Summer 2012

## APPROVAL

**Name:** Reza Sabzehgar

**Degree:** Doctor of Philosophy

**Title of Thesis:** Modeling and Control of Boost Converters with Application to Energy Harvesting

**Examining Committee:**

Dr. Behraad Bahreyni
Chair

---

Dr. Mehrdad Moallem, Senior Supervisor
Associate Professor, School of Engineering Science

---

Dr. Farid Golnaraghi, Supervisor
Professor, School of Engineering Science

---

Dr. Ahmad Rad, Supervisor, Supervisor
Professor, School of Engineering Science

---

Dr. Martin Ordonez, Internal Examiner
Assistant Professor, School of Engineering Science

---

Dr. Alireza Bakhshai, External Examiner
Associate Professor, Department of Electrical and Computer Engineering, Queen's University

**Date Approved:** August 7, 2012

# Partial Copyright Licence

# Abstract

In this thesis, we investigate the development of new control schemes for single- and three-phase boost-type converters and their application to energy conversion. The developed algorithms are utilized to efficiently convert energy from a source with an arbitrary voltage waveform to a DC link or a battery. This type of energy transfer is of great interest in energy conversion systems involving low frequency, time-varying input sources such as vibration energy harvesting and marine wave power. In such applications, the generated voltages are sporadic in the sense that the amplitudes and frequencies of the generated waveforms are time-varying and not known a-priori.

Motivated by these applications, first a single-phase boost converter is studied and the performance of the proposed controller in providing a resistive input behavior is experimentally verified. Next, the idea proposed for a single-phase converter is extended to a three-phase bridgeless boost-type converter. To this end, an averaged model of the three-phase converter is obtained and utilized in designing a feedback control scheme to enforce a resistive behavior across each phase of the converter. Similar to the single-phase system, the proposed controller does not require a-priori knowledge of the input waveform characteristics and can convert waveforms with time-varying frequencies and amplitudes into DC power by regulating the input resistances at each phase. The proposed solution enables real-time variation of the generator loading using high efficiency switching power devices. Numerical simulations and experimental results are presented that evaluate performance of the proposed modeling and feedback control scheme for the three-phase system.

Finally, an application involving energy regeneration for a mechanical suspension system is considered using a setup consisting of a mass-spring test rig attached to a mechanical shaker for single- and three-phase applications using a tubular DC permanent-magnet machine and rotary machine connected to an algebraic screw, respectively. The algebraic screw

converts the translational motion of mechanical vibrations into rotary motion that acts as a prime mover for the three-phase synchronous machine. The experimental results reveal that the boost circuit and proposed feedback controller can successfully provide regenerative damping for mechanical vibrations with high-efficiency power conversion.

*Index Terms*—Boost converters, Switching circuits, Maximum power transfer, Energy regeneration, AC-DC converters, Regenerative suspension, Energy harvesting.

*To my beloved wife, Masi, for her immeasurable support, encouragement, and patience*
*and to my little son, Aria, the joy of my life.*

*"The whole of science is nothing more than a refinement of everyday thinking"*

Albert Einstein

# Acknowledgments

I would like to express my gratitude to Dr. Mehrdad Moallem, my senior supervisor, who provided me the great opportunity to work as his graduate student. His advices on research issues, experimental verifications, and paper manuscripts, were substantial and absolutely invaluable. These years in the doctoral program filled with challenging classes, exciting projects, long evenings in the lab, and participation in conferences were greatly helpful in my professional development as a researcher in the area of power electronics and control.

I would like to thank Dr. Farid Golnaraghi and Dr. Ahmad Rad, members of my Ph.D. supervisory committee, for providing valuable comments that helped me to improve this work. Special thanks go to Dr. Golnaraghi for providing me with the experimental shaker setup for the regenerative suspension system.

I would also like to thank Dr. Martin Ordonez and Dr. Alireza Bakhshai, my examiners, for their evaluation of this thesis.

Many thanks go to my fellow graduate students at the Motion and Power Electronic Control Lab, who made these years easier and more enjoyable in the atmosphere of fellowship and camaraderie. Specially, I would like to thank Amir Maravandi for his work on algebraic screw and Nicholas C. Doyle for his help on the shaker setup and its measurement sensors.

I would also like to acknowledge funding by the Natural Sciences and Engineering Research Council of Canada (NSERC) through which this research was mainly funded.

Last but not least, my special thanks are to my wife, my son, and my family in Iran for their love, sacrifices, patience, support, and encouragement.

# Contents

# List of Tables

# List of Figures

# Chapter 1

# Introduction

## 1.1 Motivation for the Research

Energy harvesting is the process of capturing energy from different sources in the environment such as radio waves, traffic-induced vibrations in a bridge, and excess heat coming from an engine. These sources of ambient energy can be recycled using advanced technologies resulting in improved energy utilization. Ambient sources of energy can be classified into five categories including electromagnetic, thermal, radioactive, biomass, and kinetic energy. Harvesting kinetic energy in the form of ambient mechanical vibrations provides a means to extend the operation of battery-dependent systems. Over the past decade, a wide array of electrodynamic transducers have been proposed to convert mechanical vibrations into usable electrical energy [1]-[3]. Electrodynamic energy harvesters operate based on the principle of electromagnetic induction, whereby electrical energy is converted from mechanical energy into electrical energy through the relative motion between a permanent magnet and a coil [4]. Fewer moving parts, lower maintenance, and higher efficiency are some advantages of electrodynamic energy harvesters which make them good candidates in many renewable energy technologies such as marine wave [5]-[8], wind power [9]-[10], and regenerative suspension and braking [11]-[18]. Figure 1.1 shows a conceptual vehicle which harvests energy from different ambient sources such as wind, solar, vibration, and fly-wheel [19].

One of the most important design trade-offs in the implementation of kinetic energy harvesters involve the compromise between the system size, total harvested power, and

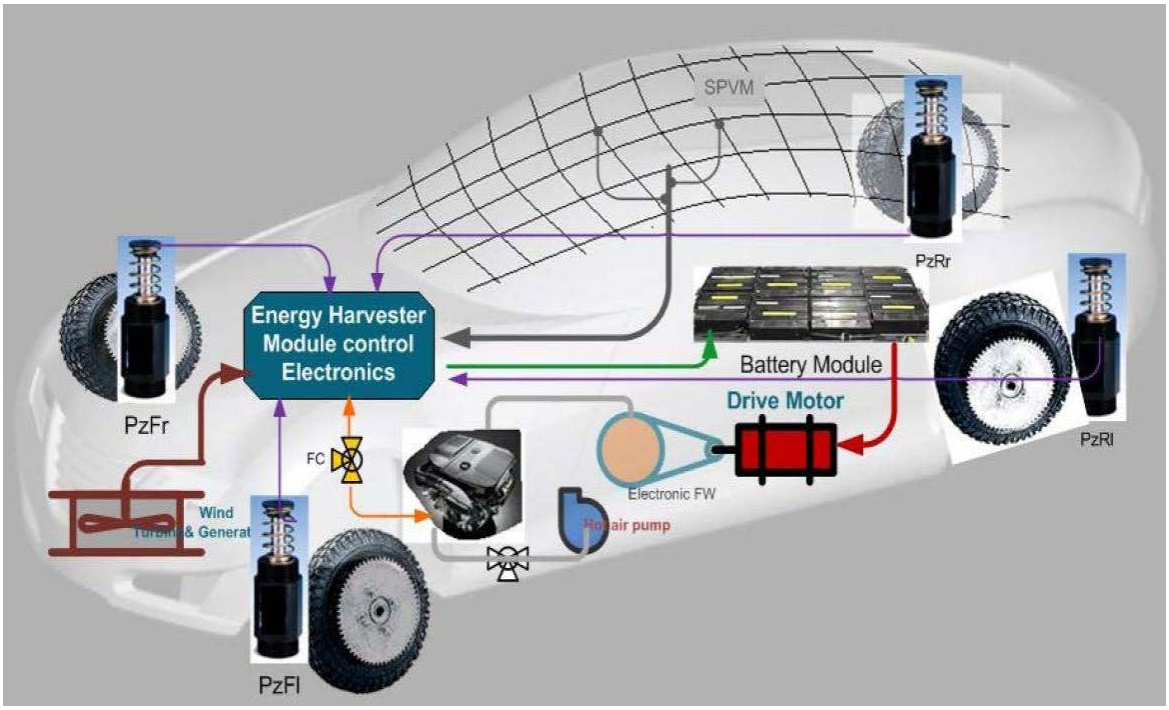


Figure 1.1: A conceptual vehicle with different energy harvesting modules [19].

cost. A functional energy harvesting system usually includes a power conditioning module and a storage element, which may be capacitor or rechargeable battery, as depicted in Figure 1.2. A power conditioning circuity is required since renewable energy sources do not usually produce deterministic voltage or current profiles and are time-varying in frequency and amplitude of the power waveforms. Thus, a critical component in renewable energy technologies is the need for an interface circuit between the harvester mechanism and the load to provide appropriate power management such as rectification, regulation, and impedance matching. In other words, since energy harvesting devices should process input power profiles with intermittent or time-dependent characteristics, specialized power electronic circuits are required to act as interfaces between the harvester and load.

Previous research on energy harvesting circuits have mainly focused on AC-DC converters based on the assumption of using sinusoidal input voltages/currents with known input frequencies. However, in energy harvesting applications, the generated input voltages and frequencies are time-varying and not known accurately in advance. Certain approaches have

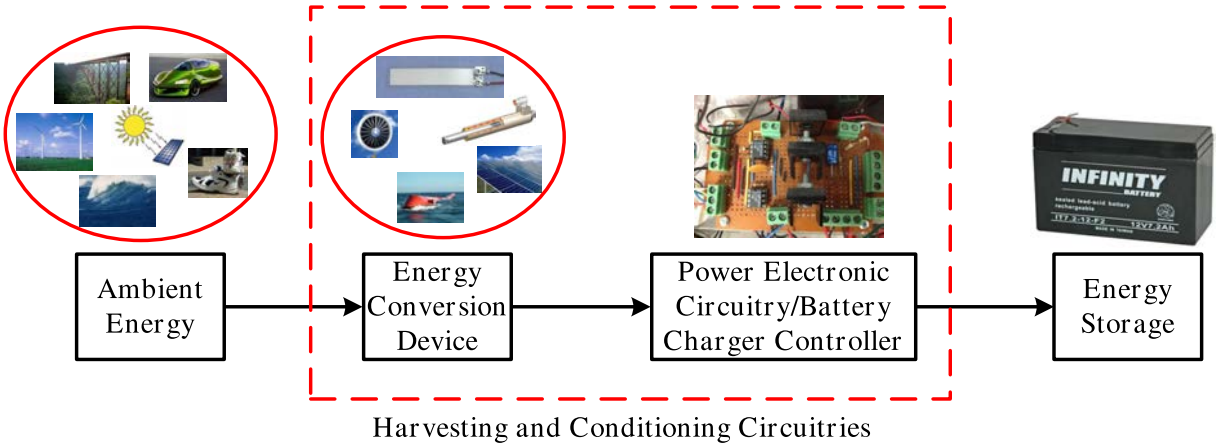


Figure 1.2: Schematic of energy harvesting systems.

been proposed to address power processing such as using more than one power converter in multi-channel converters [20]. However, these methods are not highly efficient due to unpredicted nature of renewable sources, cost of extra components, complicated controller, and high maintenance costs.

## 1.2 Background and Overview of the Present State of Technology

AC-DC conversion of electric power is widely used in many applications such as battery chargers, adjustable-speed drives, switch-mode power supplies, and uninterrupted power supplies. Conventional AC-DC converters, also known as rectifiers, have been developed using diodes or thyristors to provide uncontrolled and controlled DC power with unidirectional and bidirectional power flow [21]. In both types of rectifiers, the input current is highly distorted and the ratio of input voltage to the the input current is not constant. Also, the harmonic components injected into the power line would result in unfavorable effects for electricity consumers such as overheating of transformer windings and malfunctioning in the electrical devices connected to the grid. Therefore, conventional AC-DC conversion topologies are not favorable due to several drawbacks such as poor power quality, current harmonics, low efficiency, and large size of the required AC and DC filters.

To measure the quality of the power, a criterion called power factor, is defined for pure sinusoidal waveforms as the ratio of the real or active power flowing to the load to the apparent power in the circuit given by

$$Power\ Factor\ (PF) = \frac{Real\ Power\ (W)}{Apparent\ Power\ (VA)} \tag{1.1}$$

which is a dimensionless number between 0 and 1. Real power is the capacity of the circuit to perform work in a particular time interval. Apparent power is the product of the current and voltage across a load. Due to energy stored in the load and returned to the source, or due to a nonlinear load that distorts the current waveform, the apparent power will be greater than the real power. In the sinusoidal steady state, the power factor is defined as

$$PF = \frac{P}{S} \tag{1.2}$$

where $P$ is the real power (also known as active power) measured in watts (W), and $S$ is the apparent power measured in volt-amperes (VA). In the case of a pure sinusoidal waveform, $P$ and $S$ can be expressed as vectors that form a vector triangle such that

$$S^2 = P^2 + Q^2 \tag{1.3}$$

where $Q$ is the reactive power, measured in reactive volt-amperes (var). If $\phi$ is the phase angle between the input current and voltage, then the power factor is equal to the cosine of the angle $|\cos\phi|$ and

$$|P| = |S||\cos\phi| \tag{1.4}$$

Although, power factor is defined for purely sinusoidal waveforms, the same concept of keeping input voltage and current in the same phase, can be extended to an input waveform with multiple frequencies to improve the power quality. In cases where amplitude and frequency may vary, a proportional relationship between voltage and current would be equivalent to a unity power factor in the sinusoidal domain.

To adjust the power factor, different power factor correction (PFC) methods have been suggested which can be broadly classified into passive and active categories. Passive techniques [22]-[30] utilize an input filter, consisting of passive components (inductors and capacitors) to reduce line current harmonics caused by the diode rectifier. However, improvements that can be achieved by this method are relatively limited. Another drawback of the passive

PFC technique is the requirement for a relatively large size and weight of the filter inductor and capacitor. Besides, the passive filter may not respond adequately if the load power factor changes. On the other hand, active PFC techniques based on switch mode power converters (SMPC) are regarded as more efficient solutions. These devices utilize controlled solid-state switches in association with passive elements such as resistors, inductors, and capacitors [31]- [42].

Switch mode power converters convert the input voltage to another voltage level, by storing the input energy temporarily and then releasing that energy into the output at a different voltage. This switched-mode conversion is of particular interest due to the fact that it can result in high-efficiency power conversion. Power is controlled by controlling the timing of electronic switches in the "on" and "off" states. All basic switch mode power converter topologies such as boost, buck, buck-boost, and their variations can be used to realize active PFC techniques. At lower power ratings, metal-oxide-semiconductor field-effect transistors (MOSFETs) are the switching power devices of choice because of their low conduction losses and high switching speed. For medium- and high-power applications, insulated gate bipolar transistors (IGBTs) can be used in PWM-controlled converters with switching frequencies up to 30kHz.

Among different SMPCs [33]-[34], the boost topology is by far more popular than others in PFC applications because of its advantages such as simplicity, high power factor, low harmonic distortion, and high conversion efficiency when compared to the other topologies. A boost converter (step-up converter) is a switch mode power converter with an output DC voltage greater than its input DC voltage. It contains at least two semiconductor switches (a diode and a transistor) and at least one energy storage element. The boost PFC converter draws continuous current from the line and does not require much filtering, which is usually accomplished by an input filter capacitor. However, other topologies such as buck, buck-boost, and flyback draw pulsed current and need much better input filters. As a result, a more robust input filter must be employed to suppress the high-frequency components of the pulsating input current, which increases the overall weight and cost of the rectifier. A theoretical study of switching power converters with power factor correction is presented in [43]-[44] in which conditions for resistive behavior were discussed in an open-loop sense.

To address issues such as robustness, power density, efficiency, cost, and complexity, numerous AC-DC boost-type topologies have been proposed [45]-[46]. Also, some issues of traditional PFC converters such as the reverse recovery time of the boost diode have

been addressed in [47]-[50]. The proposed topologies include conventional boost converter (CBC) [51], symmetrical and asymmetrical bridgeless boost converters (SBBC and ABBC) [52]-[53], interleaved boost converter (IBC) [54]-[58], half- and full-bridge boost converter (HBBC and FBBC) [59]-[60], three-level boost converter (3LBC and B3LBC) [61]-[62], and regular and voltage doubler boost converter using a three-state switching cell (BC3SSC and VDBC3SSC) [63]-[66]. Figure 1.3 depicts different boost-type topologies. As shown in Figure 1.3-a, the conventional boost converter [51] uses a dedicated diode bridge to rectify the AC input voltage to DC followed by a boost section. Thus, the current always flows through three semiconductor elements, which are the two diodes of the diode bridge in series with boost diode $D_b$, or boost switch $S$, depending on the state of $S$, resulting in significant conduction losses. Therefore, the converter efficiency is compromised especially at low input voltages. To increase the efficiency of the conventional boost converter, bridgeless boost rectifiers (also known as dual boost converters) [52]-[53] have been introduced as shown in Figure 1.3-b,c which eliminate the input bridge rectifiers. The drive circuit of the main switches in Figure 1.3-b is less complex than that of Figure 1.3-c, since both switches are connected to the same reference node. However, it should be mentioned that this feature also eliminates the possibility of short-circuit through one leg due to possible malfunctioning of the main switches. The main disadvantage of bridgeless boost converter is the electromagnetic interference (EMI) and noise issues [67]-[68]. For a bridgeless PFC, the output voltage ground is always floating relative to the AC line input. Thus, all parasitic capacitance including MOSFET drain to earth and the output terminals to the earth ground contribute to common mode noise. To improve EMI noise in bridgeless boost converters, two slow diodes are added to the input line [67]. The added diodes have no effect on the efficiency of converter since they are in parallel with another semiconductor when they conduct. This solution will help to reduce the current stress on the MOSFETs in bridgeless configuration. As the power rating increases, it is often required to associate converters in series or in parallel to construct a new type of converters known as interleaved converters [54]-[58]. As illustrated in Figure 1.3-d, an interleaved PFC boost converter simply consists of two boost converters in parallel operating 180 degrees out of phase. The input current is then the sum of the two inductor currents. Since ripple currents of the inductors are out of phase, they tend to cancel each other and reduce the input ripple current caused by the boost inductors. Thus, interleaving can be used to increase conversion efficiency and power conversion density and reduce the ripple amplitude [55]. However, in interleaved converters,

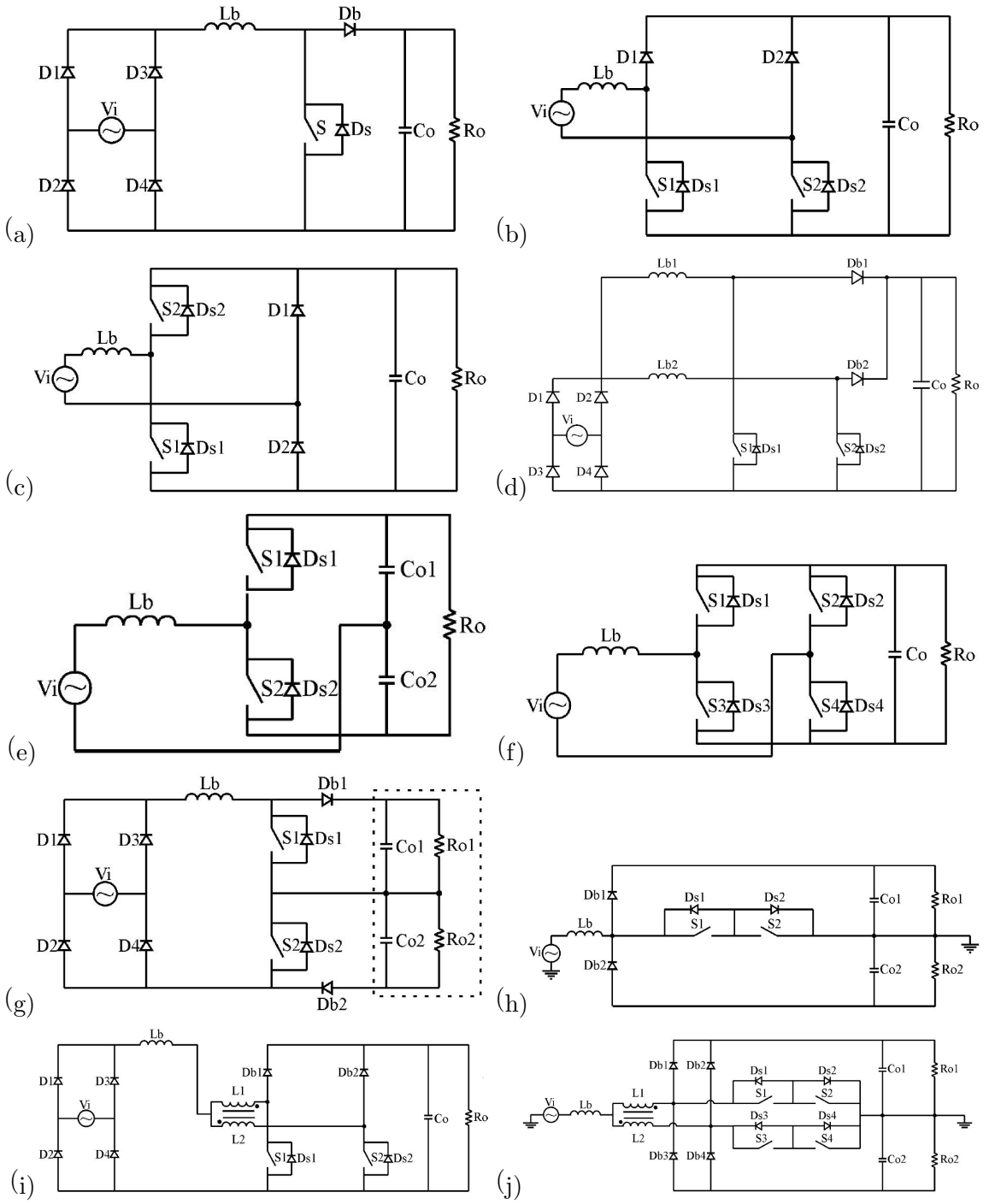


Figure 1.3: Different boost-type PFC topologies: (a) Conventional boost converter (CBC), (b) Symmetrical bridgeless boost converter (SBBC), (c) Asymmetrical bridgeless boost converter (ABBC), (d) Interleaved boost converter (IBC), (e) Half-bridge boost converter (HBBC), (f) Full-bridge boost converter (FBBC), (g) Three-level boost converter (3LBC), (h) Bridgeless three-level boost converter (B3LBC), (i) Boost converter using three-state switching cell (BC3SSC), (j) Voltage doubler boost converter using three-state switching cell (VDBC3SSC) [35].

the current is supposed to be adjusted to avoid overload, which makes the drive and control circuits more complex. Besides, the reverse recovery problem of boost diodes would still exist, which can be improved by operating in the discontinuous current mode (DCM) [56], or by using a passive snubber [58]. To further reduce the conduction losses, the half-bridge boost-type topology [59] shown in Figure 1.3-e can be utilized, where the current flows through only one switch during each operating stage, resulting in a significant reduction in the conduction losses. However, this topology suffers from imbalanced capacitor voltages, which may be caused due to DC offsets in the controller components or imbalanced loads connected in parallel with the capacitors. Therefore, a specific control loop is needed to mitigate the imbalanced voltage in the converter. To eliminate the need for this specific control loop, the full-bridge boost-type converter depicted in Figure 1.3-f has been proposed [60]. Although this structure is capable of processing higher power levels with bidirectional power flow, increased cost and complexity are distinct disadvantages due to the higher number of semiconductor elements. The three-level boost converter shown in Figure 1.3-g can also be used for high power applications as well as the interleaved boost converter [61]. From a practical point of view, a three-level boost converter is recommended for applications where the output voltage is around 400V or higher and the power level reaches some kilowatts. Furthermore, the current ripple frequencies of the three-level boost converter and the interleaved boost converter are twice as high as those of the conventional boost converter, which have a significant impact on the input filter size. To reduce the conduction losses and consequently to increase efficiency, the bridgeless three-level boost converter shown in 1.3-h can be utilized which has a reduced number of semiconductor devices due to the integration of the diode rectifier and the boost converter [62]. The three-state switching cell is similar to the interleaving of multiple cells but an autotransformer is used instead of one inductor per interleaved cell as depicted in Figure 1.3-i [63]-[65]. Since inductors in this topology are designed for twice the switching frequency, the size and weight of the converter is reduced. Moreover, the current through the switches is half of the input current. Thus, part of the input power is delivered to the load by the transformer instead of the main switches, resulting in smaller conduction and commutation losses. Also, lower cost switches can be utilized in this topology due to the possibility of parallelism of any number of cells. To further reduce the conduction losses, a bridgeless boost converter is utilized using three-state cell [66]. Table 1.1 summarizes some important characteristics of these converters considering the same current, voltage, power, and switching frequency ratings for all six categories [35].

Table 1.1: Comparison of some PFC boost-type converters

| **Parameter** | **CBC** | **SBBC** | **IBC** | **B3LBC** | **HBBC** | **VDBC3SSC** |
|---|---|---|---|---|---|---|
| Number of boost inductors | 1 | 1 | 2 | 1 | 1 | 1 |
| Size of each boost inductor | $L$ | $L$ | $L/2$ | $L$ | | $L/16$ |
| Total output voltage | $V_o$ | $V_o$ | $V_o$ | $2V_o$ | $V_o$ | $2V_o$ |
| Maximum number of semiconductor elements in the current path | 3 | 2 | 3 | 2 | 1 | 2 |
| Existence of diode bridge | Yes | No | Yes | No | No | No |
| Number of active switches | 1 | 2 | 2 | 2 | 2 | 4 |
| Number of boost diodes | 1 | 2 | 2 | 2 | 0 | 4 |

Referring to table 1.1, it is evident that each boost-type topology has its own pros and cons for a specific application. A bridgeless boost converter has been utilized in this thesis due to its advantages over the conventional boost converter such as less conduction losses and consequently higher efficiency [69]. In this topology, the series diode in the conventional boost-type topology is eliminated, which decreases the number of semiconductor devices. Moreover, the DC side inductor is moved to the AC side, which results in a reduction of the EMI noise.

A boost converter can operate in the continuous conduction mode (CCM), discontinuous conduction mode (DCM), or critical conduction mode (CRM). These terms are related to the continuity of the inductor current within the switching cycle. Figure 1.4 shows the boost inductor current of a typical converter in different modes of operation. The DCM operation of boost PFC converter is optimal for small-power applications [70]-[71], while the CCM operation is optimal for medium and high power applications in terms of cost and bulk components [36], [50], [72]-[73]. For a CCM boost PFC converter, both current control loop and voltage control loop are required. The current control loop is used to control the average input current of the converter to make it in the same shape and phase with the input voltage [74]-[75] whereas the voltage control loop is used to regulate the DC output voltage. In addition, mixed CCM/DCM and DCM operations can be used for a wide range of load variations [76]. However, high input-current distortion may still exist, requiring the use of large boost inductor to limit the input current distortion [77]. Moreover, mixed CCM/DCM and DCM operations affect the dynamics of the current control loop in CCM, which may result in poor current regulation and thus require modifications of the CCM current control law [70]. To achieve unity-power-factor operation without current control

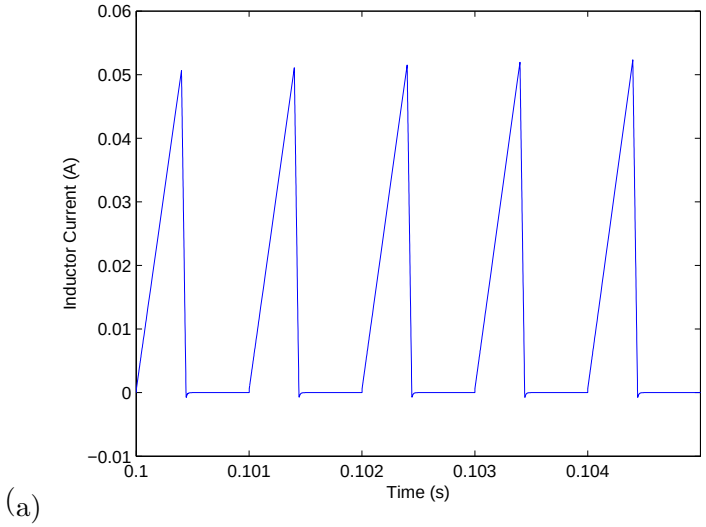


(a)

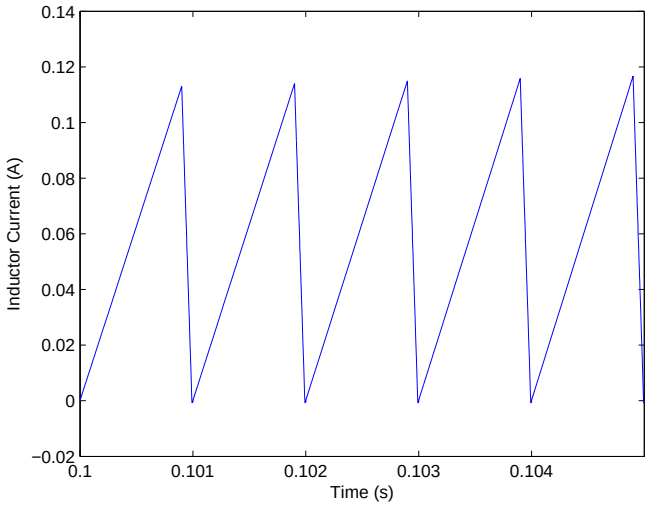


(b)

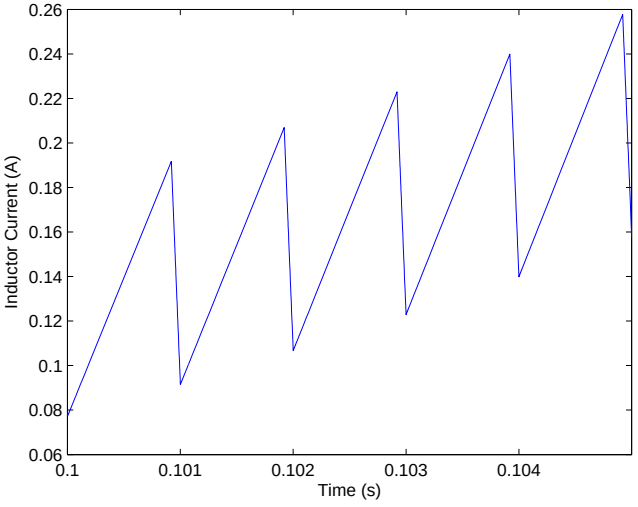


(c)

Figure 1.4: Boost inductor's current of a typical boost converter in different modes of operation: (a) Discontinuous conduction mode (DCM), (b) Critical conduction mode (CRM), (c) Continuous conduction mode (CCM).

loop, boost converter operating in the DCM has been proposed. In the steady state, the average input current of a DCM boost converter automatically follows the sinusoidal shape of the input voltage [78], thus making the DCM boost converter an inherent PFC converter. Compared with the CCM operation, DCM operation offers a number of advantages such as inherent PFC function, simple control, soft turn-on of the main switch, and reduced diode reversed-recovery losses due to soft turn-off of freewheeling diode. In other words, although in CCM operation the inductor current ripple is very small, which leads to low root-mean-square (rms) currents on the inductor and switch and low electromagnetic interference (EMI), the switch always operates in hard switching and the diode suffers from reverse recovery losses. However, in DCM operation the freewheeling diode is turned off softly and the switch is turned on at zero current, providing high efficiency. Nevertheless, the DCM operation requires a high-quality boost inductor since it must switch extremely high peak ripple currents and voltages due to the modulation of the inductor-current discharging time and high current stresses [79], which restrict the power range of single DCM boost PFC converter to lower power levels (below 250W) [70]. To increase the output power of DCM boost PFC converter, interleaved DCM boost PFC converter is recommended [80]. Also, to improve the performance of DCM boost converter at constant switching frequency, harmonic injection methods can be utilized [81], which results in high-quality input current at the cost of a complex control circuit. The approach based on variable switching frequency control can be also used for PFC boost converter operating in DCM [82]-[83]. However, since the switching frequency in this approach directly depends on the input-voltage and output-power, it requires a complex rectifier and control circuit design under a wide input voltage and output-power variation. The selected bridgeless boost converter used in this research is operated in the DCM due to the aforementioned advantages for low power applications.

Proper analytical models for DCM operation of PWM converters are therefore essential for the analysis and design of the converter. Such models could be used in designing the control systems, analysis of static and dynamic performance of the converter, and selection of the system parameters and components. Several authors have addressed the modeling issues in the DCM for PWM converters [84]-[85]. Averaging techniques are the most popular methods used for for analyzing the converter dynamic behavior and the design of a proper control loop. Several averaging techniques have been presented that are applicable to specific classes of power electronic circuits, such as the circuit averaging method [85]-[86], state-space averaging [87]-[89], switch averaging [90]-[91], sampled-data modeling [92]-[94],

and canonical averaging or loss-free resistor model [95]-[97]. Historically, the development of each averaging technique and the extensions thereof was motivated by a specific converter topology for which previous averaging techniques were inaccurate or cumbersome. In general, when a new converter topology is encountered, it is typically not clear as to which averaging technique or extension should be used for that converter. Consequently, substantial analytical effort is generally required to develop and implement the corresponding average-value model. Among the proposed averaging techniques, the circuit averaging and state-space averaging methods are quite popular and widely used. In the circuit averaging method, each semiconductor is replaced by either a controlled source voltage or a controlled source current, depending on its topological position in the converter circuit. The state-space averaging method is based on analytical manipulations using the different state representations of a converter. It consists of determining the linear state model for each possible configuration of the circuit and combining these elementary models into a single and unified model. As far as low-frequency modeling is concerned, both techniques are quite similar and provide identical results. They are quite simple and useful as far as the required behavior of the converter is limited to the low-frequency region. On the other hand, they provide no information concerning the induced high frequency phenomena and, therefore, cannot be used for electromagnetic compatibility analysis. Despite the limitations concerning their applicability, these methods provide simple tools for simulation and analysis of the power converters. To have a valid mathematical model in the entire frequency range, another modeling technique is used which is based on using the switching function concept [85], [98]. Although this method is more complex and time consuming than the averaging technique, this method does not neglect the high frequency operating regime and allows to study the switching effects and to analyze the electromagnetic compatibility of the converter. In this research, an averaged switch model of the DCM switch network is derived to represent the characteristics of the converter operating in the DCM.

## 1.3 Summary of Contributions and Outline of Dissertation

Extension of the above works to energy harvesting applications involving arbitrary band-limited sources of power such as wind, wave, and mechanical vibrations is not straightforward since the generated input voltages and frequencies are time-varying and not known accurately in advance. To achieve maximum power absorption in such cases, the idea presented

in this dissertation is to design a power conditioning system independent of input waveform characteristics through feedback control. In this regard, the contributions of this thesis are summarized as follows:

### 1.3.1 Chapter 2: Modeling and Control of a Single-Phase Boost Converter

This chapter lays the groundwork upon which the rest of the research was founded. First, the dynamic model of a single-phase bridgeless boost-type rectifier/charger is derived using averaging method. Motivated by certain requirements in energy harvesting applications, a feedback control scheme is then developed. It is shown that the circuit exhibits a nonlinear pseudo-resistive behavior as long as the duty cycle of the PWM control signal remains below a specific bound. The analytic expressions for pseudo-resistive behavior of the input are utilized to derive the feedback control law and corresponding component values and switching frequencies. Furthermore, performance of the converter with feedback control is demonstrated through simulation and experimental studies. The results indicate that by using model-based feedback control one can successfully enforce a *linear* resistive behavior between the input current and voltage with arbitrary waveforms. The value of input resistance can be changed by changing the desired resistance applied to the controller. The outcomes of research presented in this chapter were published in [99]-[100].

### 1.3.2 Chapter 3: A Regenerative Suspension System using a Tubular DC Permanent-Magnet Machine

Based on the modeling and analysis results developed for the single-phase charger presented in Chapter 2, we utilize the power converter along with the control scheme for vibration damping using a tubular DC permanent-magnet machine. To this end, the boost converter along with the proposed feedback control strategy is implemented on an energy regenerative suspension system testbed consisting of a mass, spring, and a linear DC machine. The model of the mass-spring system along with the linear DC machine is investigated when the system is vibrated using a shaker that can generate different frequencies in the low frequency band (a few Hz). The linear DC machine converts the vibration energy into electrical energy, due to the relative motion between its permanent magnet slider and stator winding. The model of regenerative damping system consisting of the linear DC machine is derived

and the condition under which the proposed damping system can harvest and transfer the maximum power to a DC media such as battery is investigated. It is shown that to transfer the maximum power to the load, there must be a resistive relationship between the input voltage and current of the power electronics interface. Thus, the boost converter circuit along with a feedback control strategy is utilized to enforce a resistive behavior between the DC machine output terminals. Furthermore, performance of the suspension system testbed is evaluated through experimental studies. The results indicate that the boost circuit and proposed feedback controller can successfully provide regenerative damping for mechanical vibrations with high-efficiency power conversion for the boost converter. The results presented in this chapter were published in [101]-[102].

### 1.3.3 Chapter 4: Modeling and Control of a Three-Phase Boost Converter

The modeling approach and control strategy developed in Chapter 2 is extended for a three-phase system due to the extensive use of three-phase machines in renewable generation systems such as variable speed wind and marine wave energy. To this end, the model of a three-phase bridgeless boost converter is derived that provides analytical expressions of the input characteristic of the converter. Based on this model, a novel feedback controller is designed to achieve a per-phase desired resistive input characteristic that can be adjusted to act as an apparent electric load on the generator. This feature can be used in maximum power transfer from the input power source in an impedance matching configuration. Furthermore, performance of the converter with feedback control is demonstrated through simulation and experimental studies for a low power conversion application using a dynamo system in the laboratory. The results indicate that one can successfully enforce a *linear* resistive behavior between each two phases of the input by using the proposed switching regime and control algorithm. The values of phase-to-phase resistances can be changed by changing the desired set points applied to the controller. The proposed solution enables real-time variation of the generator loading using high-efficiency switching power devices. The outcomes of research presented in this chapter were submitted to [103]-[104]. Moreover, the converter along with the modeling and control method have been filed as a US provisional patent [105].

### 1.3.4 Chapter 5: A Regenerative Suspension System using a Rotary Permanent-Magnet Machine

Based on the modeling and analysis results developed for the three-phase converter presented in Chapter 4, we utilize the power converter along with the control scheme for vibration damping using a rotary three-phase permanent-magnet machine. To this end, the boost converter along with the proposed feedback control strategy is implemented on an energy regenerative suspension system testbed consisting of a mass, spring, algebraic screw, and a rotary machine. The algebraic screw converts the linear motion of mechanical vibration into input torque for rotary DC machine resulting in generating electromagnetic force which acts as the damping force that can be electrically controlled by regulating the induced current. The model of regenerative damping system consisting of the rotary three-phase machine and algebraic screw is derived. The three-phase boost-type converter circuit along with a feedback control strategy is utilized for regenerative damping and its performance is verified through simulation and experiments.

### 1.3.5 Chapter 6: Summary, Conclusions, and Suggestions for Future Work

The research work accomplished in this thesis is summarized in this chapter. Based on the theoretical, simulation, and experimental studies, general conclusions concerning the outcome of this thesis are provided along with suggestions for future work.

# Chapter 2

# Modeling and Control of a Single-Phase Boost Converter

In this chapter, modeling and control of a single-phase bridgeless boost converter are presented. Prior research in this area has focused on boost converters based on the assumption of using sinusoidal input waveforms with known frequency and amplitude. The development of a boost-type switching converter as a battery charger for efficient power conversion from an arbitrary low-frequency input voltage waveform is thus presented in this chapter. The boost-type converter is modeled in Section 2.2 using the averaging method which results in a nonlinear input model. Based on the input model developed in Section 2.2, a feedback control scheme is proposed in Section 2.3 to achieve a desired input resistance. Section 2.4 presents simulation and experimental results which illustrate performance of the feedback control system. The results indicate that unity power factor operation for irregular and time-varying inputs is achievable through using the proposed feedback controller. Moreover, it is shown that by using the developed model-based feedback control scheme, a *linear* resistive behavior between the input current and voltage can be achieved. Finally, summary and conclusions are presented in Section 2.5.

## 2.1 Introduction

Operation under unity power factor is an important feature in AC-DC boost power converters. The basic topology of the conventional AC-DC PFC boost rectifier is shown in

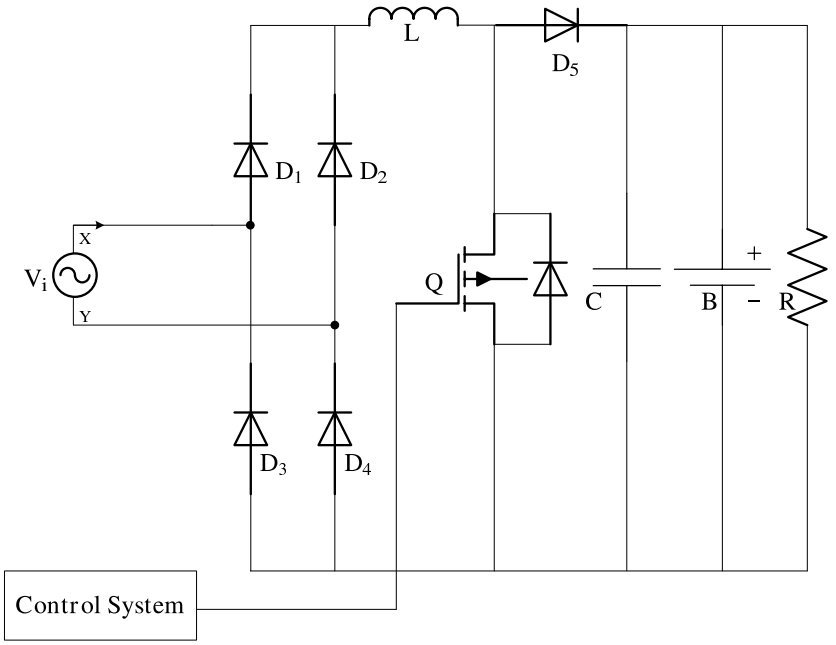


Figure 2.1: Conventional single-phase boost-type converter.

Figure 2.1. A great deal of research has been conducted on this converter aimed at minimizing power losses so that higher power conversion efficiency can be achieved. In an effort to improve the efficiency of the front-end PFC rectifiers, several power supply manufacturers and semiconductor companies have started looking into bridgeless PFC circuit topologies. Generally, bridgeless PFC topologies may reduce conduction losses by reducing the number of semiconductor components in the line current path. Compared to the conventional PFC boost rectifier (Figure 2.1) one diode is eliminated from the line-current path, so that the line current simultaneously flows through only two semiconductors, resulting in reduced conduction losses. Performance comparison between the conventional and the bridgeless PFC boost rectifier as well as loss analysis and experimental efficiency evaluation was presented in [69]. Several other researchers have studied bridgeless boost converters in terms of their efficiency and EMI noise analysis [106]-[108].

Previous research in this area has mainly focused on boost converters based on the assumption of using sinusoidal input waveforms, e.g., for power-line applications [75], [41] where the frequency and amplitude of input waveforms are a-priori known. In this chapter,

we propose a feedback control scheme based on a resistive model derived for a single-phase bridgeless boost converter as a battery charger. This feature enable the proposed system to be utilized for energy harvesting applications from arbitrary band-limited sources of power such as wind, wave, and mechanical vibrations, where the generated input voltages are not known accurately in advance.

## 2.2 Operating Principle and Circuit Analysis

The single-phase conventional and bridgeless boost converter considered in this chapter is shown in Figure 2.2 (see e.g., [69]). In the following, we provide a brief review of the circuit operation along with a derivation of the resistive behavior of the circuit. Referring to Figure 2.2, the Schottky diodes and MOSFETs are used to achieve low conduction losses.

To decrease the conduction losses, $Q_2$ is kept on when the time varying input voltage $v_i$ is positive. Similarly, $Q_1$ is turned on during the negative cycle of the input voltage. When $v_i > 0$ and $Q_1$ is on, the inductor current builds up and energy is stored in its magnetic field (Figure 2.3-a). We denote this case as mode 1 of operation. After $Q_1$ is turned off, the

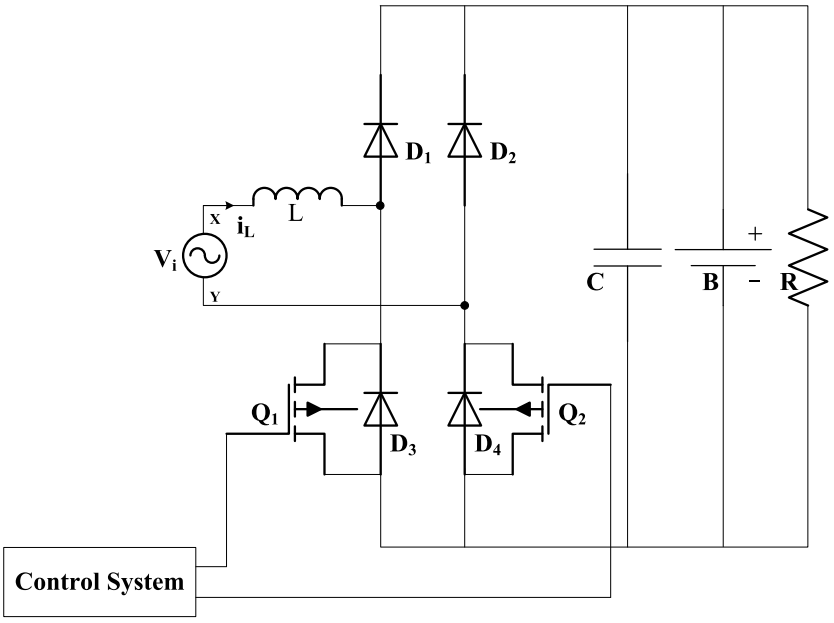


Figure 2.2: Single-phase bridgeless boost-type converter.

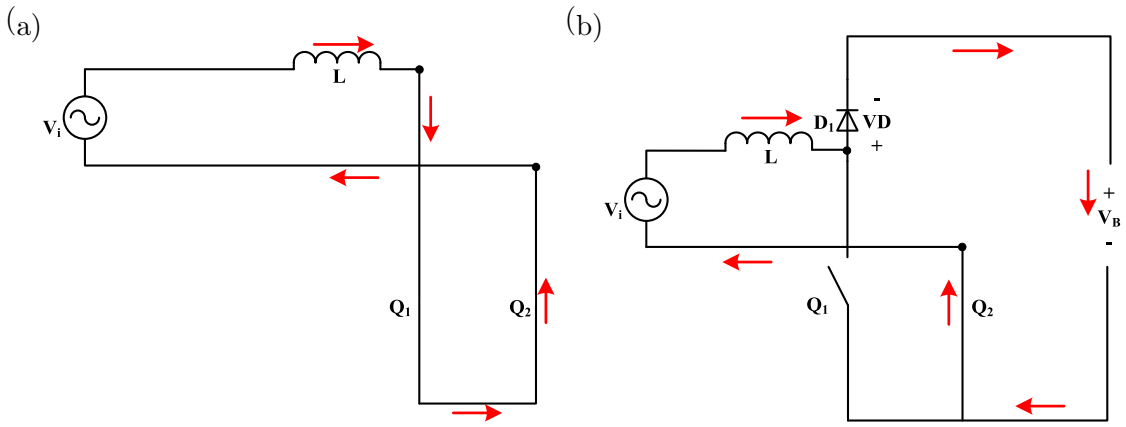


Figure 2.3: Operation modes in the positive cycle of input voltage (a) Mode 1 of circuit operation: Both $Q_1$ and $Q_2$ are ON, (b) Mode 2 of circuit operation: $Q_1$ is turned OFF and $Q_2$ remains ON.

stored energy in the inductor together with the energy coming from the input source charge the battery as depicted in Figure 2.3-b. We denote this case as mode 2 of operation of the circuit.

Let us now analyze the circuit when the input voltage $v_i$ is positive. A similar analysis can be given for negative input voltages. Based on the time intervals that MOSFETs $Q_1$ and $Q_2$ remain on and off, there are two different cases as follows.

### 2.2.1 Case I: $Q_1$ is OFF for a relatively long time

In this case, it is assumed that the off-time of $Q_1$ is large enough such that the inductor is completely discharged to zero current. The charging and discharging of the inductor is illustrated in Figure 2.4. In this figure, $t_{on}$ and $t_{off}$ are the time intervals that $Q_1$ remains on and off, respectively, and $T_s$ is the switching period of $Q_1$.

In mode 1 of operation, the inductor current can be written as follows

$$i_L(t) = i_L(t_1) + \frac{1}{L}\int_{t_1}^{t} v_i(t)dt, \quad t_1 \leq t \leq kT_s \tag{2.1}$$

In the following analysis, the MOSFET voltage drop is ignored when it is on. Since in this case the inductor is totally discharged, the current of the inductor would be zero before or just at the end of each switching cycle. Therefore, with no loss of generality, we assume

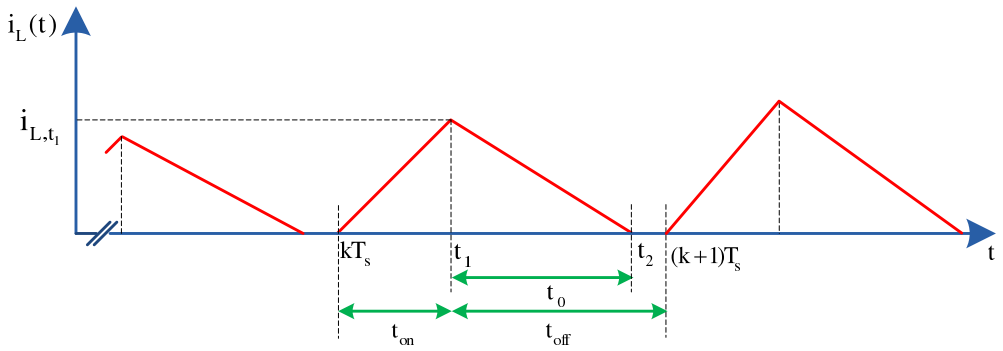


Figure 2.4: Inductor Current for Case I: $Q_1$ is OFF for a relatively long time.

$t_1$ is the start time of $k^{th}$ switching cycle such that $i_L(t_1) = 0$. Also, let us assume that, by design, we choose the switching frequency much higher than the frequency content of input source. Hence, $v_i(t)$ is approximately constant during $t_{on}$, i.e., $v_i(t) = v_i(kT_s)$, where $k$ is the sampling instant and $T_s$ is the switching period. Therefore, during $t_{on}$ (2.1) can be approximated as

$$i_L(t) = \frac{1}{L} v_{i,k}(t - t_1), \quad t_1 \leq t \leq kT_s \tag{2.2}$$

where $v_{i,k}$ is the value of input voltage $v_i$ at time $t = kT_s$.

In mode 2 of operation, the inductor current can be described by the following equation

$$i_L(t) = i_{L,k} + \frac{1}{L} \int_{kT_s}^{t} (v_i(t) - V_B - V_D)dt, \quad kT_s \leq t \leq t_2 \tag{2.3}$$

where $i_{L,k}$ represents the value of inductor current at time $t = kT_s$, $V_B$ stands for the battery voltage, and $V_D$ is the voltage drop across diode $D_1$. Again, the MOSFET voltage drop is ignored when it is on, and $v_i(t)$ is assumed to be approximately constant during $t_{off}$, i.e., $v_i(t) = v_i(kT_s)$. Using (2.2), $i_{L,k}$ is given as follows

$$i_{L,k} = \frac{1}{L} v_{i,k} t_{on}. \tag{2.4}$$

Substituting (2.4) into (2.3) results in

$$i_L(t) = \frac{1}{L} v_{i,k} t_{on} + \frac{1}{L}(v_{i,k} - V_B - V_D)(t - kT_s), \quad kT_s \leq t \leq t_2 \tag{2.5}$$

Referring to Figure 2.4, to find $t_0$, we set $i_L(t_2) = 0$. Hence

$$t_0 = \frac{v_{i,k} t_{on}}{V_B + V_D - v_{i,k}}. \tag{2.6}$$

Therefore, referring to Figure 2.4 it can be concluded that

$$\Delta q = \frac{1}{2} i_{L,k} t_{on} + \frac{1}{2} i_{L,k} t_0 \tag{2.7}$$

where $\Delta q$ is the total charge passing through the inductor in the interval $t_1 < t < t_1 + T_s$. By substituting (2.4) and (2.6) into (2.7), we have

$$\Delta q = \frac{1}{2L} v_{i,k} t_{on}^2 (1 - \frac{v_{i,k}}{v_{i,k} - V_B - V_D}) \cdot \tag{2.8}$$

Therefore, the average value of inductor current at instant $kT_s$, $\bar{i}_{L,k}$, can be written as

$$\bar{i}_{L,k} = \frac{\Delta q}{T_s} = \frac{1}{2L} \frac{t_{on}^2}{T_s} v_{i,k} (1 - \frac{v_{i,k}}{v_{i,k} - V_B - V_D}) \tag{2.9}$$

Equation (2.9) indicates that there exists a nonlinear resistance at each sampling time $t = kT_s$ between input terminals $XY$ (see Figure 2.2) given by

$$R_k = \frac{v_{i,k}}{\bar{i}_{L,k}} = \frac{2LT_s}{t_{on}^2} (1 - \frac{v_{i,k}}{V_B + V_D}) \cdot \tag{2.10}$$

It should be pointed out that there is a major difference between the above result and the loss-free resistive model given by [78]. In [78], the effective resistance is obtained across the switch element which is not a function of the input and output voltages of the converter and hence is *linear* with respect to the input and output voltages. In this work, we have obtained a nonlinear resistive behavior across the combination of the switch and inductor as given by 2.10 which will be compensated by utilizing an inversion-based controller as discussed in Section 2.3.

Due to the resistive nature of (2.10), there is no phase difference between $v_{i,k}$ and $\bar{i}_{L,k}$, if the circuit is operated in this mode. It must be noted that the time-varying part of $R_k$, i.e., $\frac{v_{i,k}}{V_B + V_D}$, is compensated by the feedback controller presented in Section 2.3. Next, we will obtain a condition to achieve the above resistive relationship between $v_{i,k}$ and $i_k$ based on the duty cycle of switching. Referring to Figure 2.4, the condition that should be satisfied is that the off-time of $Q_1$ must be large enough to let the inductor to be completely discharged, i.e., $t_0 \leq t_{off}$. Thus one can write $t_{on}$ and $t_{off}$ in terms of the duty cycle $d$ of PWM waveform as follows

$$\begin{aligned} t_{on} &= dT_s \\ t_{off} &= (1-d)T_s \end{aligned} \tag{2.11}$$

Using (2.11) and (2.6), we have

$$\frac{v_{i,k}dT_s}{V_B + V_D - v_{i,k}} \leq (1-d)T_s \tag{2.12}$$

which results in

$$d(V_B + V_D) \leq V_B + V_D - v_{i,k}. \tag{2.13}$$

Therefore, the condition to achieve resistive performance at the input can be obtained using the following equation

$$d \leq 1 - \frac{v_{i,k}}{V_B + V_D}. \tag{2.14}$$

The above relationship indicates that a *pseudo-resistive* behavior is achieved at a duty cycle that is independent of circuit elements, i.e., it only depends on the input voltage and voltage drop across the diode and battery.

### 2.2.2 Case II: $Q_1$ is OFF for a sufficiently short time

In this case, it is assumed that the off-time of $Q_1$ is small and the inductor cannot be discharged completely. Figure 2.5 shows the charging and discharging cycles of the inductor current. The inductor current in mode 1, when it is charging, can be written as follows

$$i_L(t) = i_L(t_3) + \frac{1}{L}\int_{t_3}^{t} v_i(t)dt, \quad t_3 \leq t \leq kT_s \tag{2.15}$$

In mode 2 of operation, the inductor current can be described by the following equation

$$i_L(t) = i_{L,k-1} + \frac{1}{L}\int_{(k-1)T_s}^{t} (v_i(t) - V_B - V_D)dt, \quad (k-1)T_s \leq t \leq t_3 \tag{2.16}$$

Using (2.16), we have

$$i_{L,t_3} = i_L(t_3) = i_{L,k-1} + \frac{1}{L}(v_{i,k-1} - V_B - V_D)t_{off}. \tag{2.17}$$

Substituting (2.17) into (2.15) results in

$$i_L(t) = i_{L,k-1} + \frac{1}{L}(v_{i,k-1} - V_B - V_D)t_{off} + \frac{1}{L}v_{i,k}(t - t_3), \quad t_3 \leq t \leq kT_s \tag{2.18}$$

Now, $i_{L,k}$ depicted in Figure 2.5 can be derived from (2.18) as follows

$$i_{L,k} = i_{L,k-1} + \frac{1}{L}(v_{i,k-1} - V_B - V_D)t_{off} + \frac{1}{L}v_{i,k}t_{on}. \tag{2.19}$$

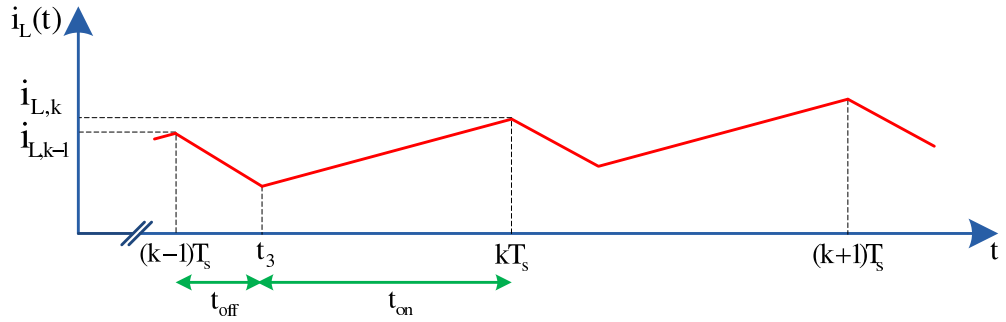


Figure 2.5: Inductor Current for Case II: $Q_1$ is OFF for a sufficiently short time.

From (2.19), it follows that

$$\Delta i_{L,k} = i_{L,k} - i_{L,k-1} = \frac{1}{L}(v_{i,k-1}t_{off} + v_{i,k}t_{on}) - \frac{1}{L}(V_B + V_D)t_{off}\cdot \tag{2.20}$$

Assuming that the input voltage does not change much in one sampling interval $T_s$, i.e., $v_{i,k-1} = v_{i,k}$, and utilizing (2.11), equation (2.20) can be used to approximate the slope of inductor current curve, i.e., $\frac{di_{L,k}}{dt}$, as

$$\frac{di_{L,k}}{dt} = \frac{1}{L}v_{i,k} - \frac{1}{L}(V_B + V_D)(1-d)\cdot \tag{2.21}$$

Therefore, the relationship between input voltage $v_{i,k}$ and input current $i_{L,k}$ at time $t = kT_s$ is given by

$$v_{i,k} = L\frac{di_{L,k}}{dt} + (V_B + V_D)(1-d)\cdot \tag{2.22}$$

Thus, when $d$ is large enough, e.g., for $d = 1$ corresponding to $t_{off} = 0$, the input voltage and current would have a phase difference of 90 degrees since the circuit would act like a pure inductance. In summary, the circuit exhibits a *pseudo-resistive* behavior between points $X$ and $Y$ in Figure 2.2, as long as $d$ remains below the bound given by (2.14), whereas for $1 - \frac{v_{i,k}}{V_B+V_D} < d < 1$, the circuit will behave as a pure inductor with a DC bias which varies based on the duty cycle as described by (2.22).

## 2.3 Proposed Control Strategy

Based on (2.10), the parameters that can significantly affect the value of input resistance $R_k$ are $T_s$, $t_{on}$, and $L$. The switching period $T_s$ cannot generally be a proper control variable.

Thus, $t_{on}$ has to be used as the control input which can be related to $d$. To this end, let us define $u$, $a$ and $y$ as follows

$$u = \frac{2LT_s}{t_{on}^2}, \quad a = V_B + V_D, \quad y = \frac{v_{i,k}}{i_{L,k}} \tag{2.23}$$

where $u$ and $a$ are both positive ($u > 0$, $a > 0$). Equations (2.10) and (2.23) result in

$$y = u(\frac{a - v}{a}) \tag{2.24}$$

where $v = v_{i,k}$.

Now, let us define

$$u = y_d + \Delta u \tag{2.25}$$

where $y_d$ is the desired input resistance of the circuit. Substituting (2.25) into (2.24) results in

$$y = (y_d + \Delta u)(1 - \frac{v}{a})\cdot \tag{2.26}$$

By defining $e = y_d - y$ and using (2.26), we have

$$e = \frac{v}{a}y_d - \Delta u(1 - \frac{v}{a})\cdot \tag{2.27}$$

Now, let us take the control input $\Delta u$ as follows

$$\Delta u = (1 - \frac{v}{a})^{-1}(w + \frac{v}{a}y_d) \tag{2.28}$$

where $w$ is the output of a PI controller given by

$$w = K_p e + K_I \int e dt\cdot \tag{2.29}$$

Substituting (2.28) into (2.27) and using (2.29) results in

$$(K_p + 1)e + K_I \int e dt = 0 \tag{2.30}$$

Since the coefficients of the PI controller are always positive, $K_I/(K_P+1)$ is always positive, which guarantees that the error would exponentially converge to zero. It should also be noted that the above ratio specifies the convergence speed of the controller. By increasing this value reasonably, the controller is able to compensate the uncertainties caused by the nonlinear term on the input resistance given by (2.10). However, if the $K_I/K_P$ ratio is

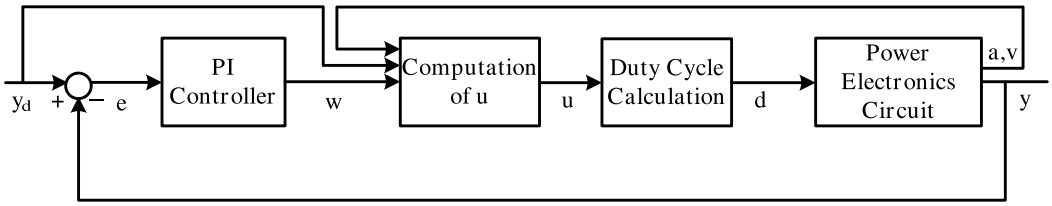


Figure 2.6: Block diagram of proposed control strategy.

increased too much, it may have a destabilizing effect due to the unmodeled dynamics. This ratio is set to 4000 ($K_I = 40$, and $K_P = 0.01$) for the experimental setup used in this study. The control law is then obtained by substituting (2.28) into (2.25) as follows

$$u = y_d + (1 - \frac{v}{a})^{-1}(w + \frac{v}{a}y_d) \tag{2.31}$$

which can be further simplified to

$$u = \frac{a}{a - v}(y_d + w)\cdot \tag{2.32}$$

The value of duty cycle, $d$, is then calculated using (2.23) and $u$ given by (2.32) at each time instant. Figure 2.6 illustrates the control system block diagram in which the control input is generated by a PWM signal with the duty cycle determined by the controller.

## 2.4 Simulation and Experimental Results

A Simulink model of the proposed converter and its controller were developed using the SIMELECTRONICS toolbox of MATLAB with the following parameters: $L = 0.1H$, $C = 100\mu F$, $R = 1k\Omega$, $V_B = 12V$, $V_D = 0.6V$, $v_i(t) = 3\sin(2\pi f_i t)V$, $f_i = 2Hz$, $f_s = 1kHz$, and $y_d = 5k\Omega$; where $f_i$ and $f_s$ are input signal and switching frequencies, respectively.

Figure 2.7 illustrates the variation of input resistance versus PWM duty cycle using simulation and the resistive formula given by (2.10). The PWM duty cycles are below the bound given by (2.14) (i.e., $d \leq 76\%$); hence the circuit operates in the pseudo-resistive mode. Figure 2.7 shows that simulated values are close to corresponding theoretical values obtained from (2.10).

The proposed controller is utilized to achieve the desired resistance by changing the duty cycle of PWM signals. Since $\frac{a}{a-v}$ is close by unity, this term is assumed to be one in controller implementation.

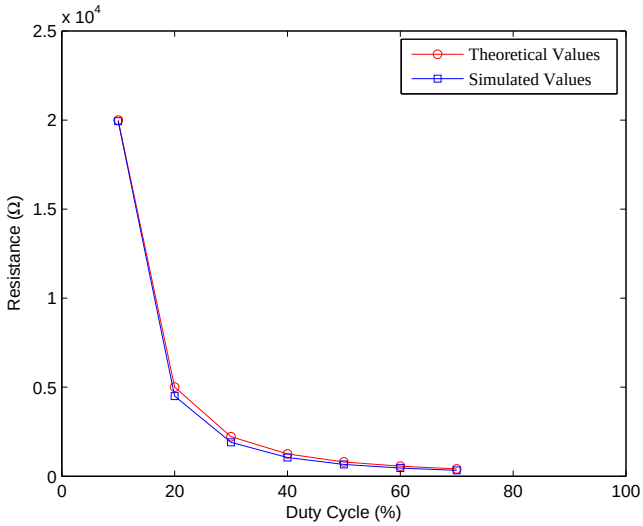


Figure 2.7: Theoretical and simulated values of circuit resistance seen from the input voltage source.

From Figure 2.8-a, it is evident that there is no phase difference between input voltage and current which is achieved by tuning the duty cycle of PWM signal. Considering (2.10) and ignoring the term $\frac{v_{i,k}}{v_B+v_D}$, which is typically small for a boost converter, results in $R_k = 5K\Omega$, when the duty cycle of the PWM control signal is 25%. Figure 2.8-b shows that the duty cycle is oscillating around 25%. This oscillation is because of the time varying part in equation (2.10) due to $\frac{v_{i,k}}{v_B+v_D}$.

Figure 2.9 illustrates performance of the proposed controller in achieving pseudo-resistive behavior for a multi-frequency input source with varying amplitude.

Figure 2.10 shows the simulation results for $d = 99\%$ which indicates almost 90 degrees phase difference between input voltage and input current. Thus the circuit behaves as an inductive circuit for duty cycles between 76% and 100%.

To evaluate performance of the circuit experimentally, the circuit shown in Figure 2.2 was implemented as shown in Figure 2.11. The following components were used: $Q_1$, $Q_2$: N-channel MOSFETs, $75V, 90A$ (IRFP2907) [109] with internal diodes $D_3$ and $D_4$; $D_1$, $D_2$: Schottky diodes, $60V, 20A$ (MBR4060WT) [110]; $B$: Sealed lead acid battery, $12V, 7Ah$; $C$: Electrolyte capacitor, $100\mu F, 25V$; $L$: $0.1H$; $R$: $1K\Omega$.

The current signal passing through the inductor, and the input voltage are measured,

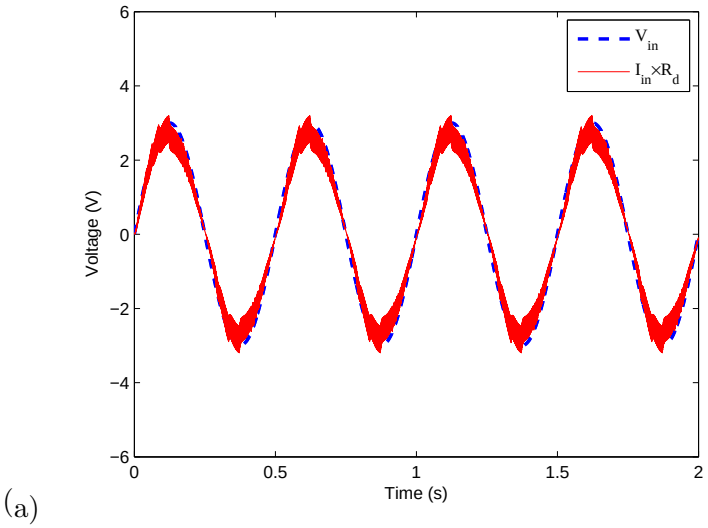


(a)

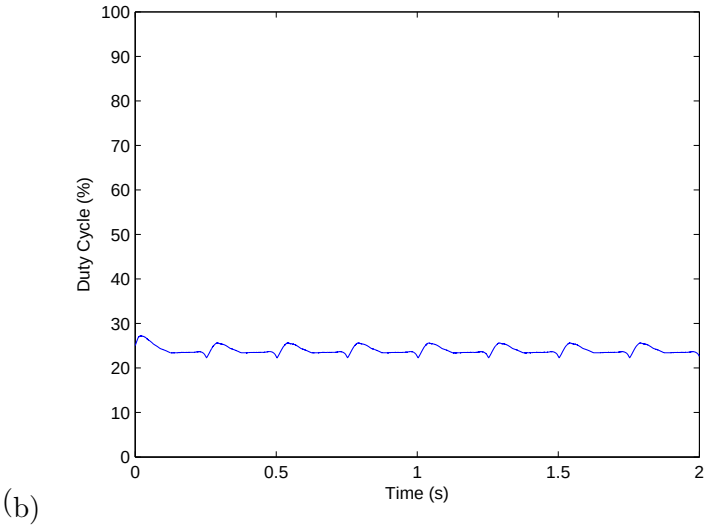


(b)

Figure 2.8: Simulated waveforms for a sine wave input source: (a) Input voltage and input current multiplied by the value of desired resistance ($R_d = 5k\Omega$), (b) Duty cycle of PWM signal.

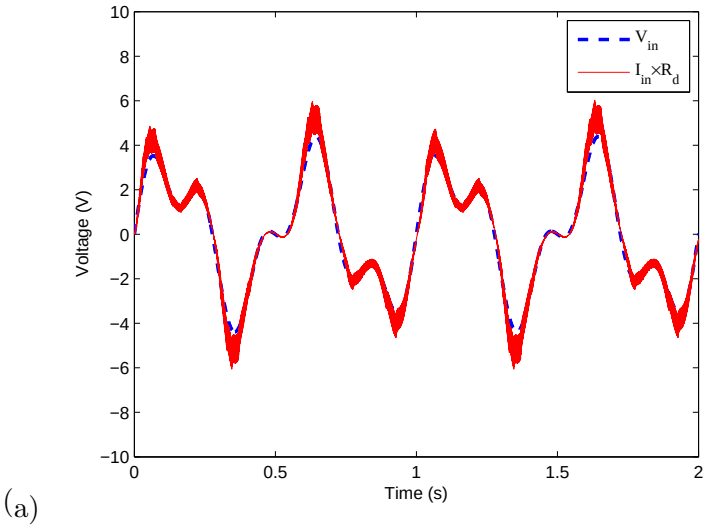


(a)

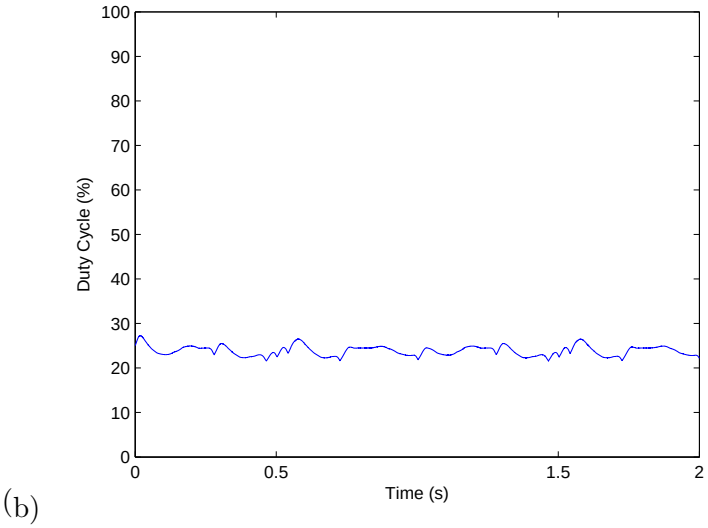


(b)

Figure 2.9: Simulated waveforms for a multi-frequency input signal with varying amplitude: (a) Input voltage and input current multiplied by the value of desired resistance ($R_d = 5k\Omega$), (b) Duty cycle of PWM signal.

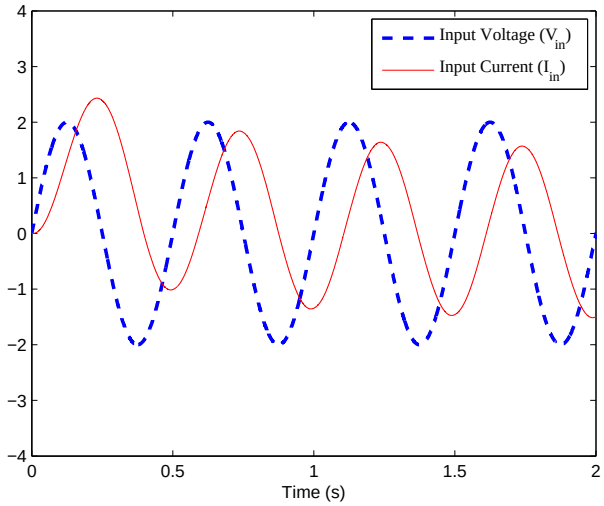


Figure 2.10: Simulation results showing inductive behavior of the circuit.

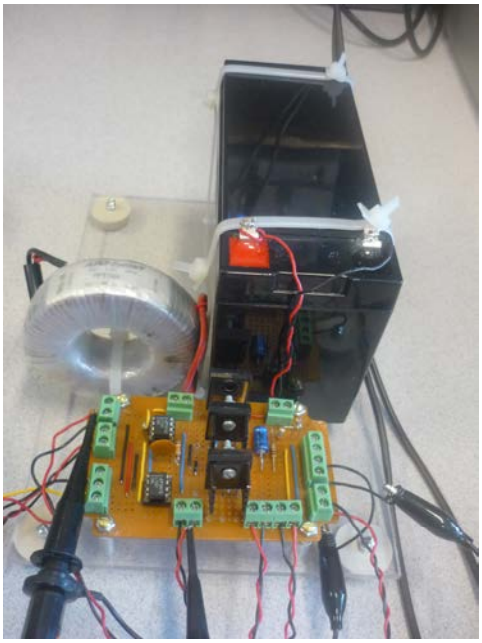

Figure 2.11: Implementation of the circuit in Figure 2.2.

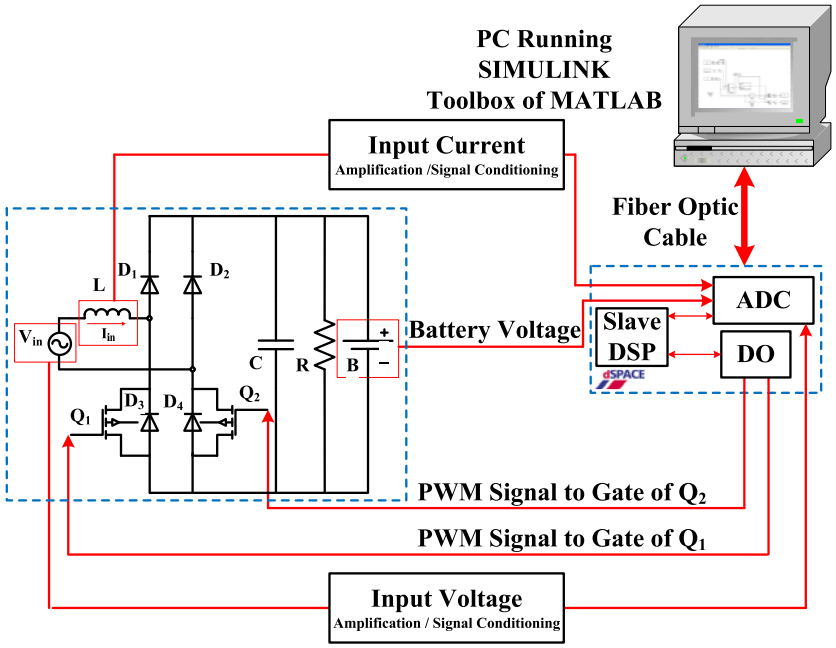


Figure 2.12: Block diagram of experimental setup.

amplified, and isolated using two LT1167 instrumentation amplifiers. These two signals along with the battery voltage are then captured by ADC channels of dSPACE 1103 (from *dSPACE, Inc.* [111]). These data are then transferred to a PC workstation running MATLAB/SIMULINK through a fiber optic cable connecting dSPACE controller to the PC. The circuit resistance seen from input voltage source ($y$) is then calculated by dividing captured input voltage over inductor current. The controller is implemented on a dSPACE DSP board using the MATLAB Real-Time Workshop. The PWM signal is generated based on the value of $d$ obtained from (2.29), (2.32), and (2.23) at each sampling instant. Figure 2.12 depicts a block diagram of the experimental setup along with its feedback controller. Figure 2.13 shows the experimental setup.

A $2Hz$ sine wave signal is applied to the experimental setup with the desired input resistance set to $5K\Omega$. The results using feedback controller are shown in Figure 2.14.

The performance of the controller was then investigated by applying a multi-frequency input signal $v_i(t) = 3\sin(4\pi t) + 1.5\sin(10\pi t)$ for an input resistance of $5k\Omega$. The results are shown in Figure 2.15 which indicate that the input current follows the input voltage with

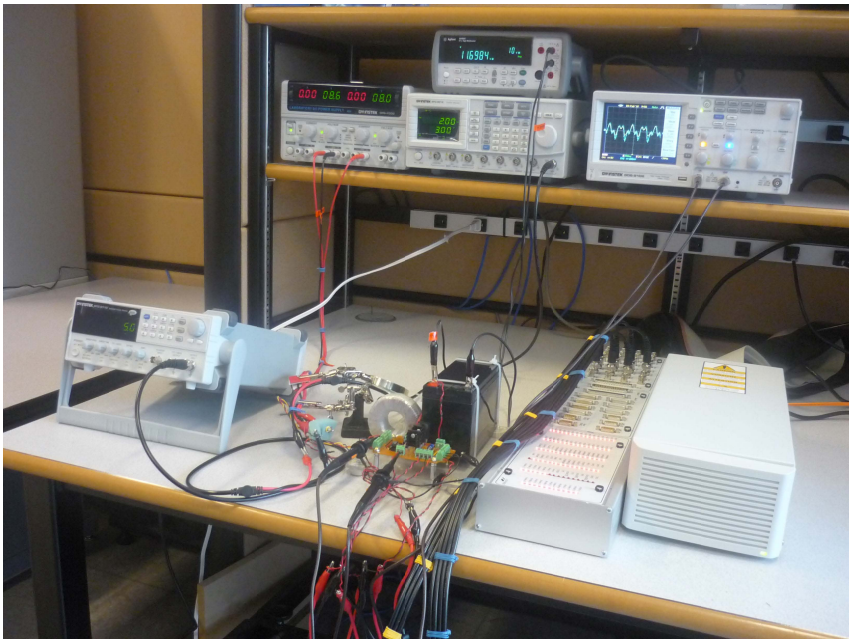

Figure 2.13: Experimental setup.

no phase difference.

It also must be noted that the negative cycle oscillations of the input current in Figures 2.14-a and 2.15-a are caused by induced noise due to using a floating ground AC input source. Since the floating point and the circuit ground cannot be completely isolated, some induced noise in the input current has appeared in negative cycles.

The inductive behavior of the circuit was also investigated using the experimental setup. The significant phase difference between input voltage and input current shown in Figure 2.16 illustrates that a large value of duty cycle ($d = 99\%$) of PWM control signal results in inductive behavior of the circuit (i.e., when $d > 1 - \frac{v_i}{V_B + V_D}$ as per (2.14)).

The efficiency of the proposed converter was also investigated by calculating the electrical power at the input and output of the converter. Figure 2.17 illustrates the efficiency versus different values of the PWM duty cycle. As shown in this figure, the efficiency remains almost constant when the duty cycle is above 10% and decreases when the duty cycle is above the boundary value for resistive operation, i.e., 76% obtained from (2.14). The drop in efficiency at low duty cycles can be attributed to switching losses due to large current

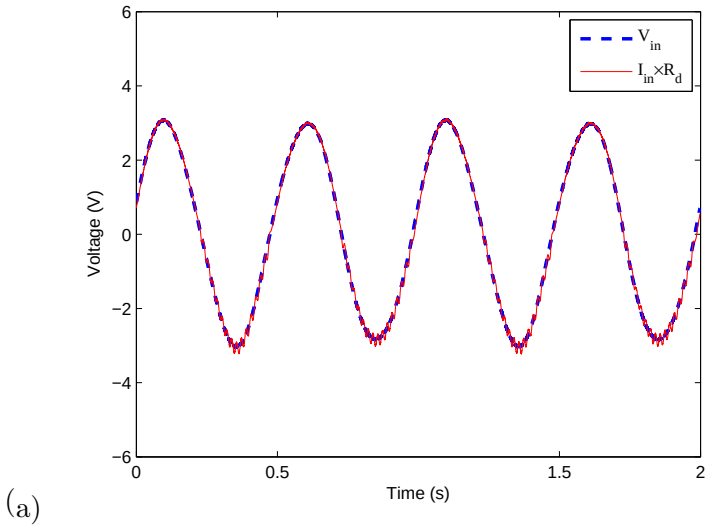


(a)

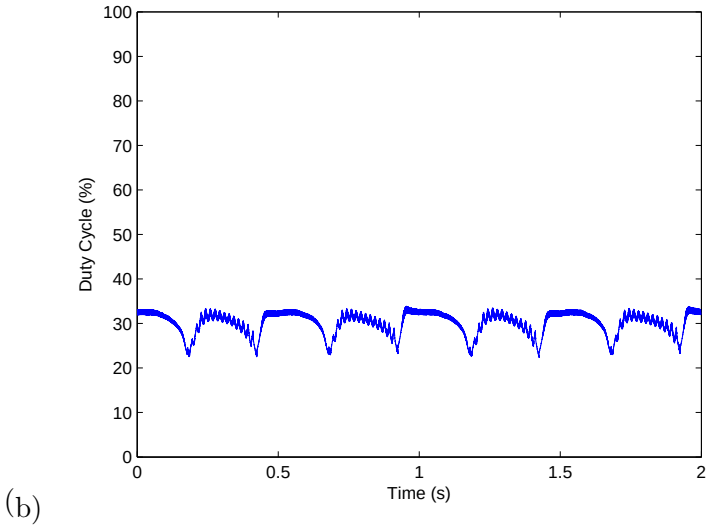


(b)

Figure 2.14: Experimental waveforms for a sine wave input source: (a) Input voltage and input current multiplied by the value of desired resistance ($R_d = 5k\Omega$), (b) Duty cycle of PWM signal.

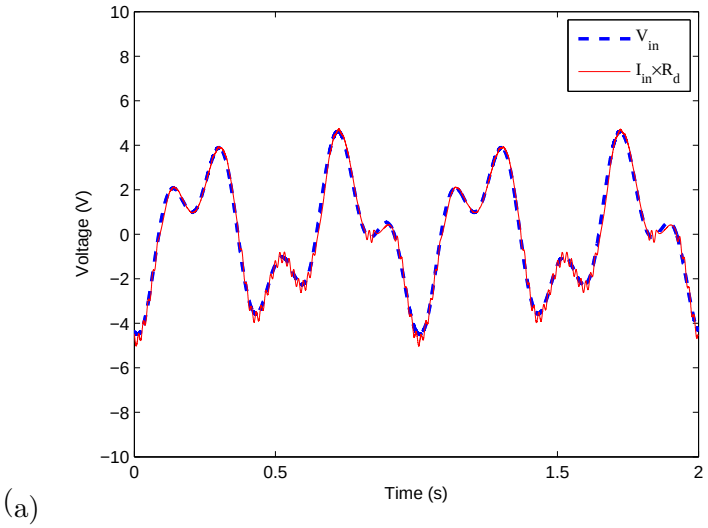


(a)

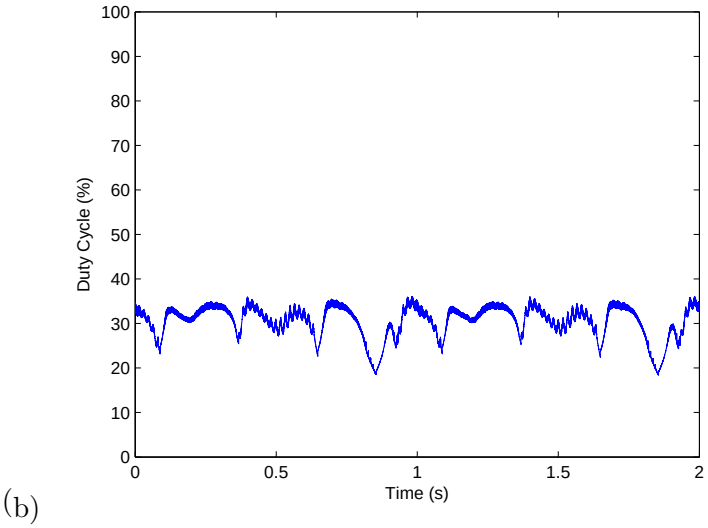


(b)

Figure 2.15: Experimental waveforms for a multi-frequency input signal: (a) Input voltage and input current multiplied by the value of desired resistance ($R_d = 5k\Omega$), (b) Duty cycle of PWM signal.

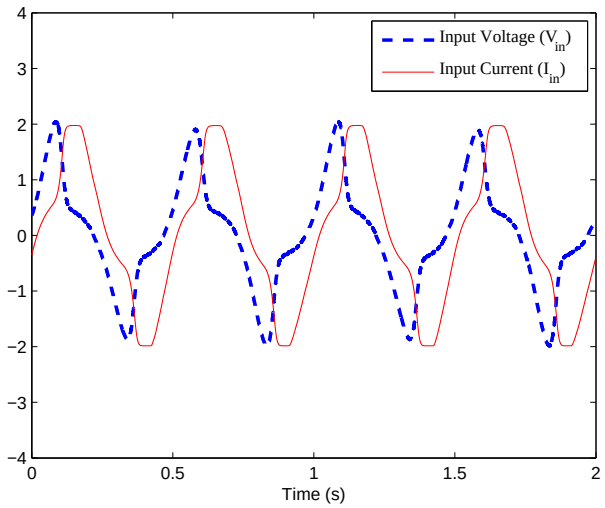


Figure 2.16: Experimental results showing inductive behavior of the circuit.

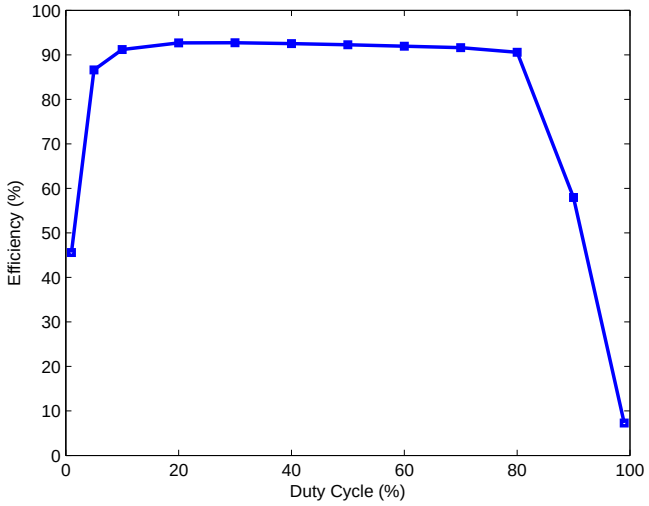


Figure 2.17: Converter efficiency for different values of duty cycle.

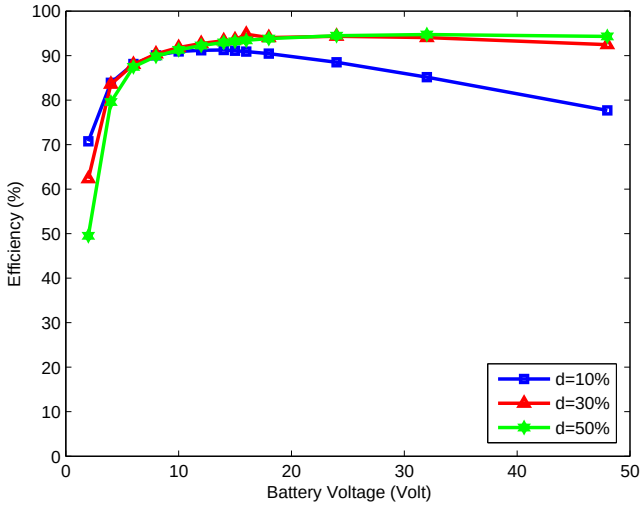


Figure 2.18: Converter efficiency for different values of battery voltage.

spikes in the discontinuous conduction mode. Operating the circuit with a duty cycle above 76% will decrease the efficiency since the circuit does not operate in the resistive region and power conversion efficiency drops due to the inductive behavior of the circuit. It must be noted that the aforementioned efficiencies were obtained by considering all possible losses of the circuit such as switching, diodes and inductor losses. The efficiency can be increased further by using lower power/voltage MOSFETs.

Figure 2.18 indicates that increasing the battery voltage improves the efficiency for higher values of duty cycle. In fact, increasing battery voltage $V_B$ extends the specific bound for $d$ obtained from (2.14) by making it closer to one. This effect enables the circuit to operate in resistive region for higher value of PWM duty cycle. Therefore, the switching power losses are reduced which results in higher efficiency. However, the efficiency changes significantly for other values of the duty cycle as observed from Figure 2.18. For instance, if $V_B = 48V$, the efficiency decreases from 95% to 79% when the duty cycle changes from 50% to 10%. It must be noted that although higher $V_B$ results in higher efficiency for higher duty cycles, it will also cause of decreasing efficiency for lower duty cycles. In summary, for an application with huge range of changing load resistance (changing of duty cycle consequently), the mid size for battery ($12V$) is the best choice, as efficiency almost remains constant for different

duty cycles (91%). For application requiring high desired input resistance (low duty cycle), it is better to use smaller size of battery, while large size of battery is needed for application requiring lower desired resistance. In this application, a $12V$ battery is used with the efficiency remaining almost constant (91%) for a wide range of the duty cycle ratios.

## 2.5 Summary and Conclusions

In this chapter, analytical expressions describing the input characteristic of a single-phase boost-type rectifier were derived, based on which a feedback controller was designed to achieve a pseudo-resistive input behavior. It is shown that the circuit exhibits a nonlinear pseudo-resistive behavior as long as the duty cycle of the control signal remains below a specific bound. The analytic expressions for pseudo-resistive behavior were utilized to derive a feedback control scheme and corresponding component values and switching frequencies. Furthermore, performance of the converter with feedback control was demonstrated through simulation and experimental studies. The results indicate that by using feedback control one can successfully enforce a *linear* resistive behavior between the input current and voltage with arbitrary waveforms. The value of input resistance can be changed in real-time by changing the desired resistance applied to the controller. This feature is used in a regenerative vibration damper to provide various damping effects by setting the equivalent electrical resistance to the desired mechanical damping which is investigated experimentally in Chapter 3.

# Chapter 3

# A Regenerative Suspension System using a Tubular DC Permanent-Magnet Machine

This chapter presents the development of an energy regenerative damper consisting of a mass-spring system coupled with a permanent-magnet DC machine, power electronics converter, and a battery. The vibration energy induced in the mass-spring system is converted into battery charge through the DC machine and a pulse-width-modulated boost-type converter developed earlier in Chapter 2, which enforces a pseudo-resistive behavior between its input terminals through the feedback control. Introducing this pseudo-resistive behavior across the DC machine produces the same effect as a mechanical damper but with an energy-regenerative function. To this end, the model of the permanent-magnet DC machine is presented in Section 3.2. Based on this model, the desired damping force that must be produced by the DC machine to convert the mechanical vibration energy into electric charge is obtained in Section 3.3. Experimental results are then provided in Section 3.4 that demonstrate the performance of the regenerative damper using a small-scale suspension system testbed described in Section 3.3. Finally, summary and conclusions are presented in Section 3.5.

## 3.1 Introduction

The main function of a suspension system is to isolate the vehicle chassis from the road disturbance and provide ride comfort and passenger safety. In particular, the relative shock and vibrations between sprung mass of a vehicle body and unsprung mass of the wheels caused by road profile and acceleration/decelerations of the car, must be damped to provide comfort and good road handling. Traditionally, the energy of this mechanical vibration is transformed into heat by passive shock absorbers due to friction. If this power loss can be recycled, the energy consumption will be reduced. Motivated by this, the idea of regenerative suspension systems with the primary goal of resolving the inherent tradeoffs between ride quality, handling performance, suspension travel and power consumption, was initiated.

Regenerative damping which constitutes converting the mechanical vibration energy into electric charge is of great interest due to an increasing demand for energy-efficient devices. Applications involving regenerative vibration damping at higher power levels ($200W$–$1kW$), for example in automotive systems, are attractive due to their potential to improve fuel-efficiency. Wendel *et al.* [112], proposed different configurations of regenerative systems in automobile suspensions. In [113], the concept of regenerative damping was introduced and a variable linear transmission was proposed. Suda *et al.* [114] proposed a hybrid control system with active control and energy regeneration to achieve vibration reduction with low energy consumption. A regenerative vibration control system with a pneumatic actuator was presented in [115].

The idea of using the electromagnetic linear actuators in automobile suspensions was proposed by many authors to get rid off the disadvantages of existing hydraulic active suspension systems such as slow response, high energy consumption, and complexity. In [116], an energy regenerative type vibration damper and suspension system were introduced using an electro-dynamic actuator. The feasibility of a self-powered active suspension control of a truck cab through an analytical energy balance method and numerical simulations was discussed in [117]. In this system, the electric machine mounted in the front suspension absorbs the vibration energy from the road excitation and stores it into a capacitor for vibration isolation of the cab suspension. This study indicates that sufficient energy is regenerated to supply power for active suspension control. Zhang *et al.* [118] utilized a combination

of a ball screw and permanent-magnet brushless DC motor in their regenerative suspension system to investigate feasibility of the concept. In [119], an energy recuperation and management scheme was presented for automotive suspension systems with linear electric motor using $H_\infty$ controller. A hydraulic transmission electromagnetic energy-regenerative suspension system was proposed by Lin *et al.* in [120]. Their suspension system combines mechanical, electromagnetic, and hydraulic structures all together to recycle the vehicle shock energy. Developments in power electronics and permanent magnet materials justify the possibility of implementing electromagnetic machines to improve performance of automobile suspension systems. Martins *et al.* [121] developed a permanent-magnet linear actuator for automobile active suspension. An energy converter consisting of a DC motor with a step-up chopper was proposed in [122], in which the energy is regenerated from a low-speed and low-voltage generator into a high voltage circuit. However, issues regarding the efficiency and performance of the power electronics converter were not studied.

The above works on regenerative suspension have investigated different topics such as the feasibility and development of electromagnetic machines and mechanisms for energy conversion. However, they have not addressed power control for maximum energy capture from vibration waveforms with time-varying amplitudes and frequencies. Such waveforms are typically present in a vehicular suspension system and depend on the road profile and vehicle's dynamic characteristics. To address the above issue in power control, we utilize the circuit discussed earlier in Chapter 2, to enforce a resistive behavior at its input terminals through feedback control. Using the proposed control strategy, the battery would look like a pure resistor as seen from the inputs of the power electronics circuit; thus realizing a controllable damper system. Furthermore, the damping coefficient of the system can be set and changed in real-time.

## 3.2 Modeling of a Tubular DC Permanent-Magnet Machine Used in the Suspension Testbed

Direct drive linear machines have been utilized in low frequency applications, where mechanical gearing is undesirable, or when low inertia is required [123]-[124]. Since mechanical vibrations of a suspension system are in the form of linear reciprocating motion, an electromagnetic linear machine shown in Figure 3.1 is utilized in this work. The machine

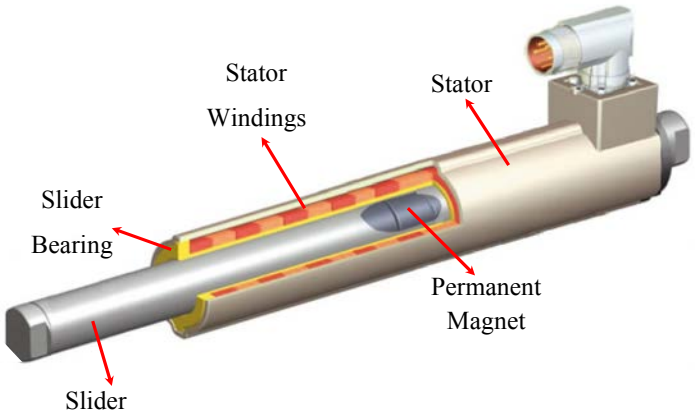


Figure 3.1: Linear permanent-magnet tubular machine [125].

is essentially an actuator, but in this work it has been used as a generator to convert mechanical vibrations into electricity. The direct-drive machine has low friction and cogging forces and consists of two parts including a slider and a stator. The slider is made of high strength neodymium magnets encased in a high-precision stainless steel tube. The stator contains the windings, slider bearings, and a position encoder. The machine operates based on the voltage generated due to the relative motion between a stack of permanent magnet rings separated by soft iron rings. Referring to Figure 3.1, the slider is free to move through the stator coil windings. In the following, a model of the above machine is presented that describes a relationship between the vibration dynamics and generated voltage. Following [124], the voltages of stator windings, i.e., phases 1 and 2, can be obtained from

$$v_j = -r_j i_j + \frac{d\lambda_j}{dt}, \quad \lambda_j = \sum_{k=1}^{2} L_{jk} i_k + \lambda_{jf} \tag{3.1}$$

where $j = 1,\ 2$, and $r_j$ is the resistance of phase $j$; $i_j$ is the current of phase $j$; $\lambda_{jf}$ represents the flux linkage in phase $j$ due to the magnets; and $L_{jk}$, $j,\ k = 1,\ 2$ are the self ($j = k$) and mutual ($j \neq k$) inductances. These inductances are generally position dependent.

Furthermore, the flux linkage due to the permanent magnet depends on the pole pitch and displacement $z$. The maximum flux linkage occurs when the coil axis is aligned with that of the soft iron pole. The generated voltage of each phase is thus given by

$$E_j = \frac{d\lambda_{jf}}{dt} = \frac{d\lambda_{jf}}{dz}\frac{dz}{dt} \tag{3.2}$$

For phase 1 used in this study, we have

$$\lambda_{1f} = N\phi_1 = N\hat{\phi}\cos(\frac{\pi}{\tau}z) \tag{3.3}$$

where $z$ is the relative displacement, $\lambda_{1f}$ is the flux linkage (for phase 2, $\lambda$ is shifted by 90 degrees), $\tau$ represents the pole pitch of the generator, $N$ is the number of turns in each phase, and $\hat{\phi}$ represents the peak flux in the air-gap. Substituting (3.3) into (3.2) results in

$$E_1 = \frac{d\lambda_{1f}}{dt} = -N\hat{\phi}\frac{\pi}{\tau}\sin(\frac{\pi}{\tau}z)\frac{dz}{dt} \tag{3.4}$$

where $E_1$ is the generated voltage of phase 1. Equation (3.4) can be further written as

$$E_1 = -\beta(z)\dot{z} \tag{3.5}$$

where

$$\beta(z) = N\hat{\phi}\frac{\pi}{\tau}\sin(\frac{\pi}{\tau}z). \tag{3.6}$$

Equation (3.5) indicates that the generated voltage will not be a pure sinusoidal waveform in response to the up-down translational motion as a result of the nonlinear term $\beta(z)$. This equation will be used in Section 3.3 to find a relationship for the optimal force that the DC machine must produce to harvest *active* power from mechanical vibrations.

## 3.3 Suspension System Dynamics and Desired Loading of the DC Machine

Figure 3.2 shows the schematic diagram of the regenerative damping system, where $m_b$, $m_w$, $K_s$, $K_w$, and $C_s$ represent a quarter of the sprung mass of a vehicle body, the unsprung mass of one wheel, the stiffness of the spring, the tire stiffness, and the damping coefficient, respectively. The desired damping is specified by the lower right block shown in Figure 3.2. The desired damping specified by this block is transformed into an equivalent electrical

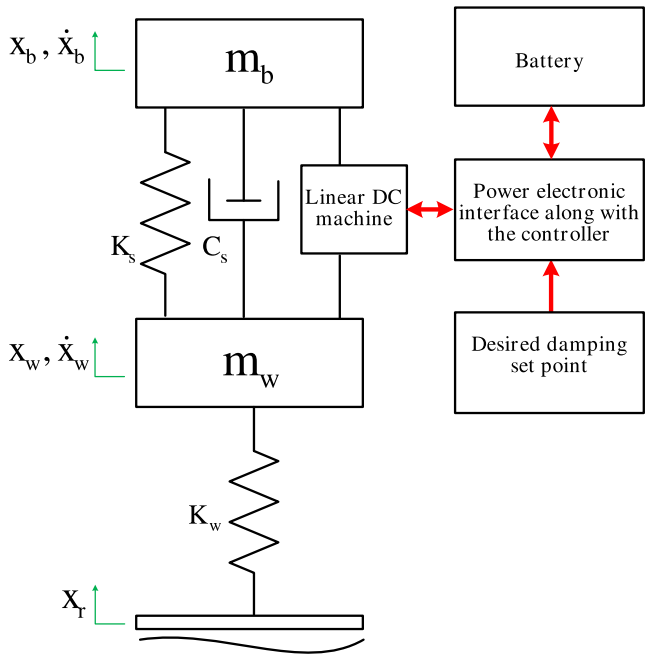


Figure 3.2: Schematic diagram of the regenerative vibration damping system.

input resistance and provided as a set-point to the feedback control scheme. The desired resistance is implemented by using a power electronics circuit converter and feedback control as discussed in Sections 2.2 and 2.3.

Using a free-body diagram, and neglecting friction, the equations of motion for this system are given by

$$m_b\ddot{x_b} = -C_s(\dot{x_b} - \dot{x_w}) - K_s(x_b - x_w) + F_g \tag{3.7}$$

$$m_w\ddot{x_w} = C_s(\dot{x_b} - \dot{x_w}) + K_s(x_b - x_w) - K_w(x_w - x_r) - F_g \tag{3.8}$$

where $x_w$, $x_r$, and $x_b$ represent vehicle's wheel displacement, road displacement, and vehicle's body displacement, respectively, and $F_g$ is the upward reaction force of the linear DC generator.

Assuming that the unsprung mass $m_w$ is negligible compared to $m_b$, and the tire stiffness $K_w$ is relatively large, an approximate one-degree-of freedom (1-DOF) system can be obtained as shown in Figure 3.3. Using a free body diagram and neglecting friction, the

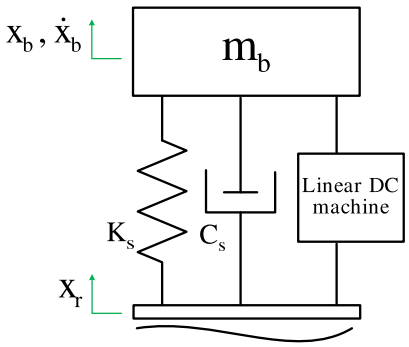


Figure 3.3: One-degree-of freedom model of the suspension system.

equations of motion for this system are thus given by

$$m_b\ddot{x_b} = -C_s(\dot{x_b} - \dot{x_r}) - K_s(x_b - x_r) + F_g \tag{3.9}$$

where $F_g$ is the upward reaction force of the DC generator.

Now, let us define

$$z = x_b - x_r \tag{3.10}$$

where $z$ is the relative displacement. Therefore, (3.9) can be written as

$$m_b\ddot{z} + C_s\dot{z} + K_s z = F_r + F_g \tag{3.11}$$

where

$$F_r = -m_b\ddot{x_r}. \tag{3.12}$$

Now, let us find the optimum value of the force that the DC machine must produce to harvest maximum power from mechanical vibrations. To this end, the total energy of the system can be written as the summation of potential and kinetic energies as follows

$$E = \frac{1}{2}m_b{\dot{x_b}}^2 + \frac{1}{2}K_s z^2 \tag{3.13}$$

Therefore, the available power in the mass-spring system is given by

$$P = \frac{dE}{dt} = m_b\ddot{x_b}\dot{x_b} + K_s z\dot{z}. \tag{3.14}$$

Substituting $m_b\ddot{x}_b$ from (3.9) into (5.14) and performing some algebraic manipulations result in

$$P = (F_g - C_s\dot{z} - C_s\dot{x_r})\dot{z} + (F_g - K_s z)\dot{x_r} \tag{3.15}$$

Now let us obtain the maximum available mechanical power in the system which should ideally be converted into electric power. To this end, differentiating $P$ as follows

$$\frac{\partial P}{\partial \dot{z}} = 0 \tag{3.16}$$

and solving for the speed results in

$$\dot{z}_{opt} = \frac{F_c + F_g}{2C_s} \tag{3.17}$$

where

$$F_c = -C_s\dot{x_r} \tag{3.18}$$

Thus $\dot{z}_{opt}$ is the speed corresponding to the maximum power in the suspension system in the form of kinetic and potential energies. Now, let us consider the equations of the DC machine given by

$$P_g = F_g\dot{z} \tag{3.19}$$

$$F_g = \alpha i \tag{3.20}$$

where $P_g$ is the power generated by the machine, $i$ is the current passing through the stator coil generating the force $F_g$, and $\alpha$ is the motor constant. Substituting the value of relative velocity from (3.17) into (3.19) and (3.5), respectively, results in

$$P_g = F_g\frac{F_c + F_g}{2C_s} \tag{3.21}$$

$$E_{1,opt} = -\beta(z)\frac{F_c + F_g}{2C_s} \tag{3.22}$$

Equation (3.21) specifies the power that can be captured by the DC machine and (3.22) indicates the amount of generated electrical voltage under this condition. Thus the maximum power that can be transferred from this generated power to a load is obtained by differentiation as follows

$$\frac{\partial P_g}{\partial F_c} = 0 \tag{3.23}$$

which results in

$$F_{g,opt} = -\frac{1}{2}F_c. \tag{3.24}$$

Substituting (3.24) and (3.20) into (3.22), will result in the desired relationship between the current and voltage of the machine for maximum power transfer as follows

$$E_{1,opt} = Ri_{opt} \tag{3.25}$$

where

$$R = \frac{\alpha\beta(z)}{2C_s}. \tag{3.26}$$

The above result indicates that to transfer the maximum mechanical power into electric power, there must be a resistive relationship between the generated voltage and current across the electric terminals of the machine. In other words, the load should be purely resistive. This result could have been expected due to the equivalence between mechanical damping and electric resistance. However, (3.26) provides a quantitative relationship to determine the desired electrical resistance and consequently the extracted power based on the DC machine parameters $\alpha$, $\beta(z)$, and the damping coefficient $C_s$ of the suspension system. Another consideration in determining the desired damping is the ride comfort and stability that can be achieved by using control schemes such as sky-hook [126]-[127]. In practice, the desired value of electrical resistance should be determined by a compromise between ride comfort and energy extraction characteristics.

## 3.4 Experimental Setup and Results

To evaluate performance of the proposed regenerative vibration damping system experimentally, implemented power electronic circuitry, which was discussed earlier in Chapter 2, was connected to the mass-spring test rig attached to a mechanical shaker, as depicted in Figure 3.4. The mass-spring experimental setup consists of four parallel springs and a DC machine (LinMot P01-37 $\times$ 120) with motor constant $\alpha = 25.8N/A$ which isolates the mass from base excitations. The sprung mass was $5.4kg$; the stiffness of each spring was $2.3kN/m$, resulting in a total stiffness of $K_s = 9.2kN/m$; and the damping coefficient of the system was measured as $C_s = 445.8Ns/m$ using a time domain excitation and observing the decay.

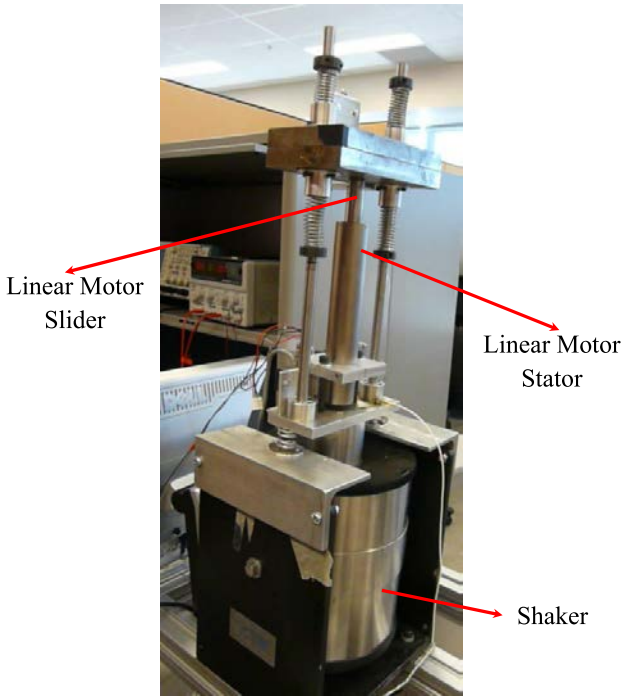


Figure 3.4: Mass-spring test rig connected to a mechanical shaker and permanent-magnet machine.

The slider of the linear motor is a bar magnet connected to the mechanical shaker and isolated from the stator winding of the DC machine through the mass-spring system. The shaker can be excited with motion profiles containing different frequencies in the range $5 - 20Hz$. In the experiments, the shaker was set to oscillate at $6Hz$ with an acceleration amplitude of $0.12g$, where $g = 9.8m/s^2$ is the acceleration of gravity. The internal inductance of the motor, $L_m = 3.1mH$, was utilized as the boost converter inductor $L$ shown in Figure 2.2. Phase 1 of the generator shown in Figure 3.1 was connected to the input of the power electronics interface. The voltage of this phase along with the current passing through the inductor, were measured using two LT1167 instrumentation amplifiers. These two signals along with the battery voltage were then captured by ADC channels of the dSPACE. The circuit input resistance between input terminals $XY$ in Figure 2.2 was then calculated at each sampling time by dividing the input voltage by the averaged inductor current in one PWM period ($0.001s$). The PWM frequency of 1 $kHz$ was selected to be much higher than

the frequency content of the input waveform and meet the closed-loop control bandwidth requirements. On the other hand, this frequency should not be very large to avoid power losses due to switching and electromagnetic interference. In practice, the PWM period should be selected to achieve a balance between the above factors. The value of $d$ was obtained from (2.23), (2.29), and (2.32), and applied to the converter at each sampling instant.

Figure 3.5 illustrates the experimental results with no damping, and Figure 3.6 shows the results with the damping in which maximum power is transferred from DC machine to the power converter. Note that the maximum power transfer takes place at a damping equivalent to $R_d = 6\Omega$, which is equal to the internal resistance of the DC machine as depicted in Figure 3.7. Using the nominal values of the parameters given in this section, (3.26) yields a resistance of $0.8\Omega$ which is not feasible to implement using converter due to the $6\Omega$ resistance of the coil winding. This damping limit can be also observed at higher desired resistance (lower mechanical damping) from Figure 3.8 which illustrates the relationship between the desired electrical resistance and the relative displacement of the stator and slider measured by a distance measurement sensor attached to the shaker setup. The distance measurement sensor is a string potentiometer that was used to measure the relative displacement. It can be observed that for larger resistances (lower damping), the relative displacement does not change much due to the dominance of other damping effects such as friction; hence the damper is less effective in that region. Thus for the machine used in this study, maximum power transfer is limited by the electric resistance of the winding as opposed to the damping of the suspension system. Thus a potential use of (3.26) is to select or design the machine based on the damping characteristics of the suspension system. It must be also pointed out that increasing the damping reduces the relative displacement as shown in Figures 3.5-b and 3.6-b. Consequently, the absolute acceleration of unsprung mass of the vehicle body is reduced which is desired for ride comfort. However, decreasing the relative displacement results in less power generated by the DC machine as a regenerative damper. Therefore, there is always a compromise between ride comfort, car handling, and energy extraction characteristics.

Figures 3.9-a and 3.10-a illustrate performance of the controller for desired input resistances $2.75K\Omega$ and $100\Omega$, respectively. Since there is no phase difference between voltage and current shown in these figures, power transfer is accomplished with unity power-factor

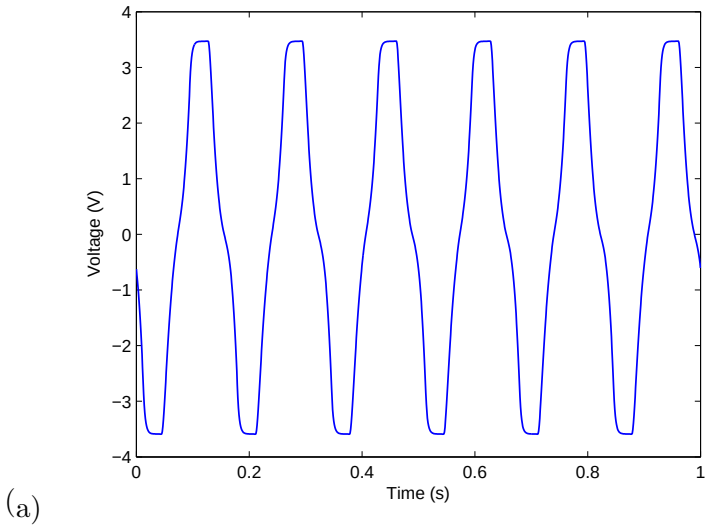


(a)

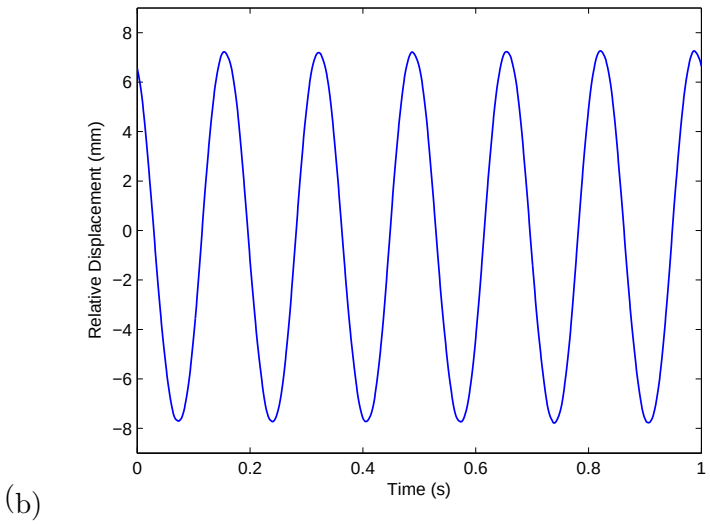


(b)

Figure 3.5: Experimental results with no damping: (a) Voltage generated by the DC machine, (b) Relative displacement.

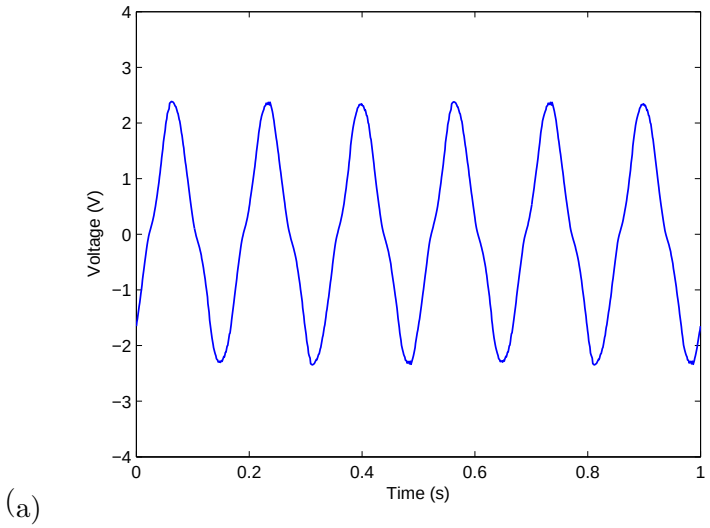


(a)

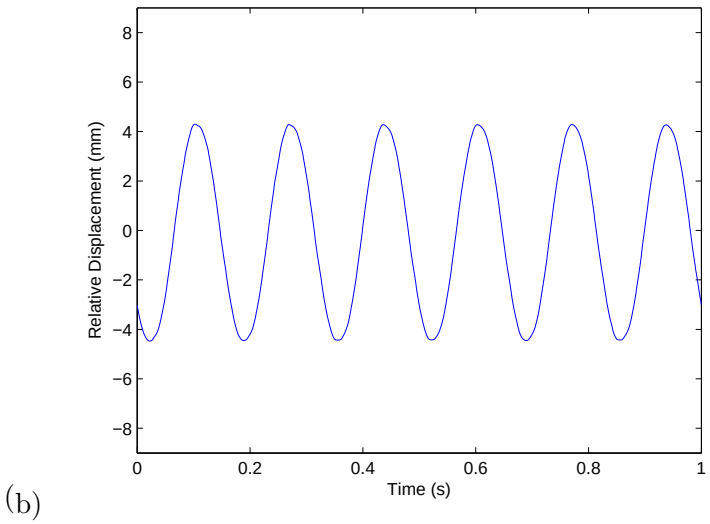


(b)

Figure 3.6: Experimental results with the damping in which maximum power is transferred to the power converter ($R_d = 6\Omega$): (a) Voltage generated by the DC machine, (b) Relative displacement.

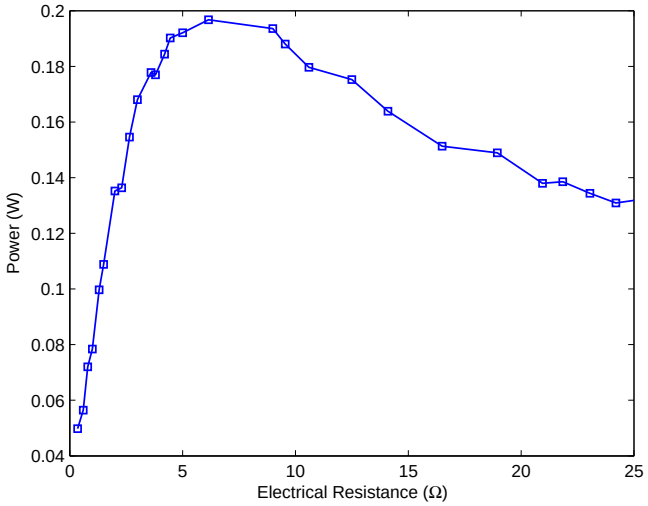


Figure 3.7: Transferred power from DC machine to the battery versus the desired input resistance of the converter.

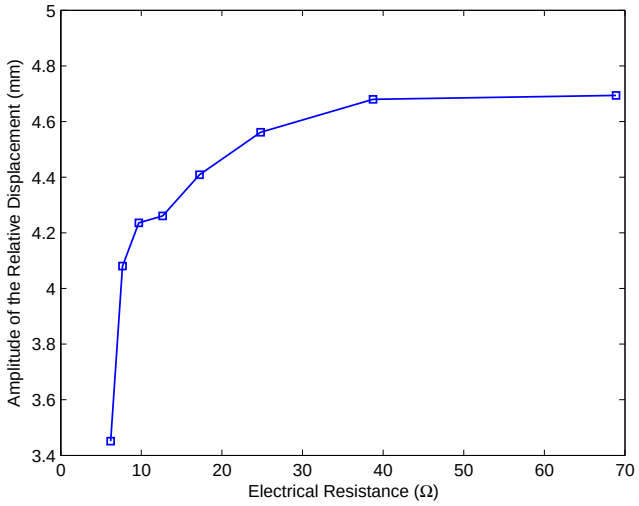


Figure 3.8: Amplitude of the relative displacement versus the desired input resistance of the converter.

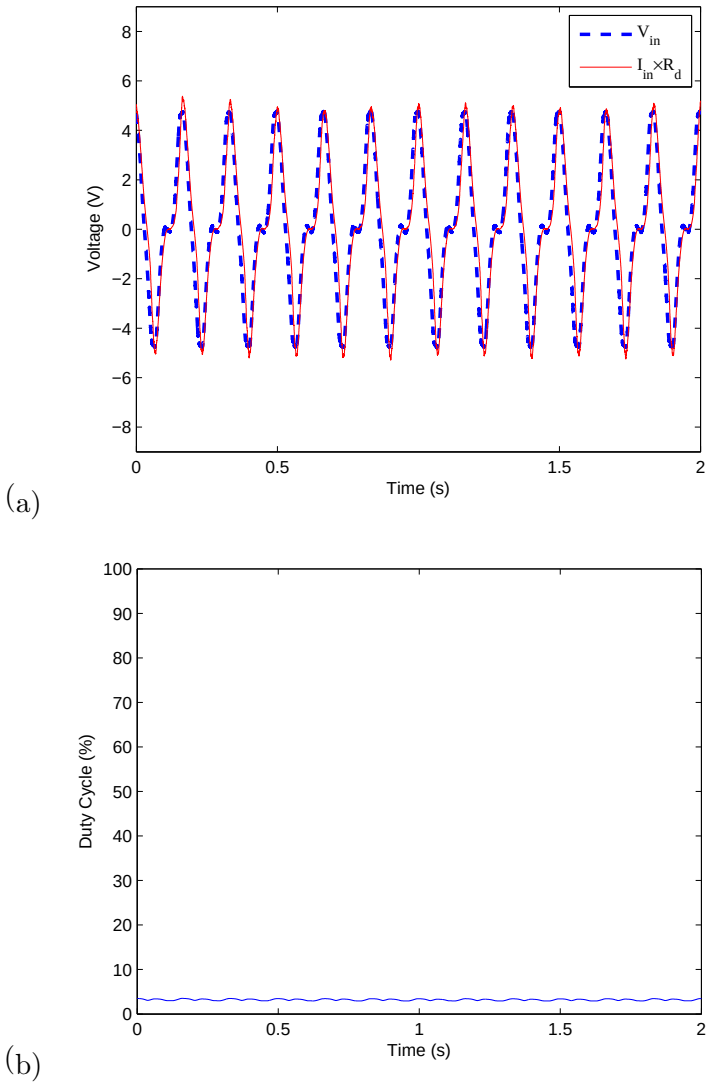


Figure 3.9: Experimental waveforms for vibration energy converter: (a) Voltage generated by the DC machine and averaged converter input current multiplied by the value of desired resistance ($R_d = 2.75k\Omega$), (b) Duty cycle of the PWM control signal.

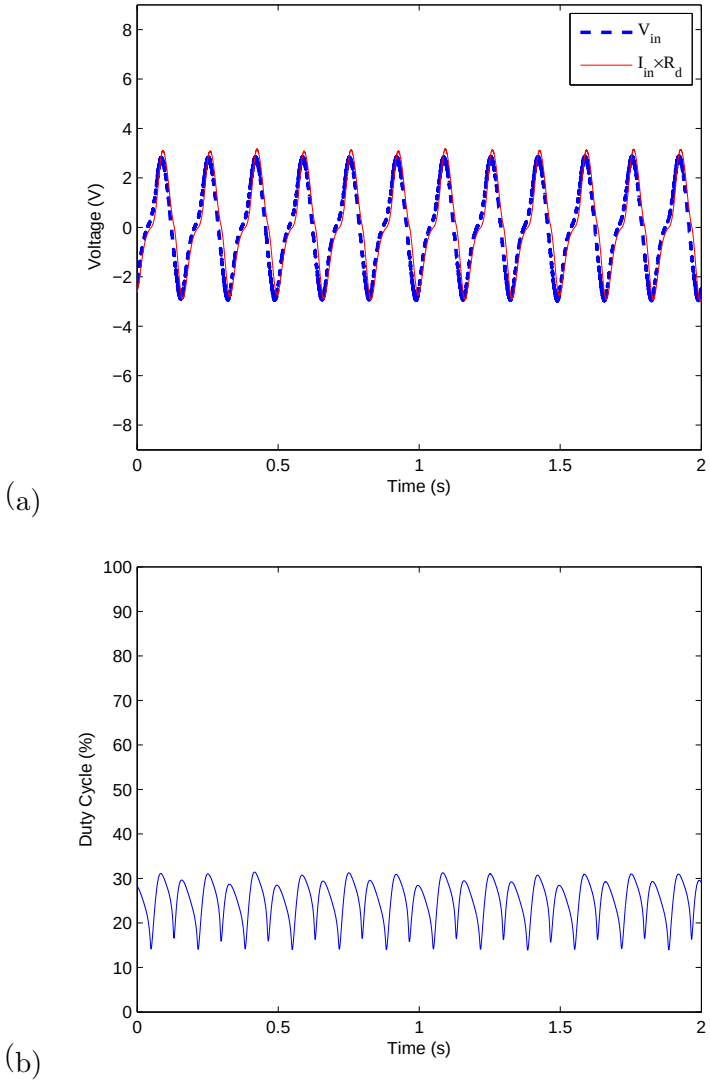


Figure 3.10: Experimental waveforms for vibration energy converter: (a) Voltage generated by the DC machine and averaged converter input current multiplied by the value of desired resistance ($R_d = 100\Omega$), (b) Duty cycle of the PWM control signal.

for arbitrary vibration amplitudes and frequencies. It should be pointed out that the voltage $v_{in}$ is the input voltage after deducting the drop across the $6\Omega$ resistance of the linear DC machine. Comparing Figures 3.9-a and 3.10-a reveals that when the desired resistance decreases from $2.75K\Omega$ to $100\Omega$, more current is drawn from the stator coil, which decreases the vibration amplitude, i.e., more power is transferred to the battery in the form of electrical charge. Since the relative displacement of the stator and slider decreases, the amount of induced voltage also decreases. Also, the induced noise in the input current in negative cycles has been removed since the input of the converter is connected to the DC machine which is isolated from the circuit ground.

Figures 3.9-b and 3.10-b indicate variations in the duty cycle of the PWM signal which are obtained from the feedback controller. These variations are necessary to compensate the nonlinear and uncertain terms in (2.10) to achieve the desired resistances $2.75K\Omega$ and $100\Omega$, respectively. It should be noted that decreasing the desired input resistance corresponds to a larger duty cycle and larger variations in the duty cycle. This effect can be verified by obtaining the sensitivity of input resistance $R_k$ in terms of the duty cycle $d$. Ignoring the nonlinear term in (2.10) and substituting $t_{on} = dT_s$, results in

$$R_k \approx \frac{2L}{T_s} d^{-2} \tag{3.27}$$

from which the variation of duty cycle, $\Delta d$, is obtained by using differential analysis as follows

$$\Delta d \approx -\frac{1}{2} d \frac{\Delta R_k}{R_k}. \tag{3.28}$$

The above equation indicates that as the feedback controller tries to enforce a small relative error $\Delta R_k/R_k$, higher values of the duty cycle (corresponding to smaller resistances) will result in larger variations of the duty cycle as corroborated by experimental results in Figures 3.9-b and 3.10-b.

Finally, to validate the performance of the regenerative vibration damping system for different frequencies, the shaker setup was excited with a sinusoidal signal that was linearly swept between 5Hz to 20Hz at a rate of 0.1 Hz/s. A displacement of 3.05mm peak-to-peak was set for the shaker, which corresponds to the maximum excitation the system could handle at resonance without bottoming out determined experimentally. The results were obtained for higher values of damping coefficients corresponding to lower values of desired input resistances, i.e., $7\Omega$, $9\Omega$, $12\Omega$, $17\Omega$, and $20\Omega$ with 10% resolution. The system

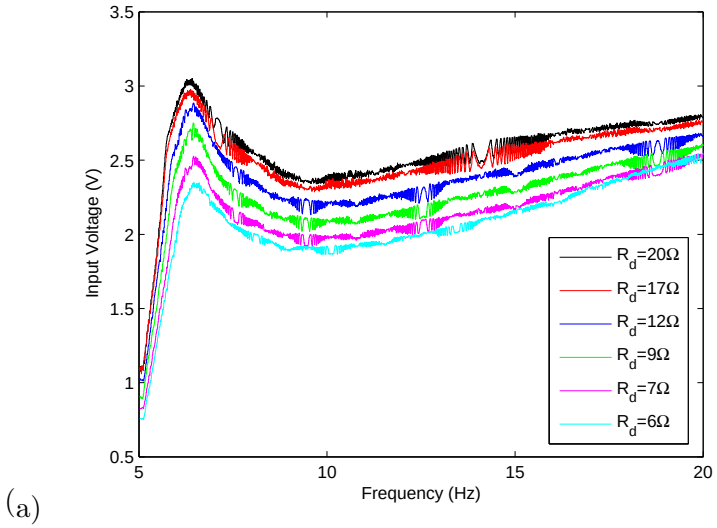


(a)

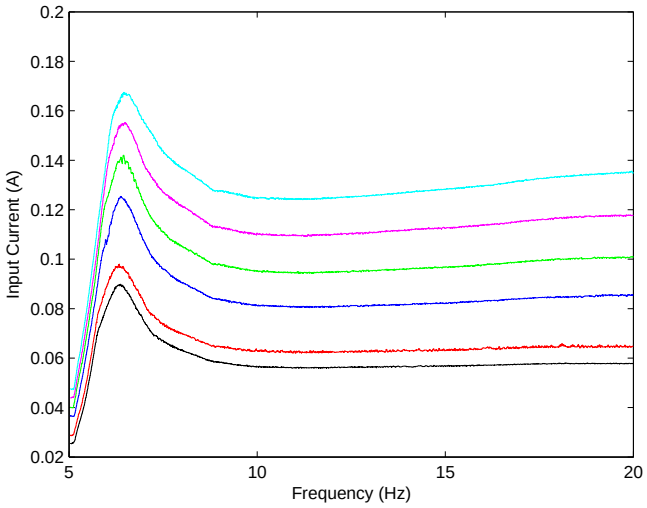


(b)

Figure 3.11: Experimental waveforms for vibration energy converter: (a) Voltage generated by the DC machine for different values of desired input resistances, (b) Input current of the boost converter drawn from the DC machine.

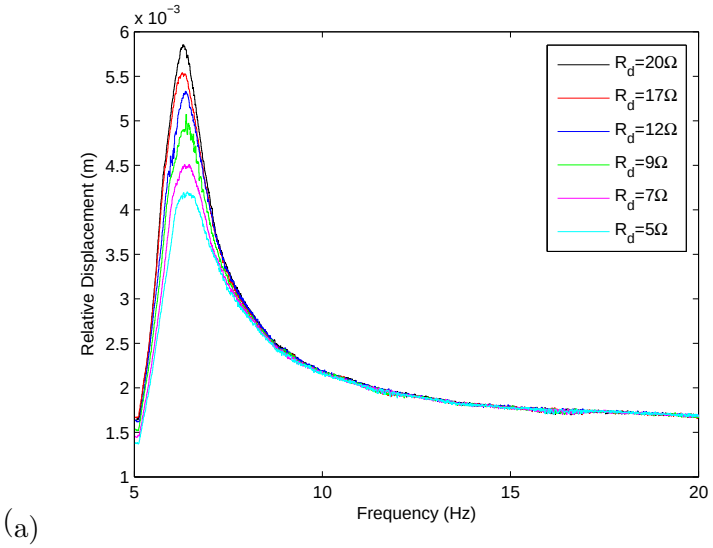


(a)

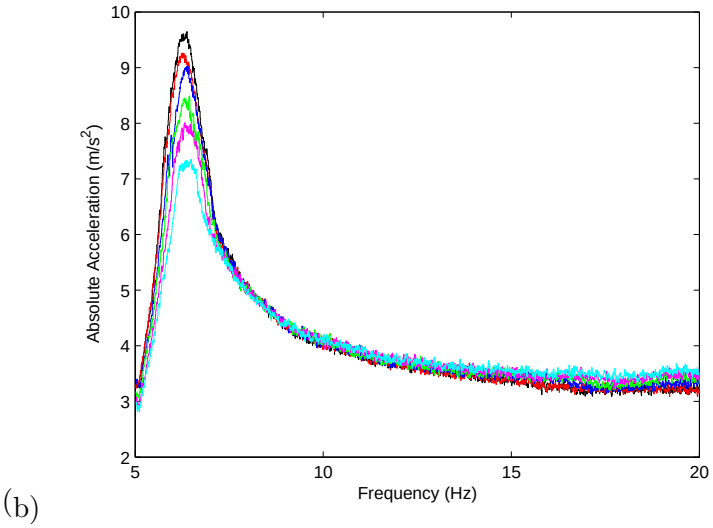


(b)

Figure 3.12: Experimental waveforms for vibration energy converter: (a) Relative displacement, (b) Absolute acceleration.

can achieve the desired values of input current with a decrease in the input resistance as shown in Figure 3.11-b. Also, the input current increases at higher frequencies when the resistance is low (heavy damping). When the resistance is high (low damping), the response remains relatively flat. Moreover, the input voltage shown in 3.11-a indicates a relative decrease in the amplitude of vibrations with an increase in the input current. In fact, the induced voltage of linear DC motor depends on both relative displacement and velocity as indicated by (3.4). By setting the input resistance to a lower value (higher damping), more current would be drawn from the motor coil, resulting in a higher damping effect. This damping effect decreases the relative displacement, which reduces the amplitude of generated voltage at low frequencies. For higher frequencies, the generated voltage is increased due to higher velocities. At higher frequencies, the low input resistance (heavy damping) shows a sharper increase in voltage when compared with their lightly damped companions, which was expected for the generated voltage at the output terminals of a linear DC motor and the relative displacement and velocity as indicated in (3.4). The relative displacement, which may represent the car handling in a real situation, and the absolute acceleration, which can be a measure of the passenger ride comfort, are shown in Figure 3.12. The results indicate that the system does not experience a natural frequency shift (the spring constant remained constant) since the boost converter only changes the damping coefficient. The heavier damped system shows lower displacement and acceleration around resonance frequency, while its acceleration at higher frequencies is slightly higher than the lightly damped system. The relatively high displacement at resonance and low acceleration values are due to the fact that the system has a fairly low spring constant.

## 3.5 Summary and Conclusions

In this chapter, the boost-type converter along with the feedback control strategy which were discussed earlier in Chapter 2, was implemented on an energy-regenerative suspension system testbed. It was shown that to transfer the maximum power to the load, there must be a resistive relationship between the input voltage and current of the power electronics interface. The boost converter circuit along with the feedback control strategy were utilized to enforce a pseudo-resistive behavior between the DC machine output terminals. Furthermore, performance of the suspension system testbed was evaluated through experimental

studies. The results indicate that the boost circuit and proposed feedback controller can successfully provide regenerative damping for mechanical vibrations with high-efficiency power conversion for the boost converter.

# Chapter 4

# Modeling and Control of a Three-Phase Boost Converter

In this chapter, the idea presented in Chapter 2 is extended to a new modeling and control technique for a three-phase boost converter to efficiently transfer energy from an irregular input power source to a battery storage device or a DC link. First, a novel circuit model of a three-phase boost converter is developed using the method of averaging in Section 4.2. This model is then used for derivation of the conditions under which the pulse width modulated (PWM) switching circuit exhibits a resistive behavior from the input. Based on the circuit model obtained, a new model-based feedback control scheme is presented in Section 4.3 to regulate the three-phase input resistances of the circuit to desired values. The circuit can provide purely active power conversion of a band-limited input voltage source to a DC load, which is of interest in boost power converters for certain renewable energy conversion systems. Simulation studies and experimental results are presented Section 4.4 that illustrate performance of the proposed modeling and feedback control scheme for a low-power application using a dynamo system in the laboratory. Finally summary and conclusions are presented in Section 4.5.

## 4.1 Introduction

Three phase power electronic converters are required in renewable generation systems such as variable speed wind and marine wave energy. In these renewable energy systems,

the kinetic energy of the device is converted into stand-alone or grid-connected electricity through three phase synchronous or induction generators and power electronics interfaces. The intermittent characteristic of the above energy resources results in generated power profiles with time-varying voltages and currents whose amplitudes and frequencies are subject to random variations. Dynamically stable and efficient energy flow in these systems require the use of advanced power controllers that can adapt to the dynamic characteristics of the source and load. As noted in [128], traditional AC-DC converters using diodes and thyristors to provide energy flow have issues including poor power quality, voltage distortion, and poor power factor. The analysis of high power factor three-phase rectifiers and new control techniques are presented in [129]-[133]. Among the proposed topologies, three-phase boost/buck converters are good candidates to be utilized in energy conversion involving arbitrary band-limited sources of power as they can offer high efficiency and low EMI emissions. Performance criteria of these converters is highly dependent on the control strategy used. To improve the performance of pulse-width-modulated (PWM) boost/buck converters toward ideal power quality conditions, different control strategies have been presented using space vector modulation [134]-[135], soft switching [136], sliding mode [137], and other feedback control methods [138]-[143].

The above cited works have been mainly utilized in applications such as speed drives and power supplies for telecommunications equipment in which the mains supply is the input power source with a relatively fixed amplitude and frequency. These approaches have mainly assumed the circuits to be in the sinusoidal steady state, which cannot be applied to applications involving arbitrary band-limited sources of power with transient power profiles such as wind, wave, and mechanical vibrations. Furthermore, to achieve maximum power transfer in renewable energy converters including wind and wave, it is sometimes necessary to control the amount of generator loading, which can be achieved through appropriate control of the power electronics interface. For example, in variable speed wind energy conversion systems, there is an optimum torque-speed characteristic that would yield maximum power transfer to the electrical generator [144]-[145]. In [146], a condition for maximum extraction of the average power is obtained for a wave energy converter which suggests operation under the resonance condition with a resistive behavior seen by the generator.

An effective way of achieving the above conditions for maximum power transfer is to adjust the apparent electric load of the generator through an appropriate controller using a power electronics interface. To this end, the idea presented in this chapter is to enforce a

resistive behavior across each phase of a boost converter using feedback control. This idea is similar to the one presented in Chapter 2 but extended to a three-phase system. The proposed controller does not require a-priori knowledge of the input waveform characteristics and can convert band-limited waveforms with multiple input frequencies and amplitudes into DC power by regulating the input resistances at each phase of a three-phase power source to desired values.

## 4.2 Operating Principle and Circuit Analysis

The three-phase bridgeless boost converter considered in this chapter is shown in Figure 4.1. Compared to a full-bridge converter, the efficiency of these converters can be improved by 8%-10%, specially for low-power applications [147]. Furthermore, to reduce the switching losses, only one MOSFET is switching at each time instant while the other two are kept ON/OFF depending on the relative voltages of the corresponding phases.

In the following, we provide a brief review of the circuit operation followed by a derivation of the nonlinear resistances seen by the input sources $v_a$, $v_b$, and $v_c$ using the averaging method. Figure 4.2 illustrates snapshots for various modes of operation of the circuit in-

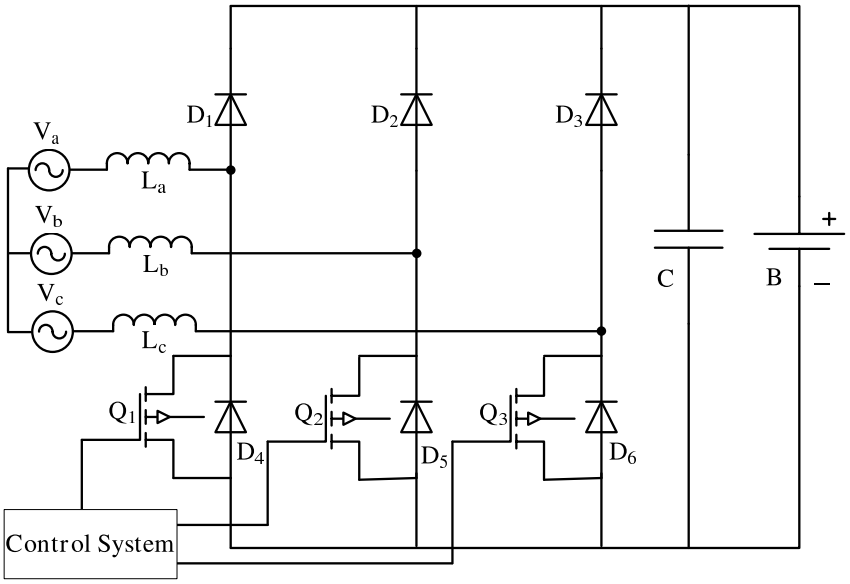


Figure 4.1: Three-phase bridgeless boost-type converter.

volving switches $Q_1$, $Q_2$, $Q_3$, and diodes $D_1$, $D_2$, $D_3$, with the corresponding phase to phase voltages, i.e., $V_{ij}(t)$ defined as follows

$$V_{ij}(t) = V_i(t) - V_j(t), \quad i, j = a, b, c, \quad i \neq j \tag{4.1}$$

For brevity, the argument $t$ in $V_{ij}(t)$ and $V_i(t)$ is dropped in the rest of this chapter. Without loss of generality, let us consider a typical case when $V_{ab} \geq 0$, $V_{ac} \geq 0$, for which $Q_1$ is switching in the ON/OFF mode while $Q_2$ and $Q_3$ are kept ON. As shown in Figure 4.2-a, when all switches are ON, none of the diodes $D_1$–$D_3$ can conduct. In this case, the inductor current of each phase builds up and the energy captured from the input sources is stored in the magnetic fields of the inductors. We denote this case as mode 1 of operation of the circuit.

Referring to Figure 4.2-b, when $Q_1$ is turned OFF, $Q_2$ is turned OFF and $Q_3$ is kept ON as long as $V_{bc} \geq 0$. Similarly, when $V_{bc} < 0$, $Q_3$ is turned OFF and $Q_2$ is kept ON. Next, let us consider mode 2 of operation of the circuit as follows. Assuming $V_{bc} \geq 0$, current flows through diode $D_1$, load, and back through the anti-parallel diode of $Q_2$ and switch $Q_3$, as depicted in Figure 4.2-b. In this case, the stored energy in the inductors together with the energy drawn from the input sources are fed to the battery. This condition is continued until $i_{Lb}$ reaches zero, after which mode 3 operation of the circuit starts as shown in Figure 4.2-c. In this mode, the remaining stored energy in $L_a$ and $L_c$ along with the energy coming from $v_a$ and $v_c$ charge the battery until the inductors are totally discharged. Table 4.1 summarizes the above modes of operation with all possible arrangements of phase-to-phase voltages. From this table, it is evident that the switches are all ON in mode 1 regardless of the phase-to-phase voltages. As soon as one of the switches is turned OFF, the states of other switches are changed according to the corresponding phase-to-phase voltages. Without

Table 4.1: The states of switches $Q_1$, $Q_2$, and $Q_3$ for different modes of operation.

| **Phase-to-phase voltages** | $Q_1$ | $Q_2$ | $Q_3$ | **Mode** |
|---|---|---|---|---|
| Any combination of voltages | ON | ON | ON | 1 |
| $V_{ac} \geq 0$, $V_{bc} \geq 0$ | OFF | OFF | ON | 2 |
| $V_{ab} \geq 0$, $V_{cb} \geq 0$ | OFF | ON | OFF | 2 |
| $V_{ba} \geq 0$, $V_{ca} \geq 0$ | ON | OFF | OFF | 2 |
| $V_{ac} \geq 0$, $V_{bc} \geq 0$, either $i_{L,a} = 0$ or $i_{L,b} = 0$ | OFF | OFF | ON | 3 |
| $V_{ab} \geq 0$, $V_{cb} \geq 0$, either $i_{L,a} = 0$ or $i_{L,c} = 0$ | OFF | ON | OFF | 3 |
| $V_{ba} \geq 0$, $V_{ca} \geq 0$, either $i_{L,b} = 0$ or $i_{L,c} = 0$ | ON | OFF | OFF | 3 |

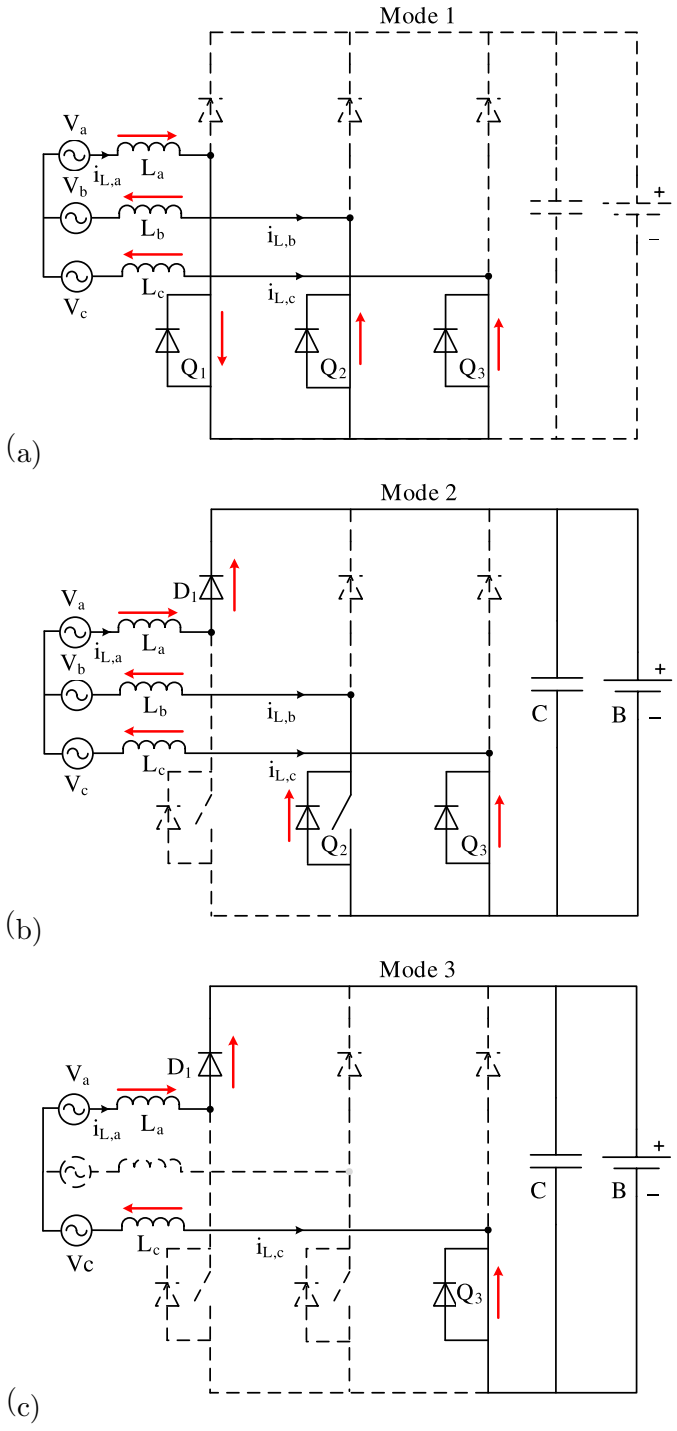


Figure 4.2: Operation modes of the three-phase boost rectifier when $V_{ac} \geq 0$, $V_{bc} \geq 0$ (first, second, and fifth rows in Table 4.1): (a) Mode 1 of circuit operation when $Q_1$, $Q_2$, and $Q_3$ are all ON, (b) Mode 2 of circuit operation when $Q_1$ and $Q_2$ are OFF and $Q_3$ is ON, (c) Mode 3 of circuit operation when $Q_1$ and $Q_2$ are OFF, $Q_3$ is ON, and the inductor current of phase $b$ reaches zero ($i_{Lb} = 0$).

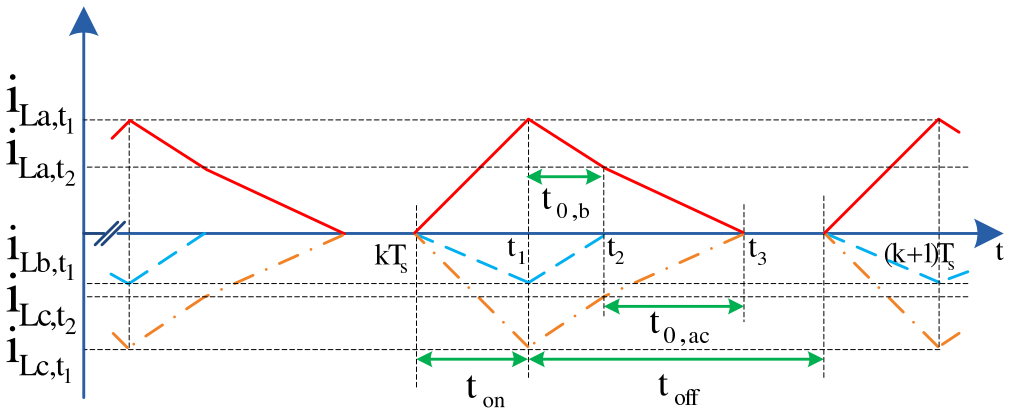


Figure 4.3: Currents in the inductors in the discontinuous conduction mode.

loss of generality, the developments presented in this section are for the case when $V_{ac} \geq 0$ and $V_{bc} \geq 0$ (first, second, and fifth rows in Table 4.1). The current profiles for charging and discharging of the inductors in a typical operating mode are shown in Fig. 4.3. It should be noted that the converter is operated in the discontinuous conduction mode (DCM) as shown in Fig. 4.3.

### 4.2.1 Mode 1: $Q_1$, $Q_2$, and $Q_3$ are ON ($kT_s \leq t \leq t_1$)

In this mode of operation, all MOSFET switches, i.e., $Q_1$, $Q_2$, and $Q_3$ are on as shown in Figure 4.2-a. Using Kirchhoffs circuit laws, and performing some algebraic manipulations in each switching interval, we have

$$\begin{aligned} \frac{di_{La}}{dt} &= \frac{1}{3L}(V_{ab} + V_{ac}) \\ \frac{di_{Lb}}{dt} &= -\frac{1}{3L}(2V_{ab} - V_{ac}) \\ \frac{di_{Lc}}{dt} &= -\frac{1}{3L}(2V_{ac} - V_{ab}) \end{aligned} \tag{4.2}$$

For simplicity, it is assumed that the values of all the three inductors are equal to $L$,

i.e., $L_a = L_b = L_b = L$. Thus, the currents in the inductors can be written as follows

$$\begin{aligned} i_{La}(t) &= i_{La}(kT_s) + \frac{1}{3L}\int_{kT_s}^{t}(V_{ab} + V_{ac})dt \\ i_{Lb}(t) &= i_{Lb}(kT_s) - \frac{1}{3L}\int_{kT_s}^{t}(2V_{ab} - V_{ac})dt \\ i_{Lc}(t) &= i_{Lc}(kT_s) - \frac{1}{3L}\int_{kT_s}^{t}(2V_{ac} - V_{ab})dt \end{aligned} \tag{4.3}$$

where $k$ is the sampling instant and $T_s$ is the switching period. In this analysis, the voltage drops across the MOSFETs are ignored when they are on. In the discontinuous conduction mode (DCM), the inductors are totally discharged within each switching cycle. Hence, the currents of inductors would reach zero before or just at the end of each switching cycle, i.e., $i_{La}(kT_s) = i_{Lb}(kT_s) = i_{Lc}(kT_s) = 0$. Moreover, let us choose the switching frequency to be much higher than the frequency content of the input source. Hence, $v_{ij}$, where $i, j = a, b, c$, is approximately constant during $t_{on}$, i.e., $v_{ij}(t) = v_{ij}(kT_s)$. Therefore, during $t_{on}$, (4.3) can be approximated as

$$\begin{aligned} i_{La}(t) &= \frac{1}{3L}(V_{ab,k} + V_{ac,k})(t - kT_s) \\ i_{Lb}(t) &= -\frac{1}{3L}(2V_{ab,k} - V_{ac,k})(t - kT_s) \\ i_{Lc}(t) &= -\frac{1}{3L}(2V_{ac,k} - V_{ab,k})(t - kT_s) \end{aligned} \tag{4.4}$$

where $v_{ij,k}$ is the value of phase-to-phase voltage $v_{ij}$ at time instant $t = kT_s$. Using (4.4), the currents in the inductors at time instant $t = t_1$ are given by

$$\begin{aligned} i_{La}(t_1) &= i_{La,t_1} = \frac{1}{3L}(V_{ab,k} + V_{ac,k})(t_{on}) \\ i_{Lb}(t_1) &= i_{Lb,t_1} = -\frac{1}{3L}(2V_{ab,k} - V_{ac,k})(t_{on}) \\ i_{Lc}(t_1) &= i_{Lc,t_1} = -\frac{1}{3L}(2V_{ac,k} - V_{ab,k})(t_{on}) \end{aligned} \tag{4.5}$$

These currents are then used as the initial conditions to find the inductor currents in mode 2 of operation, where the switches $Q_1$ and $Q_2$ are turned off and $Q_3$ is kept on.

### 4.2.2 Mode 2: $Q_1$ and $Q_2$ are turned OFF, and $Q_3$ is kept ON ($t_1 \leq t \leq t_2$)

In this mode of operation, when the switches are turned off, the stored energy in the inductors together with the energy coming from the input sources charge the battery as

depicted in Figure 4.2-b. Similar to mode 1, using Kirchhoffs circuit laws and performing algebraic manipulations, the currents through the inductors can be described by the following equations

$$\begin{aligned}\frac{di_{La}}{dt} &= \frac{1}{3L}(V_{ab} + V_{ac} - 2V_B - 2V_D)\\ \frac{di_{Lb}}{dt} &= -\frac{1}{3L}(2V_{ab} - V_{ac} - V_B - V_D)\\ \frac{di_{Lc}}{dt} &= -\frac{1}{3L}(2V_{ac} - V_{ab} - V_B - V_D)\end{aligned} \tag{4.6}$$

where $V_B$ stands for the battery voltage, and $V_D$ represents the diode voltage drop. Again, $v_{ij}(t)$ is assumed to be approximately constant during $t_{off}$, i.e., $v_{ij}(t) = v_{ij}(kT_s)$, where $i, j = a, b, c$. Therefore, the currents of the inductors can be approximated as follows

$$\begin{aligned}i_{La}(t) &= i_{La,t_1} + \frac{1}{3L}(V_{ab,k} + V_{ac,k})(t - t_1) - \frac{2}{3L}(V_B + V_D)(t - t_1)\\ i_{Lb}(t) &= i_{Lb,t_1} - \frac{1}{3L}(2V_{ab,k} - V_{ac,k})(t - t_1) + \frac{1}{3L}(V_B + V_D)(t - t_1)\\ i_{Lc}(t) &= i_{Lc,t_1} - \frac{1}{3L}(2V_{ac,k} - V_{ab,k})(t - t_1) + \frac{1}{3L}(V_B + V_D)(t - t_1)\end{aligned} \tag{4.7}$$

Substituting (4.5) into (4.7) results in

$$\begin{aligned}i_{La}(t) &= \frac{1}{3L}(V_{ab,k} + V_{ac,k})(t - t_1 + t_{on}) - \frac{2}{3L}(V_B + V_D)(t - t_1)\\ i_{Lb}(t) &= -\frac{1}{3L}(2V_{ab,k} - V_{ac,k})(t - t_1 + t_{on}) + \frac{1}{3L}(V_B + V_D)(t - t_1)\\ i_{Lc}(t) &= -\frac{1}{3L}(2V_{ac,k} - V_{ab,k})(t - t_1 + t_{on}) + \frac{1}{3L}(V_B + V_D)(t - t_1)\end{aligned} \tag{4.8}$$

Using (4.8), the currents in the inductors at the time instant $t = t_2$ are given by

$$\begin{aligned}i_{La,t_2} &= \frac{1}{3L}(V_{ab,k} + V_{ac,k})(t_{0,b} + t_{on}) - \frac{2}{3L}(V_B + V_D)t_{0,b}\\ i_{Lb,t_2} &= -\frac{1}{3L}(2V_{ab,k} - V_{ac,k})(t_{0,b} + t_{on}) + \frac{1}{3L}(V_B + V_D)t_{0,b}\\ i_{Lc,t_2} &= -\frac{1}{3L}(2V_{ac,k} - V_{ab,k})(t_{0,b} + t_{on}) + \frac{1}{3L}(V_B + V_D)t_{0,b}\end{aligned} \tag{4.9}$$

Referring to Figure 4.3, to find $t_{0,b}$, we set $i_{Lb}(t_2) = 0$. Hence

$$t_{0,b} = \frac{2V_{ab,k} - V_{ac,k}}{V_B + V_D - 2V_{ab,k} + V_{ac,k}} t_{on}. \tag{4.10}$$

Substituting (4.10) into (4.9) results in

$$i_{La,t_2} = -i_{Lc,t_2} = \frac{1}{L}\frac{(V_{ac,k} - V_{ab,k})(V_B + V_D)}{(V_B + V_D - 2V_{ab,k} + V_{ac,k})}t_{on}. \tag{4.11}$$

These currents are then used as the initial conditions to find the inductor currents in mode 3 of operation, where the inductor current of phase $b$ reaches zero.

### 4.2.3 Mode 3: $Q_1$ and $Q_2$ remain OFF and $Q_3$ is kept ON until the $i_{Lb} = 0$ $(t_2 \leq t \leq t_3)$

When $i_{Lb}$ reaches zero, the rest of the stored energy in the magnetic fields of $L_a$ and $L_c$ along with the energy coming from the corresponding input sources charge the battery until they get totally discharged as shown in Figure 4.2-c. Using a similar analysis for modes 1 and 2 of circuit operation, in each switching interval we have

$$\frac{di_{La}}{dt} = -\frac{di_{Lc}}{dt} = \frac{1}{2L}(V_{ac,k} - V_B - V_D) \tag{4.12}$$

By ignoring the voltage drop across the MOSFETs and assuming that the input voltage $v_{ij}(t)$ does not change much during each switching period, the currents in the inductors can be obtained as follows

$$\begin{aligned} i_{La}(t) &= i_{La,t_2} + \frac{1}{2L}(V_{ac,k} - V_B - V_D)(t - t_2) \\ i_{Lc}(t) &= i_{Lc,t_2} + \frac{1}{2L}(V_{ac,k} - V_B - V_D)(t - t_2) \end{aligned} \tag{4.13}$$

Referring to Figure 4.3, to find $t_{0,ac}$, lest us set $i_{La}(t_3) = i_{La}(t_3) = 0$ and substitute (4.11) into (4.13), which results in

$$t_{0,ac} = (\frac{V_{ab,k} - V_{ac,k}}{V_{ac,k} - V_B - V_D})(\frac{2t_{on}(V_B + V_D)}{V_B + V_D - 2V_{ab,k} + V_{ac,k}}) \tag{4.14}$$

Next, the value of each inductor current for each mode of operation is used to find the total charge passing through the inductor using the averaging method.

### 4.2.4 Calculation of phase-to-phase resistances using the averaging method

In this section, we utilize the expressions obtained for the inductor currents in the previous sections to derive the *averaged* instantaneous current in one switching cycle and

hence the instantaneous averaged phase-to-phase resistances as seen from the input sources. To this end, referring to Figure 4.3, we have

$$\begin{aligned}
\Delta q_a &= \frac{1}{2}[i_{La,t_1} t_{on} + (i_{La,t_1} + i_{La,t_2}) t_{0,b} + i_{La,t_2} t_{0,ac}] \\
\Delta q_b &= \frac{1}{2}[i_{Lb,t_1} t_{on} + i_{La,t_1} t_{0,b}] \\
\Delta q_c &= \frac{1}{2}[i_{Lc,t_1} t_{on} + (i_{Lc,t_1} + i_{Lc,t_2}) t_{0,b} + i_{Lc,t_2} t_{0,ac}]
\end{aligned} \tag{4.15}$$

where $\Delta q_j$ is the total charge passing through the inductor of phase $j$, i.e., $L_j$ (where $j = a, b, c$) during the time interval $kT_s \leq t \leq (k+1)T_s$. By substituting (4.5), (4.10), (4.11), and (4.14) into (4.15), and after some algebraic steps, we have

$$\begin{aligned}
\Delta q_a &= \frac{t_{on}^2}{6L}\left(\frac{V_B + V_D}{V_B + V_D - 2V_{ab,k} + V_{ac,k}}\right)(V_{ab,k} + V_{ac,k}) \\
&- \frac{t_{on}^2}{6L}\left(\frac{V_B + V_D}{V_B + V_D - 2V_{ab,k} + V_{ac,k}}\right) n_1(V_{ij,k}, V_B, V_D)
\end{aligned} \tag{4.16}$$

$$\begin{aligned}
\Delta q_c &= -\frac{t_{on}^2}{6L}\left(\frac{V_B + V_D}{V_B + V_D - 2V_{ab,k} + V_{ac,k}}\right)(2V_{ac,k} - V_{ab,k}) \\
&+ \frac{t_{on}^2}{6L}\left(\frac{V_B + V_D}{V_B + V_D - 2V_{ab,k} + V_{ac,k}}\right) n_1(V_{ij,k}, V_B, V_D)
\end{aligned} \tag{4.17}$$

where $ij = ab,\ ac,\ bc$ and the term $n_1(V_{ij,k}, V_B, V_D)$ is given by

$$n_1(V_{ij,k}, V_B, V_D) = \frac{3V_{ac,k}(V_{ac,k} - V_{ab,k})}{V_{ac,k} - V_B - V_D} \tag{4.18}$$

Furthermore,

$$\Delta q_b = -\frac{t_{on}^2}{6L}\left[\frac{V_B + V_D}{V_B + V_D - 2V_{ab,k} + V_{ac,k}}\right](2V_{ab,k} - V_{ac,k}) \tag{4.19}$$

It should be noted that all the above equations were derived by assuming that $i_{Lb} \leq i_{Lc}$, as shown in Figure 4.3. Performing a similar analysis for the case when $i_{Lb} > i_{Lc}$, we have

$$\begin{aligned} \Delta q_a &= \frac{t_{on}^2}{6L}\left(\frac{V_B + V_D}{V_B + V_D - 2V_{ac,k} + V_{ab,k}}\right)(V_{ab,k} + V_{ac,k}) \\ &- \frac{t_{on}^2}{6L}\left(\frac{V_B + V_D}{V_B + V_D - 2V_{ac,k} + V_{ab,k}}\right)n_2(V_{ij,k}, V_B, V_D) \end{aligned} \tag{4.20}$$

$$\begin{aligned} \Delta q_b &= -\frac{t_{on}^2}{6L}\left(\frac{V_B + V_D}{V_B + V_D - 2V_{ac,k} + V_{ab,k}}\right)(2V_{ab,k} - V_{ac,k}) \\ &+ \frac{t_{on}^2}{6L}\left(\frac{V_B + V_D}{V_B + V_D - 2V_{ac,k} + V_{ab,k}}\right)n_2(V_{ij,k}, V_B, V_D) \end{aligned} \tag{4.21}$$

where $ij = ab,\ ac,\ bc$ and the nonlinear term $n_2(V_{ij,k}, V_B, V_D)$ is given by

$$n_2(V_{ij,k}, V_B, V_D) = \frac{3V_{ab,k}(V_{ab,k} - V_{ac,k})}{V_{ab,k} - V_B - V_D} \tag{4.22}$$

and

$$\Delta q_c = -\frac{t_{on}^2}{6L}\left[\frac{V_B + V_D}{V_B + V_D - 2V_{ac,k} + V_{ab,k}}\right](2V_{ac,k} - V_{ab,k}) \tag{4.23}$$

The arguments of $n_2(.)$, $n_2(.)$ are dropped in the rest of this chapter for brevity. The average values of the currents in the inductors at instant $kT_s$ can then be written as

$$i_{Lj,k} = \frac{\Delta q_j}{T_s}, \quad j = a, b, c \tag{4.24}$$

Substituting (4.19) and (4.21) into (4.24) results in

$$2V_{ab,k} - V_{ac,k} = -\frac{6LT_s}{t_{on}^2}\left(1 - \frac{V_{in,bc,k}}{V_B + V_D}\right)i_{Lb,k} + \bar{S}_{bc}n_2 \tag{4.25}$$

where

$$V_{in,bc,k} = (2 - 3\bar{S}_{bc})V_{ab,k} - (1 - 3\bar{S}_{bc})V_{ac,k}$$

in which $S_{bc}$ is the control signal which can take values from the discrete set $\{0, 1\}$ as follows

$$\begin{aligned} S_{bc} &= 1, \quad i_{Lb,k} \leq i_{Lc,k} \\ S_{bc} &= 0, \quad i_{Lb,k} > i_{Lc,k} \end{aligned} \tag{4.26}$$

Also, the term $\bar{S}_{bc}$ in (4.25) is the logical complement of $S_{bc}$ (e.g., $S_{bc} = 0$ and $\bar{S}_{bc} = 1$ are equivalent).

Similarly, substituting (4.17) and (4.23) into (4.24), and using the control signal $S_{bc}$, we have

$$2V_{ac,k} - V_{ab,k} = -\frac{6LT_s}{t_{on}^2}(1 - \frac{V_{in,bc,k}}{V_B + V_D})i_{Lc,k} + S_{bc}n_1 \tag{4.27}$$

Solving equations (4.25) and (4.27) in terms of $V_{ab,k}$ and $V_{ac,k}$, results in

$$\begin{aligned} V_{ab,k} &= -\frac{4K_{bc}LT_s}{t_{on}^2}i_{Lb,k} - \frac{2K_{bc}LT_s}{t_{on}^2}i_{Lc,k} + \frac{1}{3}(S_{bc}n_1 + 2\bar{S}_{bc}n_2) \\ V_{ac,k} &= -\frac{2K_{bc}LT_s}{t_{on}^2}i_{Lb,k} - \frac{4K_{bc}LT_s}{t_{on}^2}i_{Lc,k} + \frac{1}{3}(2S_{bc}n_1 + \bar{S}_{bc}n_2) \end{aligned} \tag{4.28}$$

where

$$K_{bc} = 1 - \frac{V_{in,bc,k}}{V_B + V_D}$$

which can be further simplified to

$$V_{bc,k} = \frac{2K_{bc}LT_s}{t_{on}^2}i_{Lbc,k} + \frac{1}{3}(S_{bc}n_1 - \bar{S}_{bc}n_2) \tag{4.29}$$

where $i_{Lbc,k} = i_{Lb,k} - i_{Lc,k}$.

Equation (4.29) indicates that, at each sampling time $t = kT_s$, there exists a nonlinear resistance between two phases given by

$$R_{bc,k} = \frac{2LT_s}{t_{on}^2}(1 - \frac{(2 - 3\bar{S}_{bc})V_{ab,k} - (1 - 3\bar{S}_{bc})V_{ac,k}}{V_B + V_D}) + r_{n,bc} \tag{4.30}$$

where $R_{bc,k} = \frac{V_{bc,k}}{i_{Lbc,k}}$ and

$$r_{n,bc} = \frac{1}{3i_{Lbc,k}}(S_{bc}n_1 - \bar{S}_{bc}n_2)\cdot$$

Similarly, $R_{ab,k}$ and $R_{ac,k}$ can be obtained as follows

$$R_{ab,k} = \frac{2LT_s}{t_{on}^2}(1 - \frac{(2 - 3\bar{S}_{ab})V_{ca,k} - (1 - 3\bar{S}_{ab})V_{cb,k}}{V_B + V_D}) + r_{n,ab} \tag{4.31}$$

$$R_{ac,k} = \frac{2LT_s}{t_{on}^2}(1 - \frac{(2 - 3\bar{S}_{ac})V_{ba,k} - (1 - 3\bar{S}_{ac})V_{bc,k}}{V_B + V_D}) + r_{n,ac} \tag{4.32}$$

where $S_{ab}$ and $S_{ac}$ are defined similar to $S_{bc}$, i.e.,

$$\begin{aligned} S_{ab} &= 1, \quad i_{La,k} \leq i_{Lb,k} \\ S_{ab} &= 0, \quad i_{La,k} > i_{Lb,k} \end{aligned}$$

and

$$\begin{aligned} S_{ac} &= 1, \quad i_{La,k} \leq i_{Lc,k} \\ S_{ac} &= 0, \quad i_{La,k} > i_{Lc,k} \end{aligned}$$

Furthermore,

$$r_{n,ab} = \frac{1}{3i_{Lab,k}}(S_{ab}n_1 - \bar{S}_{ab}n_2)$$
$$r_{n,ac} = \frac{1}{3i_{Lac,k}}(S_{ac}n_1 - \bar{S}_{ac}n_2)\cdot$$

Similarly, the corresponding terms $\bar{S}_{ab}$ and $\bar{S}_{ac}$ are logical complements of $S_{ab}$ and $S_{ac}$, respectively. It is worth noting that $R_{ac,k} = R_{ca,k}$, $R_{ab,k} = R_{ba,k}$, and $R_{bc,k} = R_{cb,k}$.

Due to the resistive nature of (4.30), (4.31), and (4.32), if the circuit is operated in the discontinuous conduction mode (DCM), there is no phase difference between the phase-to-phase voltages and corresponding currents. However, it must be noted that the phase-to-phase resistance seen from the input for each phase, has a bias term, $r_{n,ij}$, and a nonlinear term given by (4.30), (4.31), and (4.32) which will be compensated by the feedback controller presented in Section 4.3.

Next, we will obtain a condition on the PWM duty cycle to achieve the above resistive relationship. Referring to Figure 4.3, the off-time of switches must be large enough to let the inductors to be completely discharged. Thus we have

$$t_{0,b} + t_{0,ac} \leq t_{off}\cdot \tag{4.33}$$

$t_{on}$ and $t_{off}$ can be written in terms of the duty cycle $d$ of PWM waveform as follows

$$\begin{aligned} t_{on} &= dT_s \\ t_{off} &= (1-d)T_s \end{aligned} \tag{4.34}$$

Substituting (4.10), (4.14), and (4.35) into (4.33), and performing some algebraic manipulations, the condition to achieve resistive performance can be obtained using the following inequality

$$d \leq 1 - \frac{V_{ac,k}}{V_B + V_D}. \tag{4.35}$$

The above relationship indicates that a *pseudo-resistive* behavior is achieved at a duty cycle that is dependent on the ratio of the phase-to-phase input voltage and the sum of the voltage drops across the diode and battery. Similar conditions can be derived for the other switching arrangements.

## 4.3 Proposed Control Strategy

Based on (4.32), (4.31), and (4.30), the parameters that can affect the value of input resistances are $T_s$, $t_{on}$, and $L$. Thus, $t_{on}$ is used to obtain the control input which can be related to $d$ for a particular $T_s$. To this end, let us define $u$, $a$, and $y$ as follows

$$\begin{aligned} u &= \frac{2LT_s}{t_{on}^2}, \quad a = V_B + V_D, \\ y_{pq} &= \frac{V_{in,pq,k}}{i_{Lp,k}}; \quad p, q = a, b, c; \quad p \neq q \end{aligned} \tag{4.36}$$

where $u$ and $a$ are both positive ($u > 0$, $a > 0$), and

$$V_{in,pq,k} = (2 - 3\bar{S}_{pq})V_{pr,k} - (1 - 3\bar{S}_{pq})V_{qr,k}$$

where $r = a, b, c$ and $p \neq q \neq r$. The values of $p$, $q$, $r$ are chosen based on the switching arrangements and phase-to-phase voltages as described in (4.1). By utilizing (4.36) and the corresponding resistive relationships between phases $p$ and $q$, i.e., (4.30), (4.31), or (4.32), we have

$$y_{pq} = u(1 - \frac{v}{a}) + r_{n,pq} \tag{4.37}$$

where $v = V_{in,pq,k}$.

Now, let us define

$$u = y_{d,pq} + \Delta u \tag{4.38}$$

where $y_{d,pq}$ is the desired input resistance of the circuit between phases $p$ and $q$. Substituting (4.38) into (4.37) results in

$$y_{pq} = (y_{d,pq} + \Delta u)(1 - \frac{v}{a}) + r_{n,pq}. \tag{4.39}$$

By defining $e_{pq} = y_{d,pq} - y_{pq}$ and using (4.39), we have

$$e_{pq} = \frac{v}{a} y_{d,pq} - \Delta u(1 - \frac{v}{a}) - r_{n,pq}. \tag{4.40}$$

Now, let us take the control input $\Delta u$ as follows

$$\Delta u = (1 - \frac{v}{a})^{-1}(w_{pq} + \frac{v}{a} y_d - r_{n,pq}) \tag{4.41}$$

where $w_{pq}$ is the output of a PI controller given by

$$w_{pq} = K_p e_{pq} + K_I \int e_{pq} dt. \tag{4.42}$$

Substituting (4.41) into (4.40) and using (4.42) results in

$$(K_p + 1)e_{pq} + K_I \int e_{pq} dt = 0 \tag{4.43}$$

Since the coefficients of the PI controller are always positive, $K_I/(K_P+1)$ is always positive, which guarantees that the error would exponentially converge to zero. The control law is then obtained by substituting (4.41) into (4.38) as follows

$$u = y_{d,pq} + (1 - \frac{v}{a})^{-1}(w_{pq} + \frac{v}{a} y_{d,pq} - r_{n,pq}) \tag{4.44}$$

which can be further simplified to

$$u = \frac{a}{a - v}(y_{d,pq} + w_{pq} - r_{n,pq}). \tag{4.45}$$

In summary, the switching arrangement is first set based on the phase-to-phase input voltages at each time instant. The value of the duty cycle, $d$, is then calculated using (4.36) and $u$ is given by (4.45). Figure 4.4 illustrates the control system block diagram in which the control input is generated by a PWM signal with the duty cycle determined by the controller.

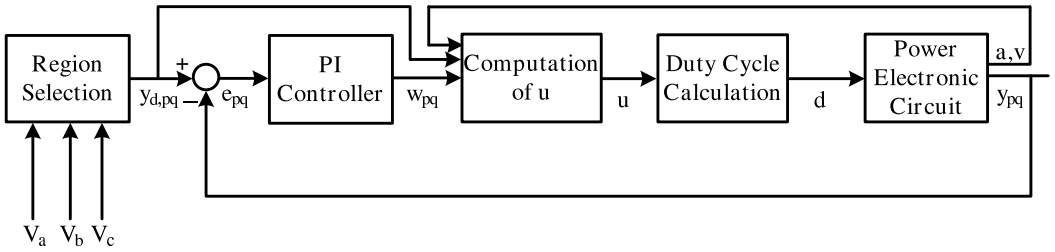


Figure 4.4: Block diagram of proposed control strategy.

## 4.4 Simulation and Experimental Results

A Simulink model of the proposed converter and its controller were developed using the SIMELECTRONICS toolbox of MATLAB with the following parameters: $L = 0.49$mH, $C = 100\mu$F, $V_B = 12$V, $V_D = 0.6$V, $V_a(t) = 0.8\sin(2\pi f_i t)$V, $V_b(t) = 0.8\sin(2\pi f_i t + \frac{2\pi}{3})$V, $V_c(t) = 0.8\sin(2\pi f_i t - \frac{2\pi}{3})$V, $K_I = 40$, $K_P = 0.01$, $f_i = 10$Hz, $f_s = 1$kHz, and $y_d = 10\Omega$; where $f_i$ and $f_s$ are the frequencies of the three-phase input signal and PWM control signal, respectively. It must be noted that $f_i$ is considered as low as 10Hz to evaluate the performance of the converter for applications involving energy harvesting from energy sources with a low-frequency content input waveform, e.g., vehicle suspension systems, low speed wind turbines, and electric bike regenerative systems. To remove the 1kHz switching harmonics, a 50Hz low-pass filter was used for all shown graphs. Figure 4.5 illustrates the variation of input resistance $R_{ab}$ between phases $a$ and $b$ versus the PWM duty cycle and comparing the values with the resistive formula given by (4.31) when $\frac{V_{in,ab}}{V_B+V_D}$ and $r_{n,ab}$ are small enough to be ignored. Figure 4.5 indicates that the simulated values are close to the corresponding theoretical ones obtained from (4.31).

Figure 4.6 indicates that there is no phase difference between the phase-to-phase input voltage $V_{ab}$ and corresponding current $i_{Lab}$. Also, from Figure 4.7, it is evident that controller can provide resistive behavior even in the presence of an arbitrary band-limited signal with time-varying amplitude and frequency. Figure 4.8 shows the performance of the converter along with the controller for a step-changed desired phase-to-phase input resistance. It reveals that using the proposed control scheme and switching arrangement, the desired resistance can be achieved right after setting the input resistance to a different value.

To evaluate performance of the circuit experimentally, the circuit shown in Figure 4.1 was

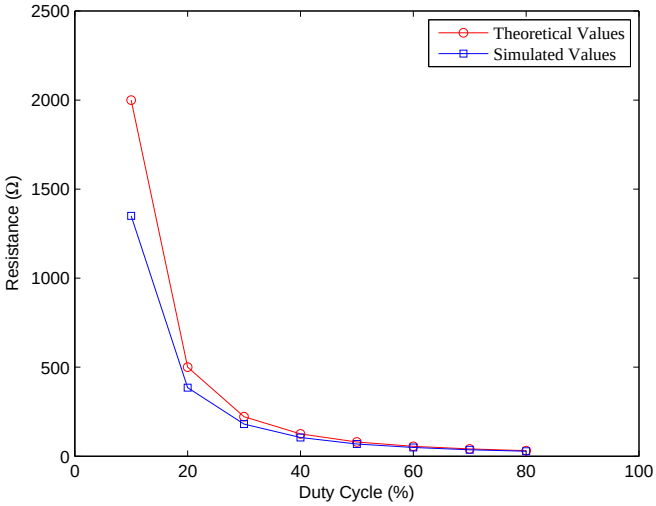


Figure 4.5: Theoretical and simulated values of the resistances seen from phases $a$ and $b$ ($R_{ab}$).

built using the following components: $Q_1$, $Q_3$: N-channel MOSFETs, 75V, 90A (IRFP2907) with internal diodes $D_4$, $D_5$, and $D_6$; $D_1$, $D_3$: Schottky diodes, 60V, 20A (MBR4060WT); $B$: Sealed lead acid battery, 12V, 7Ah; $C$: Electrolyte capacitor, 100$\mu$F, 25$V$. A dynamo system including a synchronous permanent magnet DC generator was used to generate the three-phase input signals as shown in Figure 4.9. The internal inductance of the generator was $L = 0.49$mH for each phase which were utilized to act as the boost converter inductors. The current passing through the inductors, the input voltages, and input currents were measured using LT1167 instrumentation amplifiers. These signals along with the battery voltage were then captured by ADC channels of dSPACE 1103 (from *dSPACE, Inc.*). These data were sent to a PC workstation running MATLAB/SIMULINK through a fiber optic link connecting dSPACE to the PC. The phase-to-phase resistances seen from input of converter ($y$) were then calculated by dividing the captured input voltage over the averaged inductor current. The controller was implemented on the dSPACE DSP board using the MATLAB Real-Time Workshop. The PWM signal was generated based on the value of $d$ obtained from (4.42), (4.45), and (4.36) at each sampling instant.

The performance of the controller was then investigated by setting desired resistance $R_d = 10\Omega$. The results for one of the phase-to-phase input voltages and the corresponding

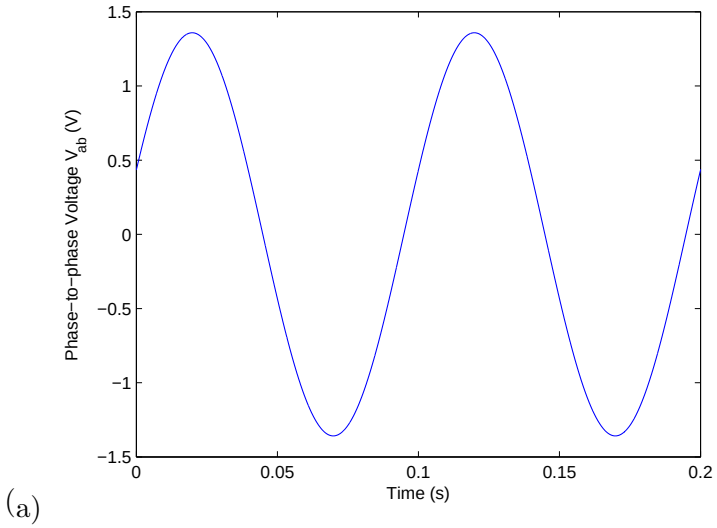


(a)

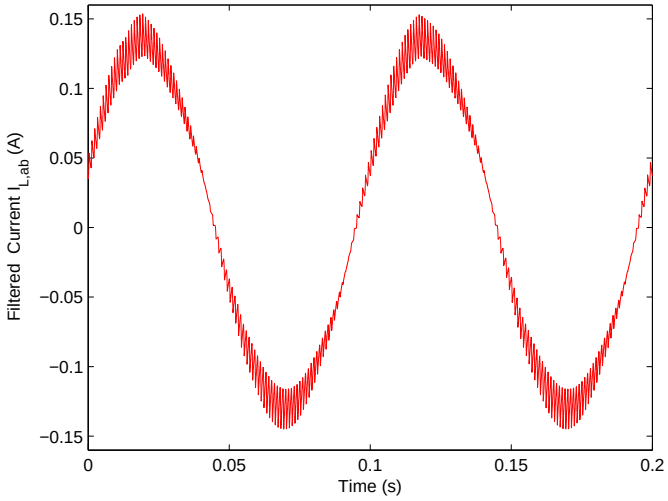


(b)

Figure 4.6: Simulation results for a desired resistance of $R_d = 10\Omega$: (a) Phase-to-phase input voltage $V_{ab}$, (b) corresponding current $i_{Lab}$.

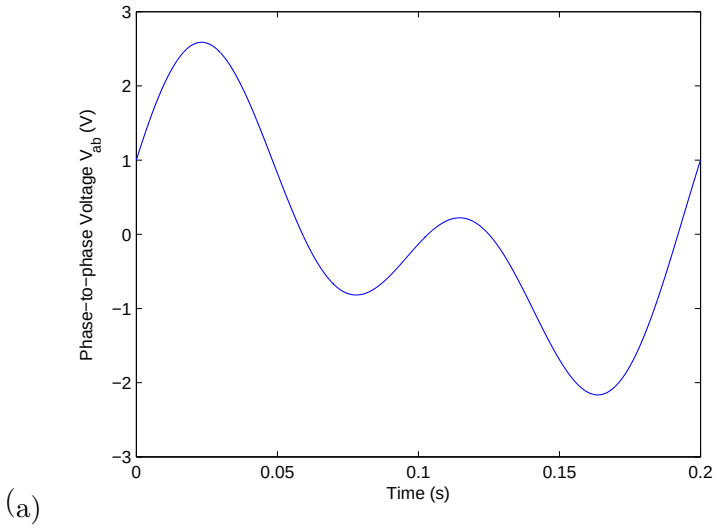


(a)

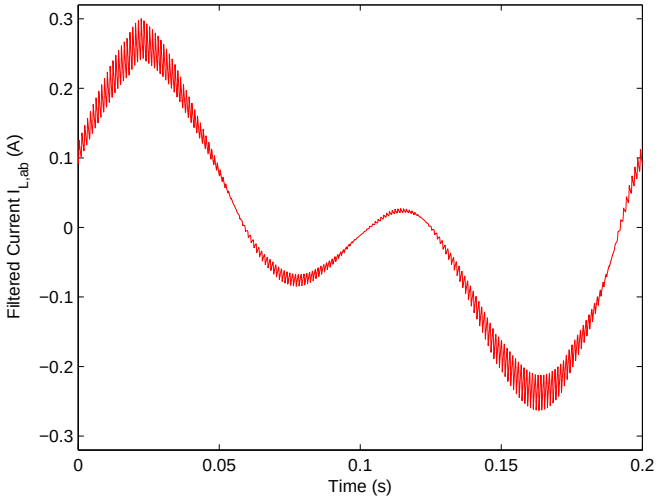


(b)

Figure 4.7: Simulation results for the closed-loop controller with a desired input resistance $R_d = 10\Omega$ subjected to an arbitrary band-limited input source: (a) Phase-to-phase input voltage $V_{ab}$, (b) corresponding current $i_{Lab}$.

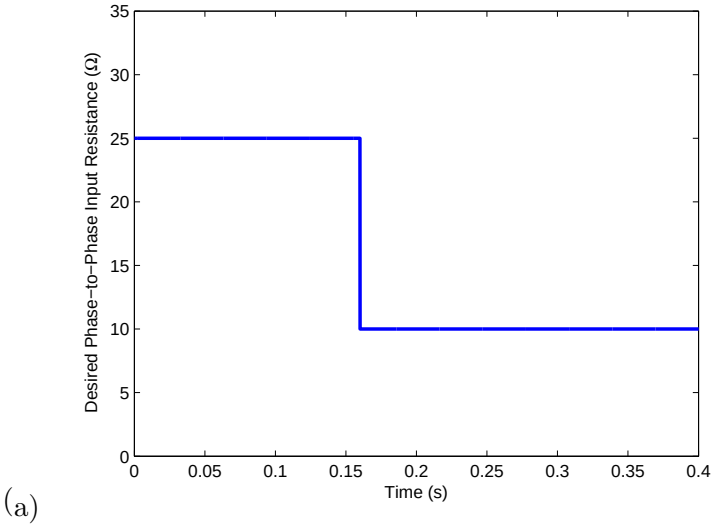


(a)

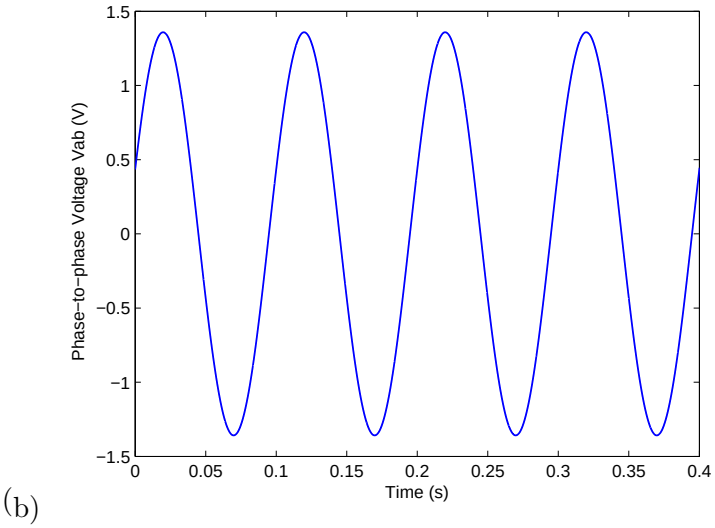


(b)

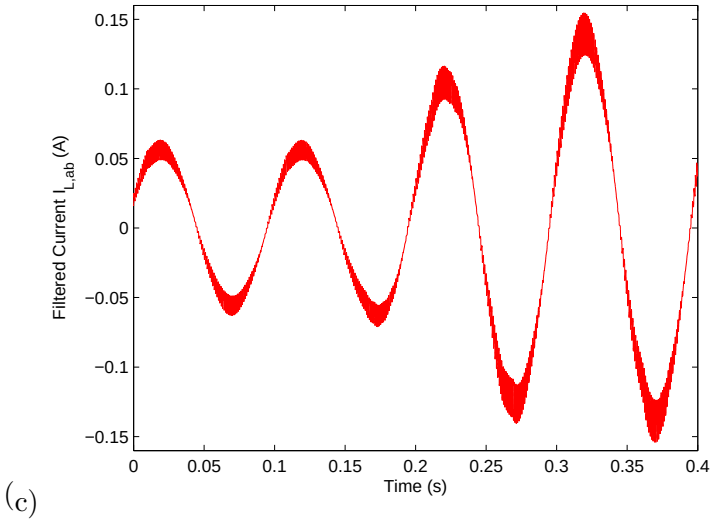


(c)

Figure 4.8: Simulation results for a step-changed desired phase-to-phase input resistance: (a) Desired phase-to-phase input resistance, (b) Phase-to-phase input voltage $V_{ab}$, (c) corresponding current $i_{Lab}$.

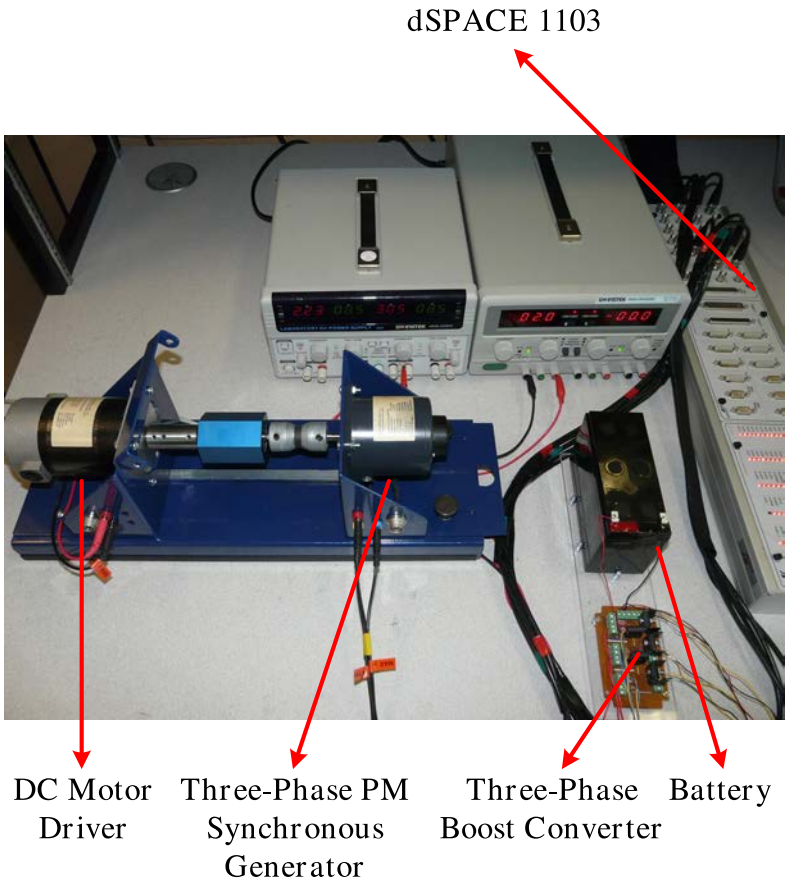


Figure 4.9: Experimental setup.

current are shown in Figure 4.10, which indicate that the input current follows the phase-to-phase input voltage with no phase difference and with a ratio corresponding to the desired resistance.

The performance of the converter along with the controller was also investigated experimentally for a step-changed desired phase-to-phase input resistance to observe the dynamic results as well as steady state results. Figure 4.11 reveals that using the proposed control scheme and switching arrangement, the desired resistance can be achieved right after setting the input resistance to a different value which means controller is fast enough to be used in real time applications. Also, the robustness of the controller was investigated through several experiments. It was observed that the controller was able to regulate the

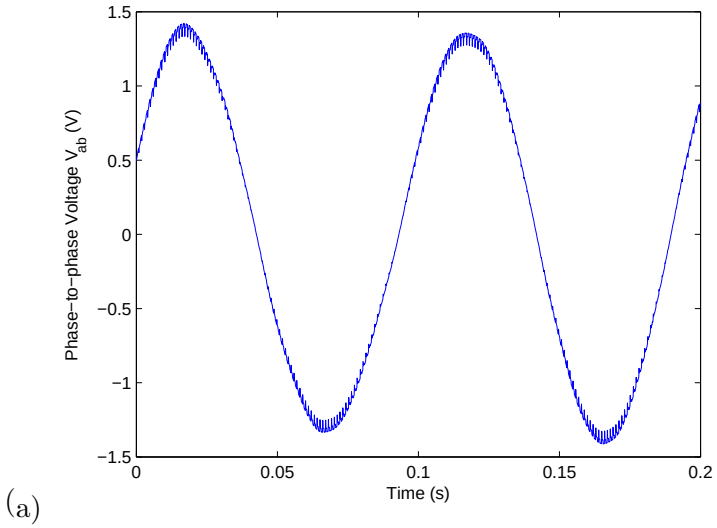


(a)

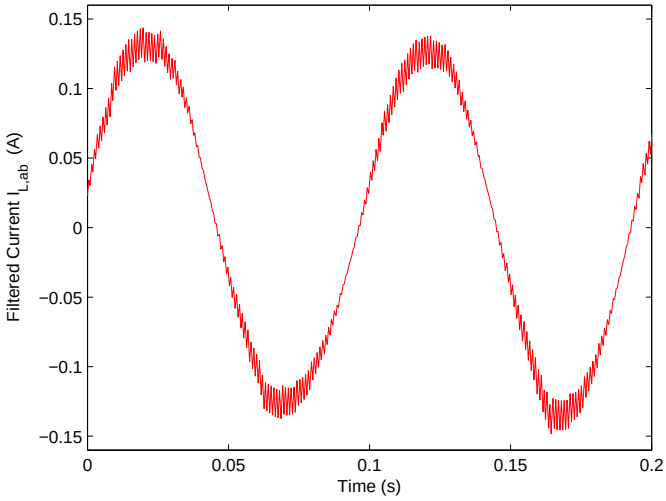


(b)

Figure 4.10: Experimental results for a desired resistance of $R_d = 10\Omega$: (a) Phase-to-phase input voltage $V_{ab}$, (b) corresponding current $i_{Lab}$.

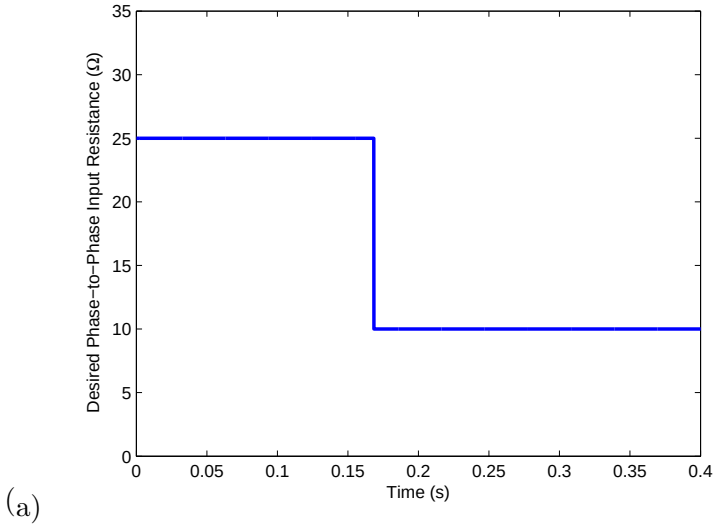


(a)

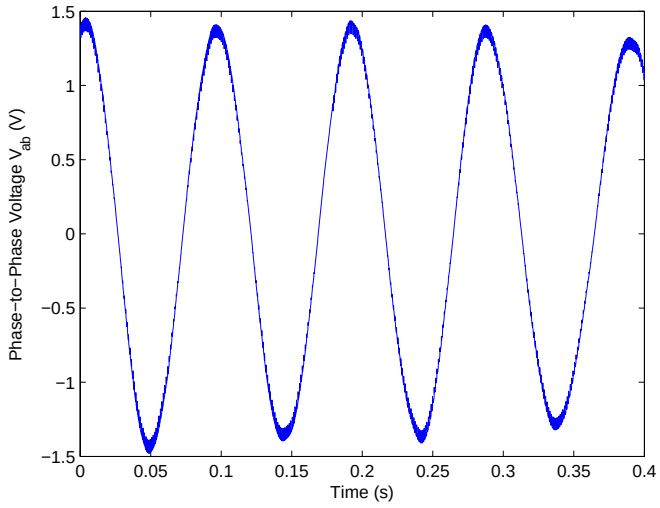


(b)

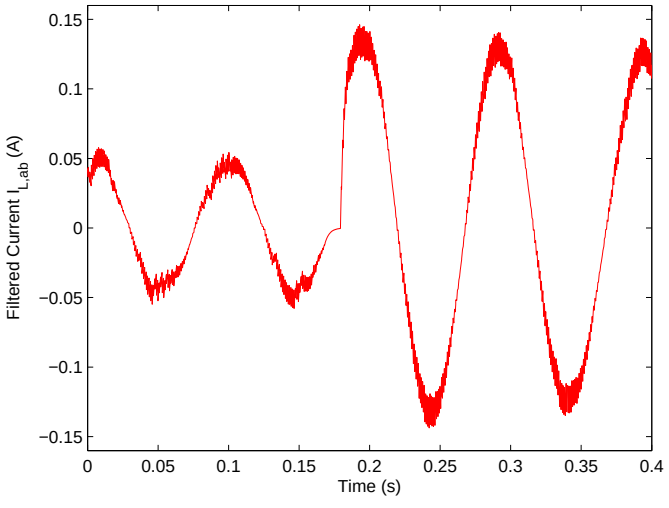


(c)

Figure 4.11: Experimental results for a step-changed desired phase-to-phase input resistance: (a) Desired phase-to-phase input resistance, (b) Phase-to-phase input voltage $V_{ab}$, (c) corresponding current $i_{Lab}$.

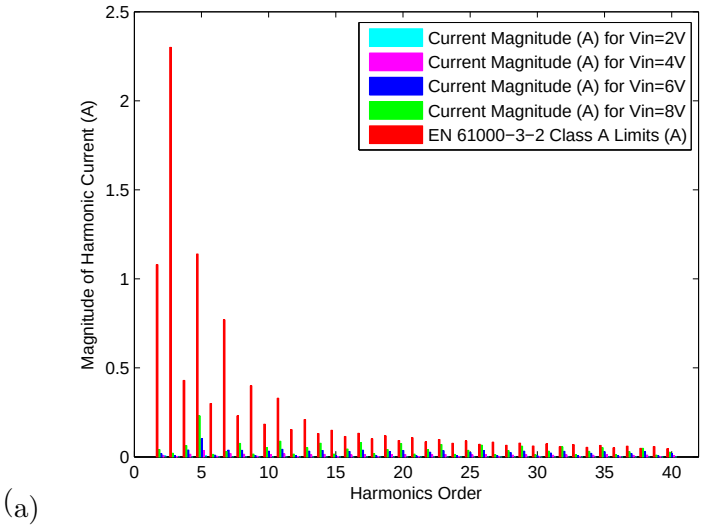


(a)

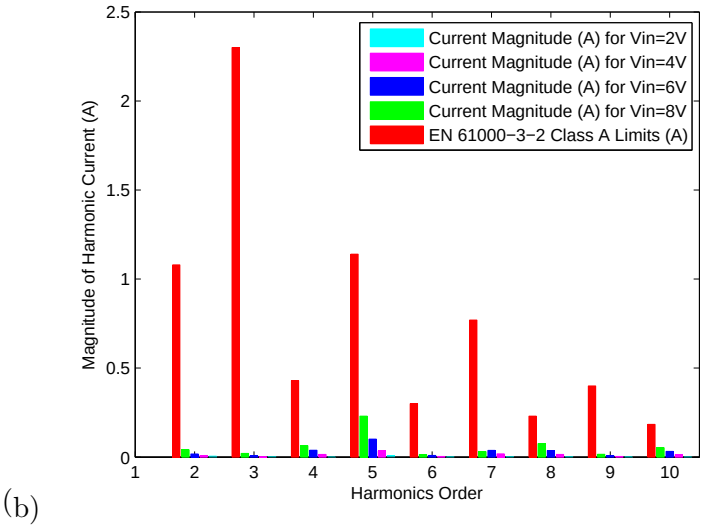


(b)

Figure 4.12: Input current harmonics for different amplitudes of input voltage for one phase of the converter: (a) All harmonics up to 40, (b) The first 10 harmonics.

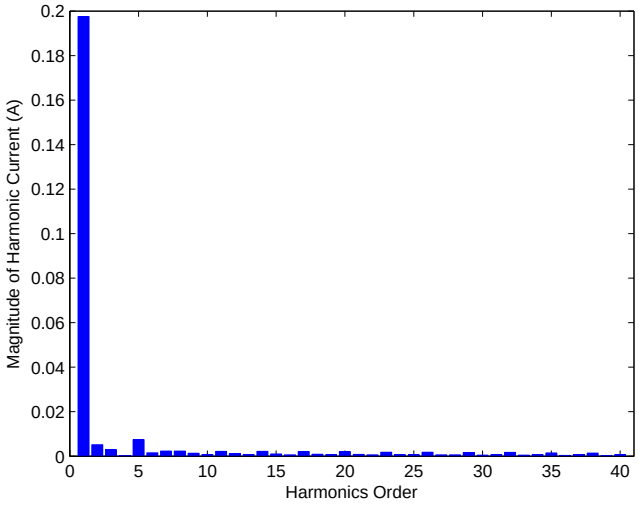


Figure 4.13: One phase input current harmonics along with the fundamental harmonic for input amplitude of 2V.

input resistance and was robust to changing circuit parameters such as battery voltage and inductors. For instance, the results reveal that the controller was capable of providing the desired resistance even if the battery voltage was changed by ±50% in 1ms. Also, it was observed that the desired resistance can be achieved even with a ±30% unbalanced values of phase inductors. Moreover, the results show that a significant increase in the amplitude of three-phase input voltage would not deteriorate performance of the controller, in terms of keeping the resistive behavior, as long as the amplitude of input voltage remains lower than the battery voltage.

In order to verify the quality of the input current in the proposed topology, the harmonics of one of the phase currents up to the $40^{th}$ harmonic were obtained and compared with the EN 61000-3-2 standard [148] in Figure 4.12-a for 2, 4, 6, and 8V amplitude of three-phase sinusoidal input signals. For more clarity, the first 10 harmonics are shown in Figure 4.12-b. This figure reveals that all converter harmonics are well below IEC standard. Also Figure 4.13 illustrates the harmonics of one of the phase currents up to the $40^{th}$ harmonic along with the fundamental harmonic for a 2V sinusoidal input signal. Thus the magnitude of all harmonics are much smaller than the fundamental harmonic. Hence, Figures 4.12 and 4.13 demonstrate that by using the proposed switching regime and control algorithm, the

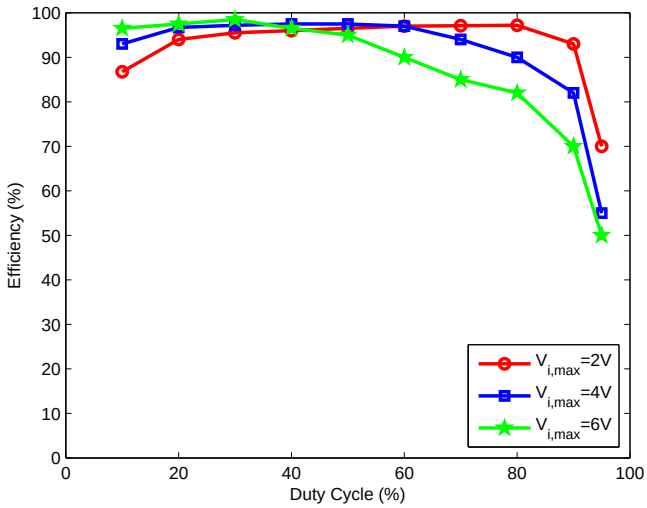


Figure 4.14: Converter efficiency versus different values of the duty cycle for different value of the amplitudes of three phase input signal.

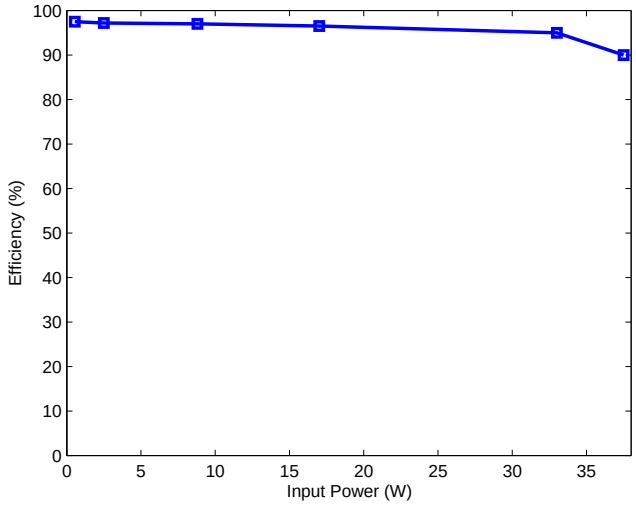


Figure 4.15: Converter efficiency for different input power.

converter draws a low harmonic sinusoidal current from the AC line in phase with the sinusoidal line voltage. As a result, the harmonic distortion is quite low and the power factor is close to unity.

Finally, the efficiency of the proposed converter was investigated by calculating the electrical power at the input and output of the converter. Figure 4.14 illustrates the efficiency against different values of the duty cycle of the PWM signal and different values of the amplitude of three phase input signal. As shown in this figure, the efficiency for higher range of three phase input amplitude is higher than the others. For all experiments, the efficiency is over 95% when the duty cycle is above 20%. The efficiency decreases when the duty cycle is increased. However, the efficiency drop takes place sooner for a higher range of amplitude since the duty cycle of the PWM control signal reaches the DCM boundary at lower values of the duty cycle, which consequently causes the circuit not to operate in the resistive region because of the inductive behavior in the CCM. Moreover, Figure 4.15 reveals that the efficiency remains almost constant for a wide range of power from; few milli-Watts up to tens of Watts. It must be noted that the aforementioned efficiencies were obtained by considering all possible losses of the circuit such as switching, diodes, and inductor losses. The efficiency can be increased further by using lower power/voltage MOSFETs.

## 4.5 Summary and Conclusions

In this chapter, analytical expressions describing the input characteristic of a three-phase boost-type converter were derived, based on which a feedback controller was designed to achieve a desired resistive input behavior. It is shown that the circuit exhibits a nonlinear resistive behavior at the input as long as the duty cycle of the control signal remains below a specific bound. The analytic expressions for this resistive behavior were utilized to derive a feedback control scheme along with the corresponding component values and switching frequencies. Furthermore, performance of the converter with feedback control was demonstrated through simulation and experimental studies for a low power conversion application. The results indicate that one can successfully enforce a *linear* resistive behavior between each two phases of the input by using the proposed switching regime and control algorithm. The values of phase-to-phase resistances can be changed by changing the desired set points applied to the controller. The proposed solution enables real-time variation of

the generator loading using high efficiency switching power devices. This feature is attractive in several renewable energy conversion systems such as low speed wind, wave energy conversion, and regenerative suspension and braking in electric vehicle applications.

# Chapter 5

# A Regenerative Suspension System using a Rotary Permanent-Magnet Machine

In this chapter we apply the results obtained in chapter 4 to develop a regenerative damper using a permanent magnet three-phase sysnchronous machine. The system consists of a mass-spring unit coupled with an algebraic screw, a brushless 3-phase rotary machine, a three-phase boost charger, and a battery. The algebraic screw converts translational vibrations into rotary motion which drives the rotary machine. The induced voltage in the rotary machine is converted into battery charge through the pulse-width-modulated three-phase boost converter developed earlier in Chapter 4. The three-phase converter enforces a resistive behavior between each two phases of the rotary machine resulting in energy-regenerative damping. This chapter is organized as follows. The modeling of the rotary machine utilized in this work presented in Section 5.2. Adapted from the work by [149], an overview of the translational to rotary converter mechanism, referred to as the *algebraic screw*, is presented in Section 5.3. In Section 5.4, the equation of motion of the rotary regenerative suspension sytem is derived. Experimental results are presented in Section 5.5 that demonstrate the performance of the regenerative damper on a suspension system testbed similar to the one discussed earlier in Chapter 3. Finally, summary and conclusions are presented in Section 5.6.

## 5.1 Introduction

As discussed before, the amount of energy dissipated in a conventional suspension systems is worthy to be recycled into electric energy as indicated by simulation results in [150]-[151], which reveal that the dissipated energy of four dampers in a passenger car traversing a poor roadway at 13.4m/s reaches approximately 200W. The proposed methods for regenerative suspension system include hydraulic, linear electromagnetic, and rotary electromagnetic mechanisms. In the hydraulic mechanism, a hydraulic motor is coupled with an electric generator to provide damping through harvesting the induced vibration energy due to the road profile [152]. This type of regenerative damper can be conveniently retrofitted into vehicles but has a low efficiency and relatively large response times. Using a linear electromagnetic machine, a mechanism similar to the concept in Chapter 3 can be developed to act as an active or semi-active damper for road induced vibrations while recuperating the vibration energy. For example, Bose, Inc., has manufactured an active damper using a linear machine [153]. This damper has a fast time response capable of changing the damping ratio in one millisecond; however, its cost and power consumption are very high. In addition, there may be a limited space in applications requiring a large vertical motion (e.g., large trucks). In contrast, a rotary electromagnetic damper uses a rotary motor coupled with a device that converts translational movement into rotary motion [11], [13], [154]. In [11] the authors present an a regenerative suspension system using a rotary motor connected to a ball-screw and nut mechanism. An experimental energy-regenerative electrical suspension system was developed in [13], which is composed of a permanent-magnet DC motor with a ball screw and a nut. Based on the reported experimental results, the suspension system can achieve a good degree of shock isolation from road excitation for low frequencies; however, ride performance in high frequencies was worse than that of a passive suspension. An electromagnetic damper consisting of a DC motor and a ball-screw mechanism was also presented in [154] but not equipped with energy-regeneration control.

## 5.2 Modeling of the Three-phase Machine used in the Suspension Testbed

Mechanical vibrations in a vehicular suspension system produce reciprocating motion which has to be converted into rotary motion if a rotary machine is to be used. When


Figure 5.1: Permanent-magnet rotary machine.

compared to their linear counterparts, brushless rotary machines are more cost-effective and can be manufactured with significantly smaller dimensions. For example, the 1kW machine for a marine wave converter developed in [155] weighs about 1800kg with a height of 3.3m and a diameter of 1.3m, whereas a 1kW rotary machine would be significantly smaller in dimensions 27cm by 11cm (see e.g., [156]), or about 1% of the volume of the linear machine reported in [155]. The rotary machine used in this research is shown in Figure 5.1. The machine is essentially an actuator, but in this work it was used as a generator to convert rotary motion into electric voltage.

The rotor of the machine shown in Figure 5.1 is an electromagnet, whereas the stator consists of three-phase windings spaced 120 electrical degrees apart around the surface of the machine. When the rotor is turned by a prime mover, i.e., through an algebraic screw in this case, it produces a rotating magnetic field and consequently three voltage waveforms in the stator coils. The equation for the induced voltage in one phase of the stator wire loop is given by [157]

$$e = (v \times B) \cdot l \tag{5.1}$$

where $v$ is the velocity of the wire loop relative to the magnetic field, $l$ represents the length of conductor in the magnetic field, and $B$ represents the magnetic flux density vector as follows

$$B = B_M \cos(\omega t - \alpha) \tag{5.2}$$

where $\alpha$ is related to the initial magnetic flux and $\omega$ is the angular velocity. It should be noted that (5.1) is for the case of a moving wire in a stationary magnetic field. In our case, the wire is stationary and the magnetic field is moving. To utilize the above equation, we must be in a frame of reference where the magnetic field appears to be stationary. Figure 5.2-a illustrates the magnetic field vector and velocities from the point of view of a stationary magnetic field and a moving wire. Thus, the total voltage induced in the coil will be the sum of voltages induced in each of its four sides in 5.2-b as follows

$$e_{ind} = e_{dc} + e_{cb} + e_{ba} + e_{ad} \tag{5.3}$$

Since $e_{cb}$ and $e_{ad}$ are zero, we have

$$e_{ind} = e_{dc} + e_{ba} = vB_M l \cos\omega t - vB_M l \cos(\omega t - 180^o) \tag{5.4}$$

From $v = r\omega$, the induced voltage can be expressed as

$$e_{ind} = \phi\omega \cos\omega t \tag{5.5}$$

where $\phi = 2rlB_M$ represents the flux passing through the coil. Equation (5.5) describes the voltage induced in a single-turn coil. Thus, for a stator with $N$ turns of wire, the total induced voltage is

$$e_{ind} = N\phi\omega \cos\omega t\cdot \tag{5.6}$$

Notice that the voltage produced in the stator of this machine winding is sinusoidal with an amplitude which depends on the flux $\phi$, rotor angular velocity $\omega$, and a constant depending on the construction of the machine $N$.

If three coils, each with $N$ turns, are placed around the rotor's magnetic field as shown in Figure 5.3, then the voltages induced in each coil will have the same magnitude but differ in phase by 120 degrees as follows

$$\begin{aligned} e_{a\acute{a}} &= N\phi\omega \cos\omega t \\ e_{b\acute{b}} &= N\phi\omega \cos(\omega t - 120^o) \\ e_{c\acute{c}} &= N\phi\omega \cos(\omega t - 240^o) \end{aligned} \tag{5.7}$$

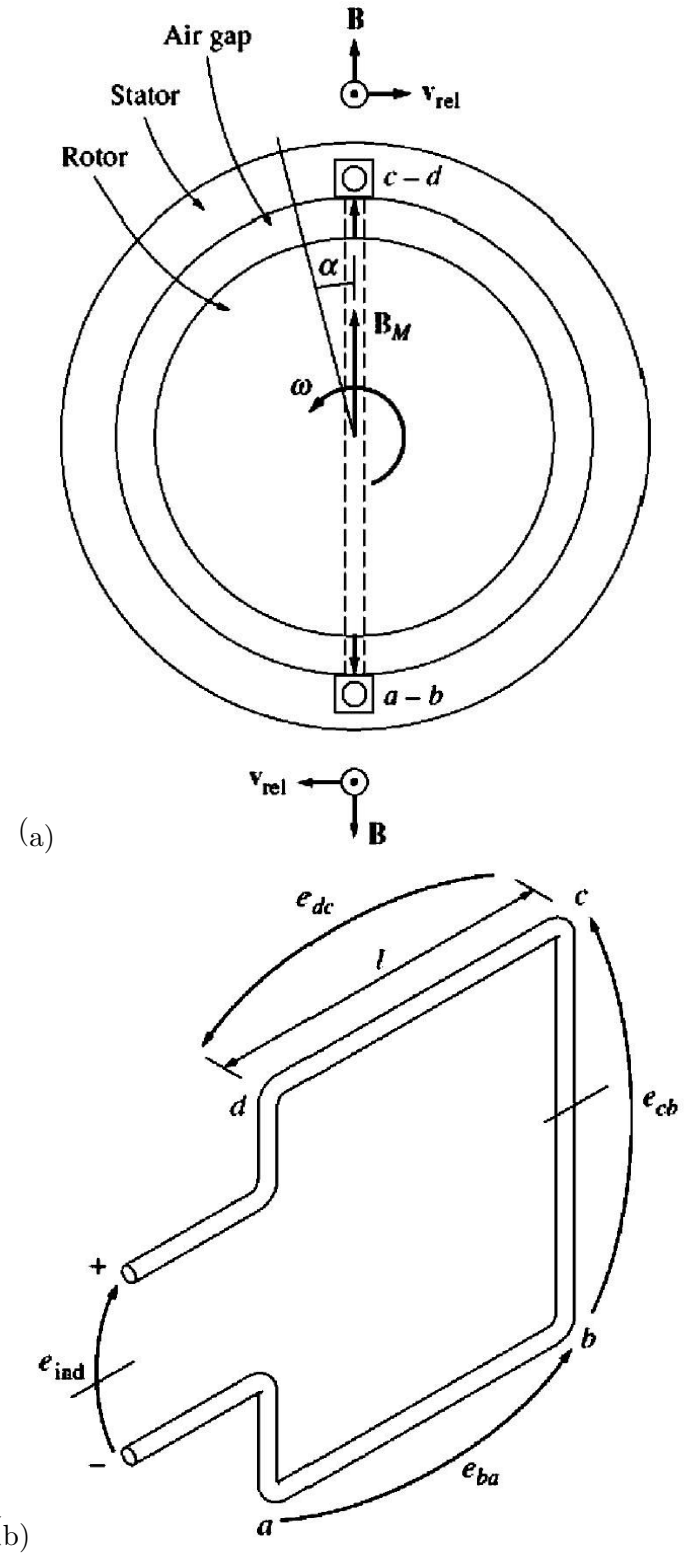


Figure 5.2: A brushless rotary machine: (a) Magnetic flux densities and velocities on the coils. The velocities shown are from a frame of reference in which the magnetic field is stationary, (b) Induced voltages in each side of a typical single-turn coil of stator [157].

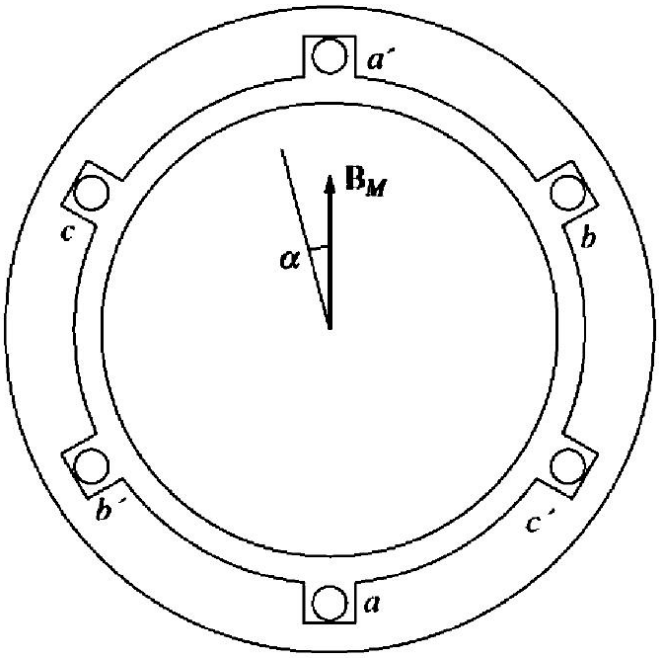


Figure 5.3: Three coils spaced $120^o$ apart [157].

Therefore, the peak voltage in any phase of a three-phase stator is given by

$$E_{max} = N\phi\omega \tag{5.8}$$

Since $\omega = 2\pi f$, this equation can be also written as

$$E_{max} = 2\pi N\phi f \tag{5.9}$$

Therefore, the root-mean-squared (rms) voltage of any phase is given by

$$E_A = \sqrt{2}\pi N\phi f \tag{5.10}$$

For the sinusoidal steady state, the RMS voltage at the terminals of the machine will depend on whether the stator is Y-connected or $\Delta$-connected. If the machine is Y-connected, then the terminal voltage will be $\sqrt{3}$ times $E_A$; if the machine is $\Delta$-connected, then the terminal voltage will be juste qual to $E_A$. Equation (5.10) can be further simplified to

$$E_A = K\phi\omega \tag{5.11}$$

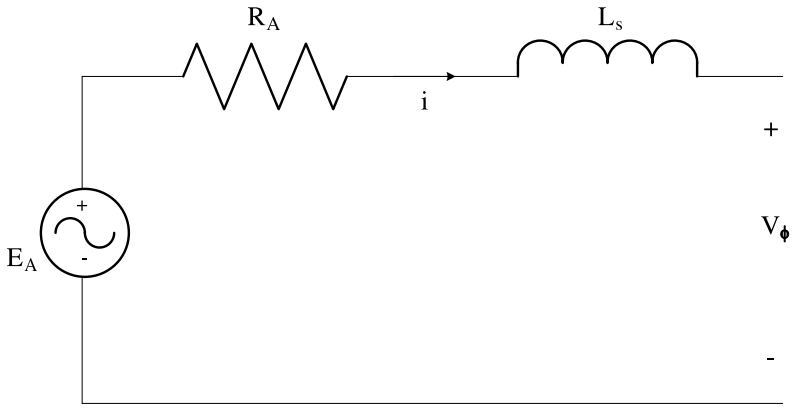


Figure 5.4: Equivalent electrical model of one phase of the rotary machine.

where $K$ is a constant representing the construction of the machine. If $\omega$ is expressed in electrical radians per second, then

$$K = \frac{N}{\sqrt{2}} \tag{5.12}$$

Similarly, if $\omega$ is expressed in mechanical radians per second, then

$$K = \frac{NP}{\sqrt{2}} \tag{5.13}$$

where $P$ is the number of poles which comes from the ratio between the rate of rotation of the magnetic fields in the machine and the stator electrical frequency given by

$$f_e = \frac{n_m P}{120} \tag{5.14}$$

where $f_e$ is electrical frequency in Hz, and $n_m$ represents the mechanical speed of the magnetic field in revolutions per minite (rpm).

The voltage $E_A$ is the internal generated voltage produced in one phase of the machine. However, this voltage $E_A$ is not usually the voltage that appears at the terminals of the machine. In fact, the only time the internal voltage $E_A$ is the same as the output voltage $V_\phi$ of a phase is when there is no armature current flowing in the machine. There are a number of factors that that result in a difference between $E_A$ and $V_\phi$ such as distortion

of the air-gap magnetic field by the current flowing in the stator winding, called armature reaction, the self-inductance of the armature coils, and the resistance of the armature coils. The armature reaction is modeled as an inductor $L$ in series with the internal generated voltage since this effect induces a voltage which lies at an angle of $90^o$ behind the plane of current and directly proportional to the current. In addition to the effects of armature reaction, each stator coil has a self-inductance $L_A$ and resistance $R_A$. Therefore, the model of one phase of machine can be shown as in Figure 5.4, where $L_s = L + L_A$. Hence, a more accurate equation for $V_\phi$ is as follows

$$V_\phi = E_A - L_s \frac{di}{dt} - R_A i \tag{5.15}$$

## 5.3 Algebraic Screw and Rotor Dynamics

This section provides an overview of the work reported in [149] which is repeated here to provide the necessary background to the reader. The Algebraic screw is a kinematic mechanism including two triangular base plates connected to each other via six legs as shown in Figure 5.5. In this figure, a particular configuration called the midline-to-vertex configuration is depicted in which a leg with an anchor point on one of the vertexes of the fixed base, has an anchor point on the midpoint of the other edges of the triangle on the moving platform. Figure 5.6 illustrates the shape of the fixed base and moving platform of the algebraic screw. This mechanism was inspired by a work reported in [158]-[160]. In this research, the algebraic screw concept is utilized as a linear-to-rotary converter that interfaces between the rotary machine and reciprocating vibration motion.

Referring to Figure 5.7-a, the relationship between the distance $d$ and rotation angle $\alpha$ is obtained as follows

$$d^2 = l^2 - \frac{a^2}{12}(5 - 4\cos\alpha) \tag{5.16}$$

where $l$ is the length of each leg and $a$ represents the length of each side of the triangle. Let us define the relative translational displacement $x$ and the relative rotational movement $\theta$ from the static equilibrium points as follows

$$d - d_0 = x \tag{5.17}$$

$$\alpha - \alpha_0 = \theta \tag{5.18}$$

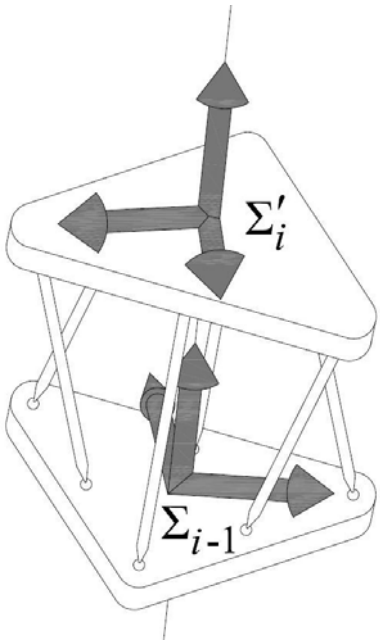


Figure 5.5: Algebraic screw with the midline-to-vertex configuration [160].

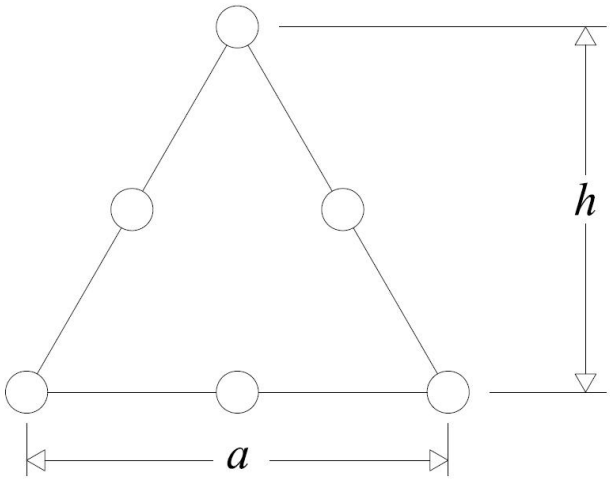


Figure 5.6: Fixed base and moving platform of the algebraic screw concept [160].

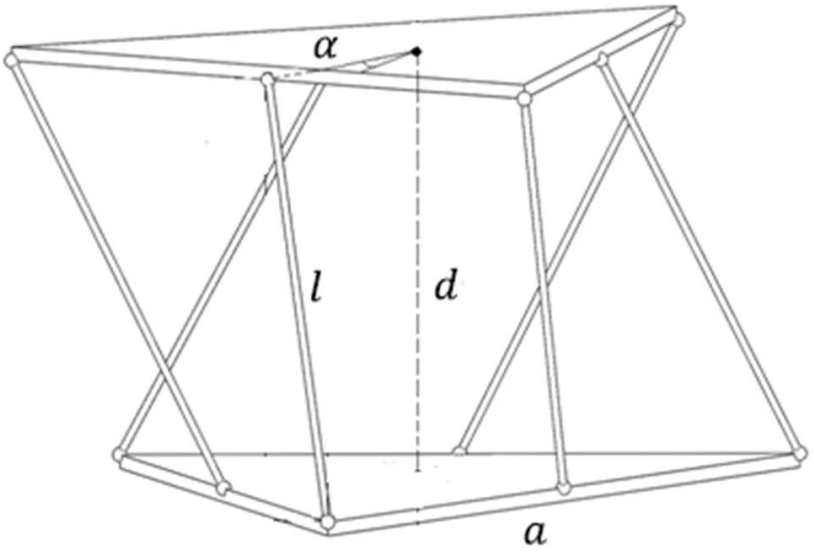


(a)

(b)

Figure 5.7: The algebraic screw: (a) Schematic diagram, (b) Developed prototype [149].

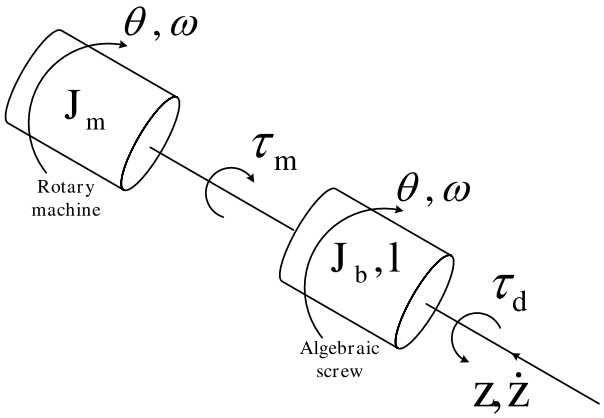


Figure 5.8: Rotor model of the electromagnetic damper.

where $d_0$ and $\alpha_0$ are the static equilibrium points corresponding to $d$ and $\alpha$, respectively. Using (5.16), (5.17), and (5.18), and performing some algebraic manipulations and linearization around the equilibrium points, we have

$$\dot{x} = c\dot{\theta} \tag{5.19}$$

where

$$c = -\frac{a^2 \sin \alpha_0}{6d_0} \tag{5.20}$$

Since the rotary machine is coupled with the algebraic screw, the angular velocity of the rotor is equal to relative rotational speed of the algebraic screw, i.e., $\omega = \dot{\theta}$. Therefore, using (5.8) and (5.19), the peak induced voltage in one phase of the stator is given by

$$E_{max} = \frac{N\phi}{c}\dot{x} \tag{5.21}$$

This equation reveals that the peak induced voltage in the stator is proportional to the linear velocity $\dot{x}$, flux $\phi$, and constants $c$ and $N$ that depend on the construction of the algebraic screw and machine, respectively.

Now, let us find the output force of electromagnetic damper consisting of the algebraic screw coupled with the rotary machine. Figure 5.8 shows the rotor dynamics components, where $J_m$ is the moment of inertia of the rotor; $J_a$ is the moment of inertia of the algebraic screw; $l$ is the distance between the two triangular plates of the algebraic screw; $\theta$ and $\omega$

are the angular displacement and velocity, respectively; and $z$ and $\dot{z}$ are the translational relative displacement and velocity, respectively, i.e., $z = x_b - x_r$ and $\dot{z} = \dot{x_b} - \dot{x_r}$. The rotor and algebraic screw are assumed to be rigid and the torsional flexibility of the algebraic screw is ignored. Refereing to Figure 5.8 we have

$$(J_m + J_a)\dot{\omega} = \tau_m - \tau_d \tag{5.22}$$

where $\tau_d$ is the total damping torque and $\tau_m$ is the output torque of the rotary machine which is proportional to the machine current $i$ as follows

$$\tau_m = k_t i\cdot \tag{5.23}$$

Using the force balance equation we have

$$f_d = \frac{2\pi}{l}\tau_d \tag{5.24}$$

where $f_d$ is the total damping force. Replacing $x$ with $z$ in (5.19) using (5.22), (5.23), (5.24), and performing some algebraic manipulations, the total damping force is obtained as follows

$$f_d = k_m i - I_d \ddot{z} \tag{5.25}$$

where

$$k_m = \frac{2\pi}{l}k_t \tag{5.26}$$

and

$$I_d = \frac{2\pi}{lc}(J_m + J_a)\cdot \tag{5.27}$$

## 5.4 Dynamic Equations of the Regenerative Suspension System including the Algebraic Screw and Rotary Machine

By utilizing the kinematic and dynamic equations for the algebraic screw, rotary machine, and the suspension system, we can obtain the dynamics of the overall suspension system. Similar to Chapter 3, it is assumed that the unsprung mass $m_w$ is negligible compared to $m_b$, and the tire stiffness $K_w$ is relatively large. Also, the mass of electromagnetic damper including the algebraic screw and the rotary machine and its friction effects are

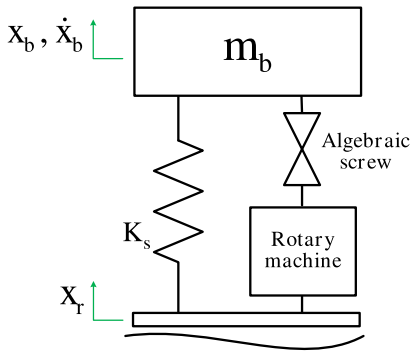


Figure 5.9: One-degree-of freedom model of the suspension system using the algebraic screw.

ignored. Therefore, an approximate one-degree-of freedom (1-DOF) system is considered as shown in Figure 5.9, where $m_b$ and $K_s$ represent a quarter of the sprung mass of a vehicle body and the stiffness of the spring, respectively. Using a free-body diagram, the equations of motion for this system are given by

$$m_b\ddot{x_b} = -K_s(x_b - x_r) - f_d \tag{5.28}$$

Substituting (5.25) into (5.28) results in

$$(m_b - I_d)\ddot{z} + K_s z = -k_m i + F_r \tag{5.29}$$

where

$$F_r = -m_b\ddot{x_r}. \tag{5.30}$$

Following the concept discussed in Chapter 4, the power electronic converter along with the controller enforce a resistive behavior across each two phases of rotary machine. Thus, the maximum current drawn for one coil of machine is given by

$$i = \frac{E_{max}}{R} \tag{5.31}$$

where

$$R = R_{desired} + R_A \tag{5.32}$$

where $R_{desired}$ represents the desired input resistance enforced by the controller as indicated in (4.30), (4.31), and (4.32). Using (5.21), (5.29), and (5.31), the equations of motion for

the proposed regenerative suspension system can be written as

$$(m_b - I_d)\ddot{z} + C_r\dot{z} + K_s z = F_r \tag{5.33}$$

where $C_r$ represents the equivalent rotary damping of the regenerative suspension system, which is given by

$$C_r \quad = \frac{k_m N \phi}{cR} \tag{5.34}$$

This equation demonstrates that the proposed system is capable of providing the damping effect which depends on the construction parameters of the algebraic screw and the rotary machine along with the value of resistance enforced by the controller.

## 5.5 Experimental Setup and Results

To evaluate performance of the proposed regenerative vibration damping system experimentally, the power electronic circuitry, discussed in Chapter 4, was utilized in the mass-spring test rig. The test rig was attached to a mechanical shaker as depicted in Figure 5.10. The mass-spring experimental setup consists of four parallel springs, an algebraic screw, and a rotary permanent-magnet machine (Maxon EC-max 40-283876) which isolates the mass from base excitations. The sprung mass was $5.53kg$. The stiffness of each spring was $1.6kN/m$, resulting in a total stiffness of $K_s = 6.4kN/m$.

The shaker can be excited with motion profiles containing different frequencies in the range $5 - 20$Hz. In the experiments, the shaker was set to oscillate at 5.6Hz which is close to the resonance frequency of the system. To find the resonance frequency of the system, the shaker was set to run with a sinusoidal signal with a linear sweep between 5Hz to 10Hz at a rate of 0.1 Hz/s as shown in Figure 5.11. Referring to this figure, the resonance frequency of the system was determined to be 5.474Hz. A displacement of 2.54mm peak-to-peak was set for the shaker, representing the maximum excitation that the system could handle at resonance without bottoming out. The phase to phase terminal inductances of the machine, $L_m = 1.6mH$, was utilized as the boost converter inductors $L_a$, $L_b$, and $L_c$ as shown in Figure 4.1. The three phases of the generator shown in Figure 5.1 were connected to the input of the power electronics interface. The phase-to-phase voltages along with the currents passing through the inductors were measured using LT1167 instrumentation amplifiers. These signals, along with the battery voltage were then captured by ADC

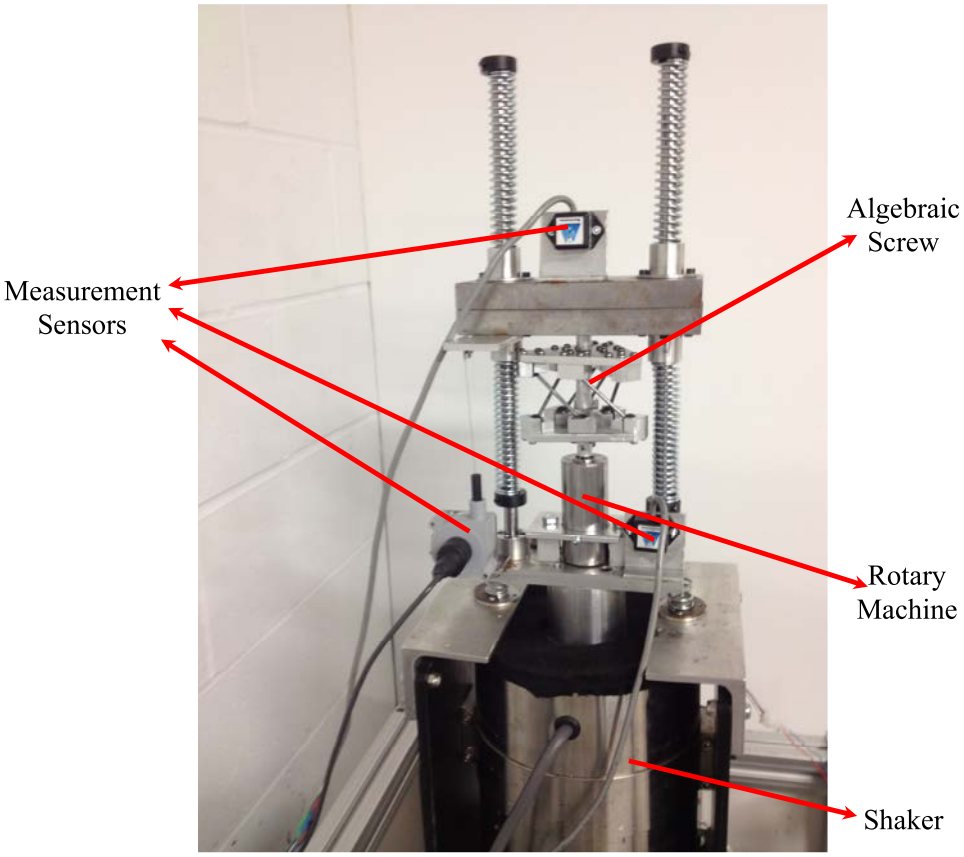


Figure 5.10: Mass-spring test rig connected to a mechanical shaker, algebraic screw, and rotary permanent-magnet synchronous machine.

channels of the dSPACE. The circuit phase-to-phase input resistance was then calculated at each sampling time by dividing the input voltage by the averaged inductor current in one PWM period ($0.001s$). A PWM frequency of 1 $kHz$ was utilized which is much higher than the frequency content of the input waveform. The value of $d$ was obtained from (4.36), (4.42), and (4.45), and applied to the converter at each sampling instant.

Figures 5.12, 5.13, and 5.14 illustrate performance of the controller for desired input resistances $10\Omega$ and $50\Omega$. Figure 5.13 reveals that when the desired resistance decreases from $50\Omega$ to $10\Omega$, more current is drawn from the stator coil, which decreases the vibration amplitude, i.e., more power is transferred to the battery in the form of electrical charge. Since the relative displacement decreases as illustrated in Figure 5.14, the amount of induced

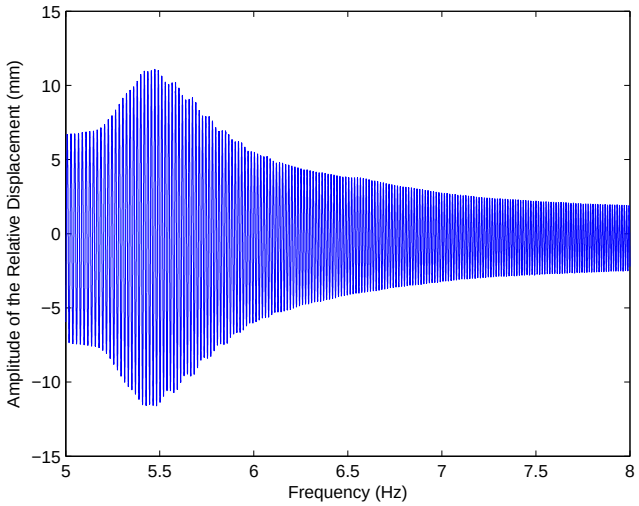


Figure 5.11: The amplitude of relative displacement for different frequencies.

voltage shown in Figure 5.12 also decreases. Form Figures 5.12 and 5.13, it is also evident that the controller could keep the ratio between the phase-to-phase voltages and current constant and equal to the desired electrical resistance (equivalent mechanical damping) by changing the duty cycle of the PWM control signal as shown in Figure 5.15. It should be noted that decreasing the desired input resistance corresponds to a larger duty cycle as indicated in (4.30), (4.31), and (4.32). Since all desired phase-to-phase input resistances of the three phases are set to be equal, they are controlled by only one PWM control signal. Therefore, some spikes in the value of duty cycle are observed at the times of changing the switching arrangement. Also, larger variations in the duty cycle for smaller desired resistances, can be verified by obtaining the sensitivity of input resistances in terms of the duty cycle $d$ in the same way discussed in Chapter 3.

It must be also noted that the algebraic screw cannot provide a unidirectional rotary motion. In fact, it rotates 30 degrees in one direction and turns back 70 degrees in other direction. Therefore, the generated three-phase voltages would depend on the relative orientation of the rotary machine and the algebraic screw. Figures 5.16 and 5.17 verifies this which can be improved by adding a gearhead mechanism between the algebraic screw and the rotary machine to provide a 360 degree rotation. Figures 5.18 and 5.19 demonstrate

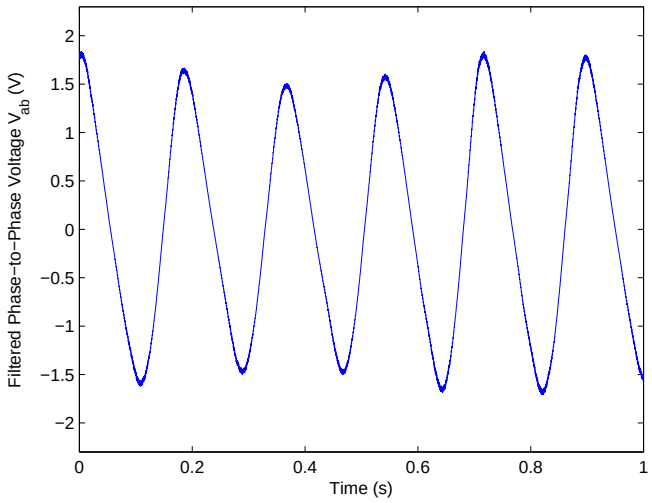


(a)

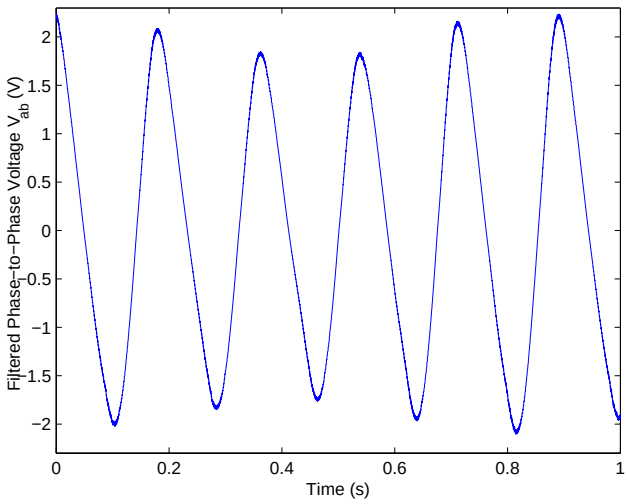


(b)

Figure 5.12: Experimental waveforms for phase-to-phase voltage $V_{ab}$ for different values of the desired resistance $R_{ab}$: (a) $R_{ab} = 10\Omega$, (b) $R_{ab} = 50\Omega$.

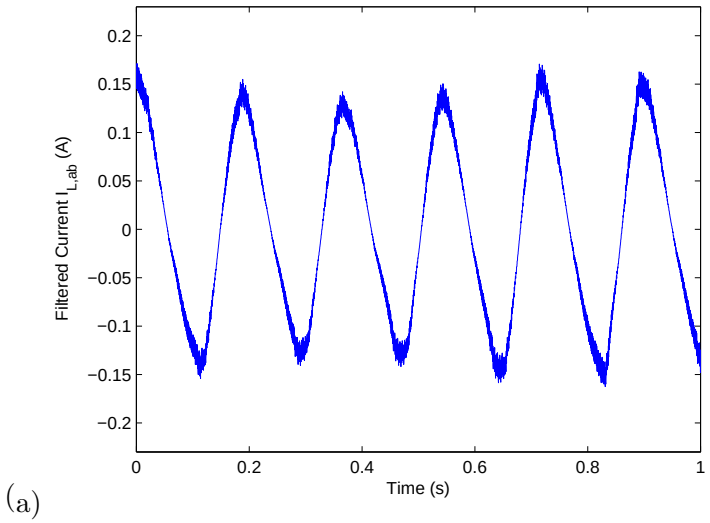


(a)

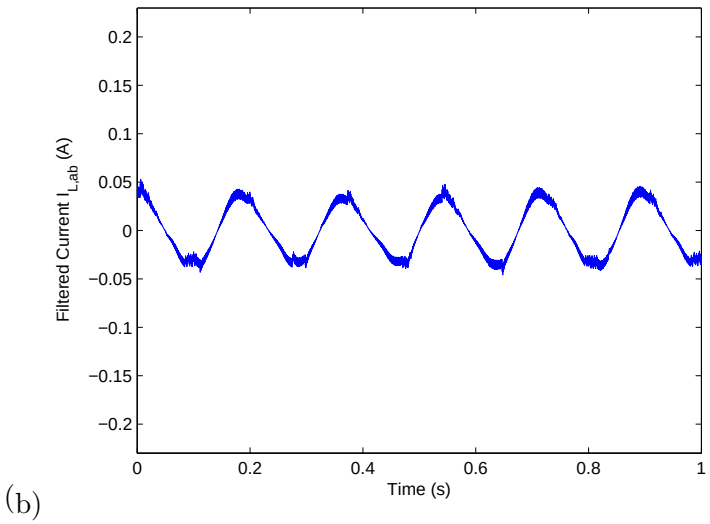


(b)

Figure 5.13: Experimental waveforms for current $I_{ab}$ for different values of the desired resistance $R_{ab}$: (a) $R_{ab} = 10\Omega$, (b) $R_{ab} = 50\Omega$.

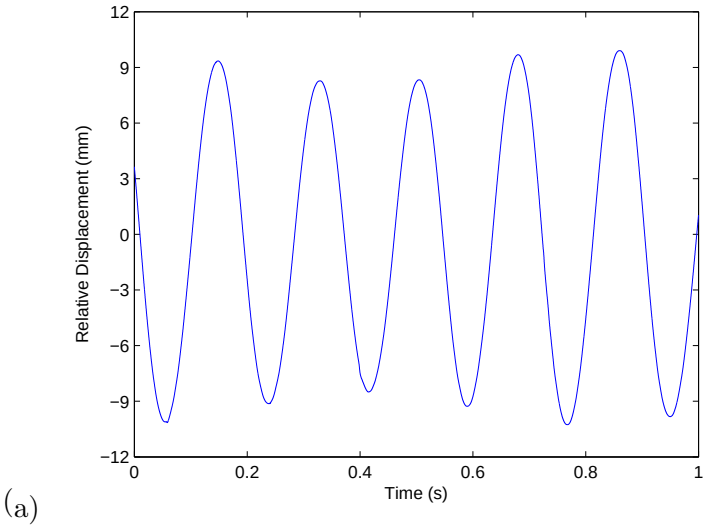


(a)

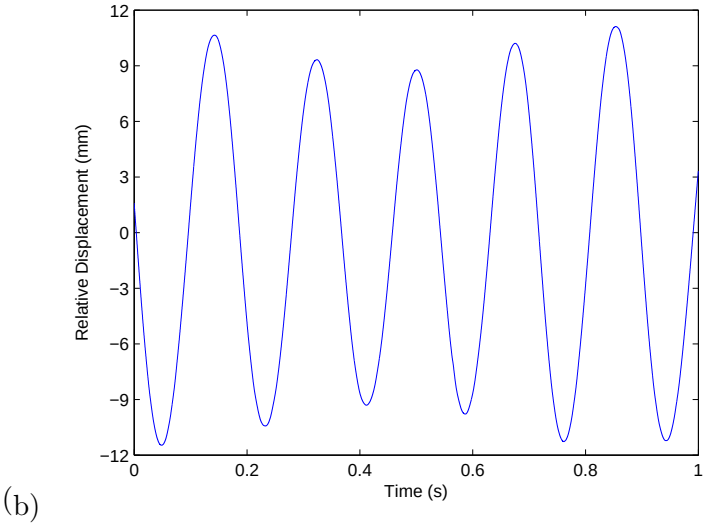


(b)

Figure 5.14: Experimental waveforms for relative displacement for different values of the desired resistance $R_{ab}$: (a) $R_{ab} = 10\Omega$, (b) $R_{ab} = 50\Omega$.

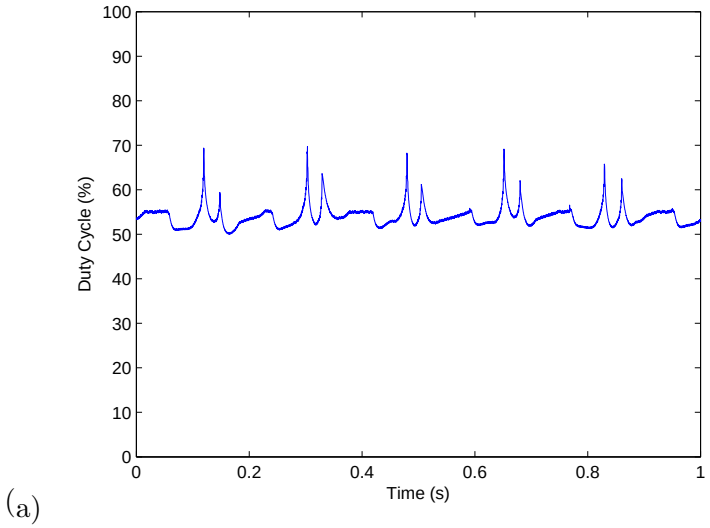


(a)

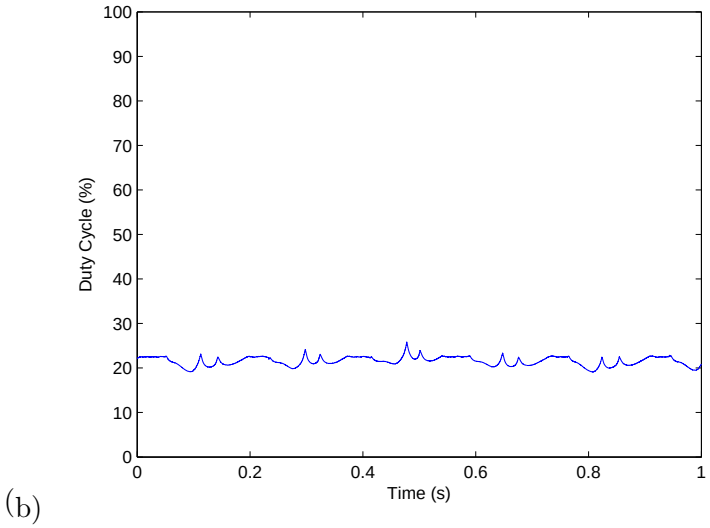


(b)

Figure 5.15: Experimental waveforms for the duty cycle of the PWM control signal for different values of the desired resistance $R_d = R_{ab} = R_{ac} = R_{bc}$: (a) $R_d = 10\Omega$, (b) $R_d = 50\Omega$.

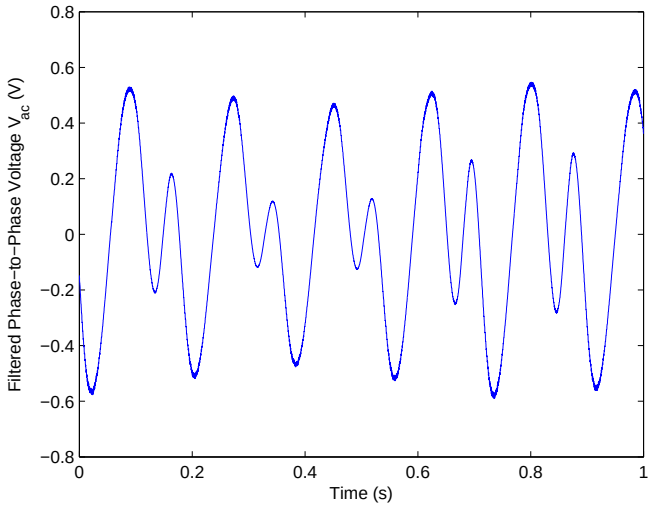


(a)

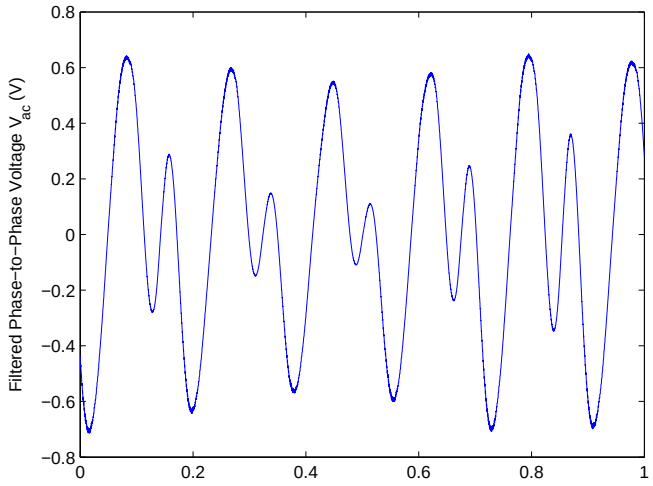


(b)

Figure 5.16: Experimental waveforms of the phase-to-phase voltage $V_{ac}$ for different values of the desired resistance $R_{ac}$: (a) $R_{ac} = 10\Omega$, (b) $R_{ac} = 50\Omega$.

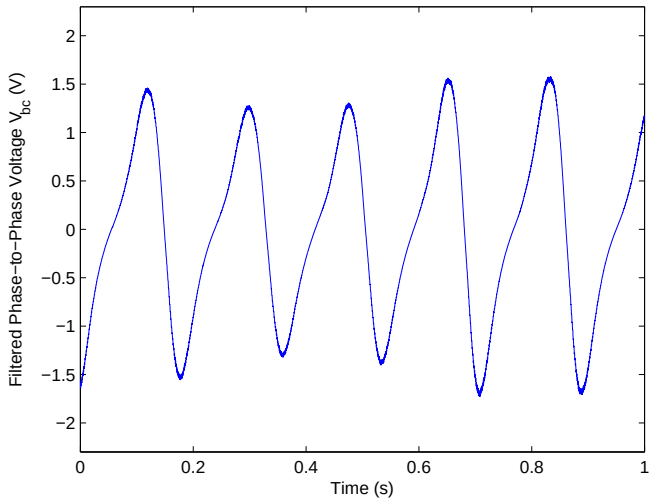


(a)

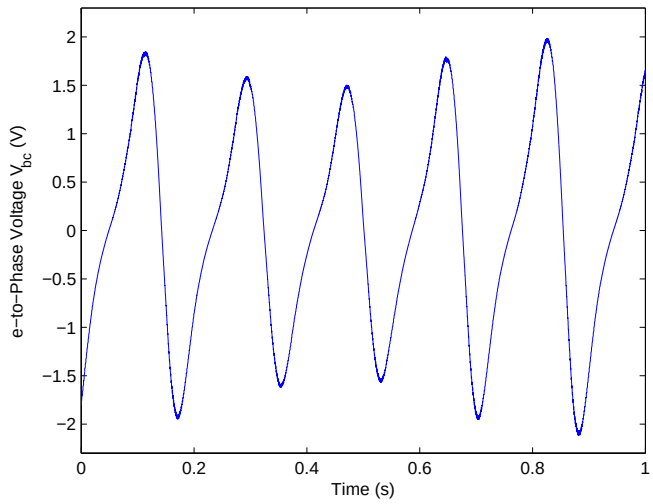


(b)

Figure 5.17: Experimental waveforms of the phase-to-phase voltage $V_{bc}$ for different values of the desired resistance $R_{bc}$: (a) $R_{bc} = 10\Omega$, (b) $R_{bc} = 50\Omega$.

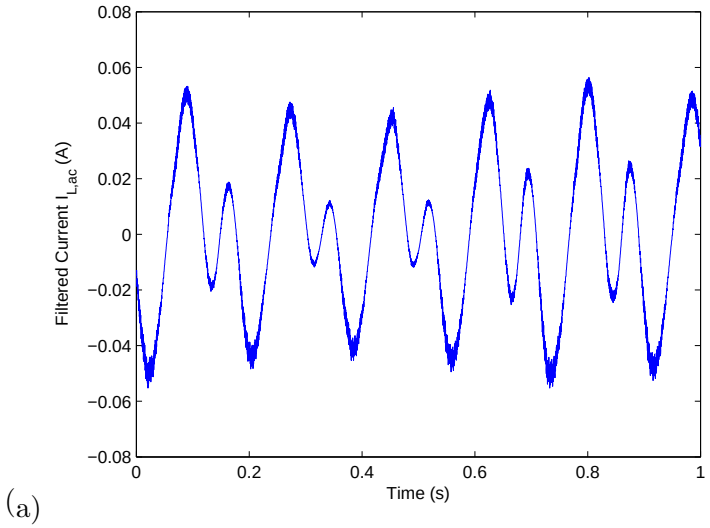


(a)

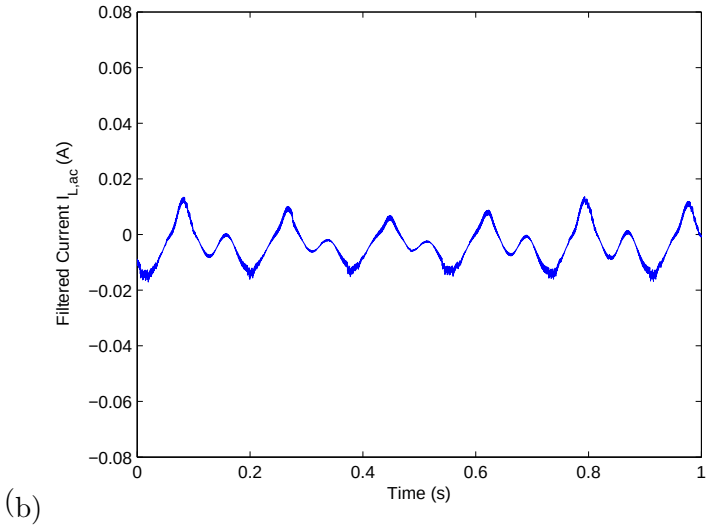


(b)

Figure 5.18: Experimental waveforms of the current $I_{ac}$ for different values of the desired resistance $R_{ac}$: (a) $R_{ac} = 10\Omega$, (b) $R_{ac} = 50\Omega$.

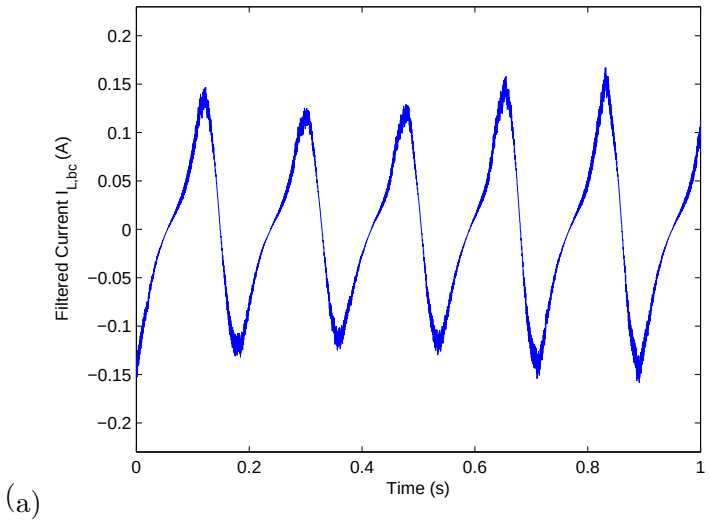


(a)

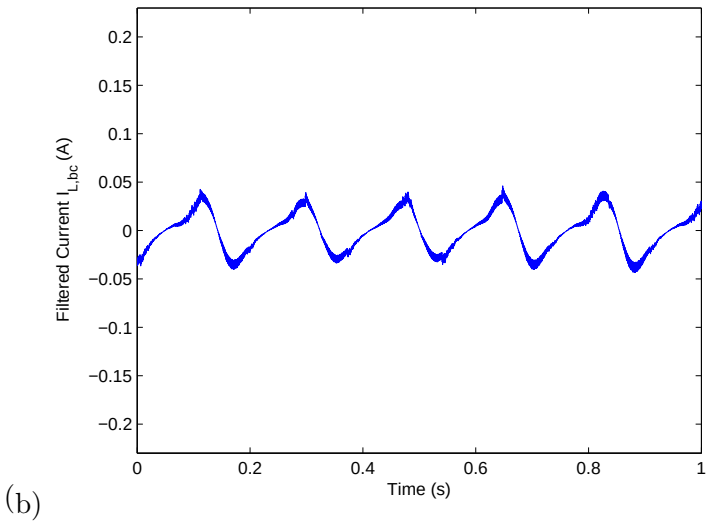


(b)

Figure 5.19: Experimental waveforms of the current $I_{bc}$ for different values of the desired resistance $R_{bc}$: (a) $R_{bc} = 10\Omega$, (b) $R_{bc} = 50\Omega$.

that the closed-loop system is capable of achieving the resistive behavior as the current waveforms follow the voltage waveforms with a constant ratio equal to the desired electrical resistance.

## 5.6 Summary and Conclusions

In this chapter, the boost-type converter along with the feedback control strategy developed in Chapter 4 were utilized in an energy-regenerative suspension system testbed. It was shown that the three-phase converter along with the controller and the rotary machine, coupled with an algebraic screw, can provide a rotary damping effect which depends on the construction parameters of the algebraic screw and the rotary machine as well as the value of the desired resistance enforced by the controller. The performance of the regenerative suspension system was then evaluated experimentally. The results demonstrate that the boost circuit and proposed feedback controller can successfully provide regenerative damping for mechanical vibrations.

# Chapter 6

# Summary, Conclusions, and Suggestions for Future Work

## 6.1 Summary and Conclusions

In this thesis, the idea of enforcing a pseudo-resistive behavior at the input of a boost converter was presented for single- and three-phase circuits. To this end, novel modeling and control schemes were developed and implemented for boost-type switching converters. It was shown that the above concept can be implemented by utilizing a model-based feedback controller that regulates the input resistance of the converter to desired values. The value of the converter's input resistance can be changed in real-time by changing the desired resistance applied as a set-point to the controller. The circuit and control scheme were then utilized in a regenerative vibration damper to provide the damping effect. The performance of the testbed suspension system consisting of four parallel springs and a tubular DC permanent-magnet machine was then evaluated through experimental studies. The results indicate that the boost circuit and proposed feedback controller can successfully provide regenerative damping for mechanical vibrations with high-efficiency power conversion. Motivated by the results obtained from the single-phase system in providing a pseudo-resistive input behavior, the idea was extended to a three-phase system. To this end, analytical expressions describing the input characteristic of the converter were obtained, based on which a feedback controller was designed. The three-phase converter system was then utilized in a suspension system testbed consisting of four parallel springs and a rotary permanent-magnet

machine connected to an algebraic screw. The system was used to evaluate the performance of the converter and control scheme in providing a desired damping effect.

## 6.2 Future Research

Based on the experience gained and results obtained in the course of this research, the following activities may be considered for future work.

### 6.2.1 Optimized Semi-Active Regenerative Suspension System

Developments in power electronics and permanent magnet materials justify the possibility of implementing electromagnetic machines to improve performance of automobile suspension systems. To this end, the three-phase converter along with the proposed controller and a permanent magnet brushless DC motor can be utilized in a regenerative suspension system that can harvest energy when subjected to a real road profile. In that case, the desired damping of the suspension system can be optimized by taking energy generation into account as well as the ride comfort and car handling. Therefore, the objective function may include all of these criteria. For example a root mean squared (RMS) objective function can be defined as follows

$$J = \sqrt{\int_0^T (x_w - x_r)^2 \, \mathrm{d}t} + \sqrt{\int_0^T W_{hs} * \ddot{x_b}^2 \, \mathrm{d}t} + \sqrt{\int_0^T P_{gen}^2 \, \mathrm{d}t} \tag{6.1}$$

where $W_{hs}$ is a weighting function for human sensitivity to vibrations, $*$ denotes convolution operation, $P_{gen}$ is the regenerated power, $x_w$, $x_r$, and $x_b$ represent vehicle's wheel displacement, road displacement, and vehicle's body displacement, respectively, as described in Chapter 3. The first term in (6.1) is aimed at improving the vehicle stability through attenuation of the tire pressure, or more precisely, through the attenuation of the unsprung mass force acting on the road. The second term in (6.1) provides passenger comfort, and the third term in (6.1) indicates the energy regenerative aspect. The first two terms have been already used for improvement of vehicle's performance [161]-[164], but adding energy regeneration to the optimization function is an interesting extension of the above works.

### 6.2.2 Bidirectional Single/Three Phase Boost Converter

The same concept can be extended to model, design, and control a signle/three phase boost converter by replacing the diodes, located in the upper part of the circuits shown in Sections 2.2 and 4.2, by MOSFET switches similar to the lower part of the circuits. Bidirectional boost PFC converters can supply prescribed amounts of reactive power (with leading or lagging current) independently of the DC load power, which allows the converter to be used as a static reactive power compensator in a power system. This can be also utilized as an active suspension system, where both damping and stiffness characteristics of the system can be controlled. The system virtually eliminates body roll and pitch variation in many driving situations including cornering, accelerating, and braking which allows car manufacturers to achieve a greater degree of ride quality and car handling by keeping the tires perpendicular to the road in corners, allowing better traction and control.

### 6.2.3 Extending the Controller for Continuous Conduction Mode (CCM)

As it was earlier verified in Sections 2.4 and 4.4, the efficiency drops when the duty cycle of PWM control signal reaches the DCM boundary. This is due to the fact that the circuit does not operate in the resistive region because of the inductive behavior of the circuit in CCM. To address this issue, control techniques should be designed and integrated with the proposed controller to provide the resistive behavior for all values of the duty cycle of PWM control signal for both DCM and CCM modes of operation.

### 6.2.4 Control System Implementation on an Embedded System Platform

The control strategy used in this research was simulated using SIMPOWER toolbox of MATLAB/Simulink, and then implemented on the rapid control prototyping hardware, dSPACE, using Real-Time workshop interface to evaluate theoretical and simulation results, experimentally. The operational scheme, control, and switching algorithm strategy developed in this dissertation can be ultimately implemented using low-cost embedded computing devices such as micro-controllers and field-programmable gate arrays (FPGAs) for a class of power electronic converters for vehicular suspension systems.

### 6.2.5 Battery Management

In this research, we did not study battery management circuitry and controllers. A battery management strategy is needed to extend the battery lifetime by controlling the charging rate and providing protection against overcharge. In fact, modern battery power management systems rely on a high-fidelity battery model to track the battery state of charge (SOC), predict runtime of each battery cell, and hence optimize the performance of whole battery system. Achieving this objective requires a battery model that accurately captures various nonlinear effects and dynamic electrical characteristics of the battery to facilitate system-level circuit design and simulation.

# Bibliography


[1] D.P. Arnold, "Review of microscale magnetic power generation," *IIEEE Transactions on Magnetics,* vol. 43, no. 11, pp. 3940-51, 2007.

[2] B. Dick, M. Fralick, H. Jazo, M. Kerber, J. Brewer, and R. Waters, "Optimization of kinetic energy harvester for low amplitude vibration," *IIEEE Sensors Conference,* pp. 1840-3, 2009.

[3] D. Zhu, S. Roberts, M.J. Tudor, and S.P. Beeby, "Design and experimental characterization of a tunable vibration-based electromagnetic micro-generator," *Sensors and Actuators A: Physical,* vol. 158, no. 2, pp. 284-93, 2010.

[4] S. P. Beeby, M.J. Tudor, and N.M. White, "Energy harvesting vibration sources for microsystems applications," *Measurement Science and Technology,* vol. 17, no. 12, pp. R175-R195, 2006.

[5] H. Polinder, B. Mecrow, A. Jack, P. Dickinson, and M.A. Mueller, "Linear generators for direct drive wave energy conversion," *IEEE. Transactions on Energy Conversion,* vol. 20, no. 2, pp. 260-7, 2005.

[6] R. Sabzehgar and M. Moallem, "A review of ocean wave energy conversion systems," *IEEE Electrical Power and Energy Conference,* pp. 1-6, 2009.

[7] M.A. Mueller, H. Polinder, and N. Baker, "Current and novel electrical generator technology for wave energy converters," *IEEE International Electric Machines and Drives Conference,* vol. 2, pp. 1401-6, 2007.

[8] M.A Mueller and N.J. Baker, "Direct drive wave energy converters," *Journal of Power and Energy,* vol. 219, no. A3, pp. 223-34, 2005.

[9] S.-Y. Jung, H. Jung, S.-C. Hahn, H.-K. Jung, and C.-G. Lee, "Optimal design of direct-driven PM wind generator for maximum annual energy production," *IEEE Transactions on Magnetics,* vol. 44, no. 6, pp. 1062-5, 2008.

[10] H. Polinder, F.F.A.van der Pijl, G.-J. de Vilder, and P.J. Tavner, "Comparison of direct-drive and geared generator concepts for wind turbines," *IEEE Transactions on Energy Conversion,* vol. 21, no. 3, pp. 725-33, 2006.

[11] S. Liu, H. Wei, and W. Wang, "Investigation on some key issues of regenerative damper with rotary motor for automobile suspension," *IEEE International Conference on Electronic and Mechanical Engineering and Information Technology,* vol. 3, pp. 1435-9, 2011.

[12] Y. Kawamoto and Y. Suda, "Modeling of electromagnetic damper for automobile suspension," *Journal of System Design and Dynamics,* vol. 1, no. 3, pp. 524-35, 2007.

[13] Y. Zhang, K. Huang, F. Yu, Y. Gu, and D. Li, "Experimental verification of energy-regenerative feasibility for an automotive electrical suspension system," *IEEE International Conference on Vehicular Electronics and Safety,* pp. 1-5, 2007.

[14] A. Phipps, D. Phung, M. Kerber, B. Dick, A. Powers, and R. Waters, "Development of kinetic energy harvesting systems for vehicle applications," *IEEE Sensors Conference,* pp. 24-7, 2011.

[15] M.-J. Yang, H.-L. Jhou, B.-Y. Ma, and K.-K. Shyu, "A cost-effective method of electric brake with energy regeneration for electric vehicles," *IEEE Transactions on Industrial Electronics,* vol. 56, no. 6, pp. 2203-10, 2009.

[16] M. Ye, Z. Bai, and B. Cao, "Robust control for regenerative braking of battery electric vehicle," *IET Control Theory and Applications,* vol. 2, no. 12, pp. 1105-14, 2008.

[17] R. Sabzehgar and S.Arzanpour, "Energy harvesting from bike using linear DC motor," *ASME International Mechanical Engineering Congress and Exposition,* pp. 291-6, 2010.

[18] K. Nakano, Y. Suda, and S. Nakadai, "Self-powered active vibration control using a single electric actuator," *Journal of Sound and Vibration,* vol. 260, no. 2, pp. 213-35, 2003.

[19] C.S.S. Sarma, "Energy harvesting and intelligent load sharing for electric hybrid vehicles: A system perspective," *IEEE India Conference,* pp. 1-5, 2011.

[20] M.H. Nehrir, C. Wang, K. Strunz, H. Aki, R. Ramakumar, J. Bing, Z. Miao, and Z. Salameh, "A review of hybrid renewable/alternative energy systems for electric power generation: configurations, control, and applications," *IEEE Transactions on Sustainable Energy,* vol. 2, no. 4, pp. 392-403, 2011.

[21] N. Mohan, T.M. Undeland, and W.P. Robbins, "Power electronics," *Wiley New York,* 1995.

[22] T. Key and J.-S. Lai, "Analysis of harmonic mitigation methods for building wiring systems," *IEEE Transactions on Power Systems,* vol. 13, pp. 890-7, 1998.

[23] K. P. Louganski and J.-S. Lai, "Input filter design for power factor correction circuits," *IEEE Transactions on Power Electronics,* vol. 11, pp. 119-205, 1996.

[24] D.F. Pires, V.F. Pires, C.H. Antunes, and A.G. Martins, "Passive and active anti-resonance capacitor sSystems for power factor correction," *IEEE International Power Electronics and Motion Control Conference,* pp. 1460-5, 2006.

[25] D. Detjen, J. Jacobs, R.W. De Doncker, and H.-G. Mall, "A new hybrid filter to dampen resonances and compensate harmonic currents in industrial power systems with power factor correction equipment," *IEEE Transactions on Power Electronics,* vol. 16, no. 6, pp. 821-7, 2001.

[26] S.N.A.L. Yousif, M.Z.C. Wanik, and A. Mohamed, "Implementation of different passive filter designs for harmonic mitigation," *IEEE Power and Energy Conference,* pp. 229-34, 2004.

[27] W.M. Lin, M.M. Hernando, A. Fernandez, J. Sebastian, and P.J. Villegas, "A new topology for passive PFC circuit design to allow AC-to-DC converters to comply with the new version of IEC1000-3-2 regulations," *IEEE 33th Annual Power Electronics Specialists Conference,* pp. 2050-5, 2002.

[28] S. Rahmani, A. Hamadi, and K. Al-Haddad, "A new three phase hybrid passive filter to dampen resonances and compensate harmonics and reactive power for any

type of load under distorted source conditions," *IEEE Power Electronics Specialists Conference,* pp. 2594-9, 2007.

[29] Y. Nishida and H. Oyama, "Passive PFC converter for energy saving-efficient and cheap diode rectifier topology," *IEEE 8th International Conference on Power Electronics and ECCE Asia,* pp. 1073-6, 2011.

[30] A. Sandali, P. Sicard, and A. Cheriti, "Power factor improvement of an AC/AC converter by association of PDM control and passive filtering," *IEEE 33rd Annual Power Electronics Specialists Conference,* pp. 250-5, 2002.

[31] A.I. Pressman, K. Billings, and T. Morey, "Switching power supply design," *McGraw-Hill Professional,* 2009.

[32] S.-K. Ki, D.K.-W. Cheng, and D.D.-C. Lu, "Analysis and design of a single-phase hybrid mode power factor correction converter," *IET Power Electronics,* vol. 1, no. 1, pp. 72-83, 2008.

[33] B. Singh, B.N. Singh, A. Chandra, K. Al-Haddad, A. Pandey, and D.P. Kothari, "A review of single-phase improved power quality AC-DC converters," *IEEE Transactions on Industrial Electronics,* vol. 50, no. 5, pp. 962-81, 2003.

[34] G. Moschopoulos and P. Jain, "Single-phase single-stage power-factor-corrected converter topologies," *IEEE Transactions on Industrial Electronics,* vol. 52, no. 1, pp. 23-35, 2005.

[35] J.P.M. Figueiredo, F.L. Tofoli, and B.L.A. Silva, "A review of single-phase PFC topologies based on the boost converter," *9th IEEE/IAS International Conference on Industry Applications,* pp. 1-6, 2010.

[36] K. Raggl, T. Nussbaumer, G. Doerig, J. Biela, and J.W. Kolar, "Comprehensive design and optimization of a high-power-density single-phase boost PFC," *IEEE Transactions on Industrial Electronics,* vol. 56, no. 7, pp. 2574-87, 2009.

[37] K. Yao, X. Ruan, X. Mao, and Z. Ye, "Variable-duty-cycle control to achieve high input power factor for DCM boost PFC converter," *IEEE Transactions on Industrial Electronics,* vol. 58, no. 5, pp. 1856-65, 2011.

[38] J. Galvez and M. Ordonez, "High performance boundary control of boost-derived PFCs: natural switching surface derivation and properties," *IEEE Transactions on Power Electronics,* vol. 27, no. 8, pp. 3807-16, 2012.

[39] Y. Jang and M.M. Jovanovic, "Isolated boost converters," *IEEE Transactions on Power Electronics,* vol. 22, pp. 1514-21, 2007.

[40] M. Nymand and M.A.E. Andersen, "High-efficiency isolated boost dc-dc converter for high-power low-voltage fuel-cell applications," *IEEE Transactions on Industrial Electronics,* vol. 57, pp. 505-14, 2010.

[41] K.P. Louganski and J.S. Lai, "Current phase lead compensation in single-phase PFC boost converters with a reduced switching frequency to line frequency ratio," *IEEE Transactions on Power Electronics,* vol. 22, no. 1, pp. 113-9, 2007.

[42] J.P.R. Balestero, F.L. Tofoli, R.C. Fernandes, G.V. Torrico-Bascope, and F.J.M. de Seixas, "Power factor correction boost converter based on the three-state switching cell," *IEEE Transactions on Industrial Electronics,* vol. 59, no. 3, pp. 1565-77, 2012.

[43] C.K. Tse and M.H.L Chow, "Theoretical study of switching power converters with power factor correction and output regulation," *IEEE Transactions on Circuits and Systems-I: Fundamental Theory and Applications,* vol. 47, pp. 1047-55, 2000.

[44] C.K. Tse, "Circuit theory of power factor correction in switching converters," *International Journal of Circuit Theory and Applications,* 2003, 31, (1), pp. 157-98.

[45] K. Matsui, I. Yamamoto, T. Kishi, M. Hasegawa, H. Mori, and F. Ueda, "A comparison of various buck-boost converters and their application to PFC," *28th Annual Conference of the Industrial Electronics Society, IECON '02,* vol. 1, pp. 30-36, 2002.

[46] J.-C. Crebier, B. Revol, and J.P. Ferrieux, "Boost-chopper-derived PFC rectifiers: interest and reality," *IEEE Transactions on Industrial Electronics,* vol. 52, no. 1, pp. 36-45, 2005.

[47] W.-Y. Choi, J.-M. Kwon, E.-H. Kim, J.-J. Lee, and B.-H. Kwon, "Bridgeless boost rectifier with low conduction losses and reduced diode reverse-recovery problems," *IEEE Transactions on Industrial Electronics,* vol. 54, no. 2, pp. 769-80, 2007.

[48] Q. Zhao, F. Tao, F.C. Lee, P. Xu, and J. Wei, "A simple and effective method to alleviate the rectifier reverse-recovery problem in continuous-current-mode boost converters," *IEEE Transactions on Power Electronics,* vol. 16, pp. 649-58, 2001.

[49] D.D.-C. Lu, D.K.-W. Cheng, and Y.-S. Lee, "A single-switch continuous-conduction-mode boost converter with reduced reverse-recovery and switching losses," *IEEE Transactions on Industrial Electronics,* vol. 50, pp. 767-76, 2003.

[50] J.M. Kwon, W.Y. Choi, and B.H. Kwon, "Cost-effective boost converter with reverse-recovery reduction and power factor correction," *IEEE Transactions on Industrial Electronics,* vol. 55, no. 1, pp. 471-3, 2008.

[51] J. Wang, W.G. Dunford, and K. Mauch, "A comparison of modified boost converters with continuous inductor current mode and ripple free input current with conventional converters," *IEEE Industry Applications Conference,* vol. 2, pp. 878-885, 1996.

[52] R. Martinez and P.N. Enjeti, "A high-performance single-phase rectifier with input power factor correction," *IEEE Transactions on Power Electronics,* vol. 11, no. 2, pp. 311-7, 1996.

[53] J.W. Lim and B.H. Kwon, "A power factor controller for single-phase PWM rectifiers," *IEEE Transactions on Industrial Electronics,* vol. 46, no. 5, pp. 1035-7, 1999.

[54] Y. Jang and M.M. Jovanovic, "Interleaved boost converter with intrinsic voltage-doubler characteristic for universal-line PFC front end," *IEEE Transactions on Power Electronics,* vol. 22, no. 4, pp. 1394-1401, 2007.

[55] B.A. Miwa, D.M. Otten, and M.E. Schlecht, "High efficiency power factor correction using interleaving techniques," *IEEE Applied Power Electronics Conference and Exposition,* pp. 557-68, 1992.

[56] D. Garinto, "Interleaved boost converter system for unity power factor operation," *IEEE European Conference on Power Electronics and Applications,* pp. 1-7, 2007.

[57] M. Pahlevaninezhad, P. Das, J. Drobnik, P.K. Jain, and A. Bakhshai, "A ZVS interleaved boost AC/DC converter used in plug-in electric vehicles," *IEEE Transactions on Power Electronics,* vol. 27, no. 8, pp. 3513-29, 2012.

[58] C.A. Gallo, F.L. Tofoli, and J.A.C. Pinto, "A passive lossless snubber applied to the ac-dc interleaved boost converter," *IEEE Transactions on Power Electronics,* vol. 25, no. 3, pp.775-85, 2010.

[59] R. Srinivasan and R. Oruganti, "A unity power factor converter using half bridge boost topology," *IEEE Transactions on Power Electronics,* vol. 13, no. 3, pp. 487-500, 1998.

[60] D.K. Jackson and S.B. Leeb, "A power factor corrector with bidirectional power transfer capability," *IEEE Power Electronics Specialists Conference,* vol. 1, pp. 365-70, 2000.

[61] M.T. Zhang, Y. Jiang, F.C. Lee, and M.M. Jovanovic, "Single-phase three-level boost power factor correction converters," *IEEE Applied Power Electronics Conference and Exposition,* vol. 1, pp. 434-9, 1995.

[62] J.C. Salmon, T. Tang, and E. Nowicki, "Operation, control and performance of a family of high power unity power factor rectifiers," *IEEE Canadian Conference on Electrical and Computer Engineering,* vol. 2, pp. 854-7, 1995.

[63] G.V.T. Bascop and I. Barbi, "Generation of a family of non-isolated DC-DC PWM converters using new three-state swiching cell," *IEEE Power Electronics Specialists Conference,* vol. 2, pp. 858-63, 2000.

[64] G.V.T. Bascop and I. Barbi, "A single phase PFC 3 kW converter using a three-state switching cell," *IEEE Power Electronics Specialists Conference,* vol. 5, pp. 4037-42, 2004.

[65] R.A. da Camara, R.N.A.L. Silva, G.A.L. Henn, P.P. Praa, C.M.T. Cruz, and R.P.T. Bascop, "Voltage doubler boost rectifier based on three-state switching cell for UPS applications," *IEEE Brazilian Power Electronics Conference,* vol. 5, pp. 458-63, 2009.

[66] T. N. Santelo, J.P.R. Balestero, F.J.M. Seixas, and G.V.T. Bascop, "Three-state switching cell for single-stage PFC rectifier," *Global Congress on Engineering and Technology Education,* pp. 1521-5, 2005.

[67] P. Kong, S. Wang, and F.C. Lee, "Common mode EMI noise suppression for bridgeless PFC converters," *IEEE Transactions on Power Electronics,* vol. 23, no. 1, pp. 291-7, 2008.

[68] Y. Jang and M.M. Jovanovic, "A bridgeless PFC boost rectifier with optimized magnetic utilization," *IEEE Transactions on Power Electronics,* vol. 24, no. 1, pp. 85-93, 2009.

[69] L. Huber, Y. Jang, and M. M. Jovanovic, "Performance evaluation of bridgeless PFC boost rectifiers," *IEEE Transactions on Power Electronics,* vol. 23, no. 3, pp. 1381-90, 2008.

[70] K.D. Gusseme, D.M. Van de Sype, A.P.M. Van den Bossche, and J.A. Melkebeek, "Digitally controlled boost power-factor-correction converters operating in both continuous and discontinuous conduction mode," *IEEE Transactions on Industrial Electronics,* vol. 52, no. 1, pp. 88-97, 2005.

[71] H. Ma, Y. Ji, and Y. Xu, "Design and analysis of single-stage power factor correction converter with a feedback winding," *IEEE Transactions on Power Electronics,* vol. 25, no. 6, pp. 1460-70, 2010.

[72] Y.-K. Lo, H.-J. Chiu, T.-P. Lee, I. Purnama, and J.-M.Wang, "Analysis and design of a photovoltaic system DC connected to the utility with a power factor corrector," *IEEE Transactions on Industrial Electronics,* vol. 56, no. 11, pp. 4354-62, 2009.

[73] M. Mahdavi and H. Farzanehfard, "Zero-current-transition bridgeless PFC without extra voltage and current stress," *IEEE Transactions on Industrial Electronics,* vol. 56, no. 7, pp. 2540-7, 2009.

[74] N. Vazquez, J. Lopez, J. Arau, C. Hernandez, and E. Rodriguez, "A different approach to implement an active input current shaper," *IEEE Transactions on Industrial Electronics,* vol. 52, no. 1, pp. 132-8, 2005.

[75] Y.M. Liu and L.K. Chang, "Single-stage soft-switching ac−dc converter with input-current shaping for universal line," *IEEE Transactions on Industrial Electronics,* vol. 56, pp. 467-79, 2009.

[76] R.K. Tripathi, S.P. Das, and G.K. Dubey, "Mixed-mode operation of boost switch-mode rectifier for wide range of load variations," *IEEE Transactions on Power Electronics,* vol. 17, no. 6, pp. 999-1009, 2002.

[77] Z. Lai and K. M. Smedley, "A family of continuous-conduction-mode power-factor-correction controllers based on the general pulse-width modulator," *IEEE Transactions on Power Electronics,* vol. 13, no. 3, pp. 501-10, 1998.

[78] R.W. Erickson and D. Maksimovic, *Fundamentals of Power Electronics*, Second Edition, Kluwer Academic Publishers, 2001.

[79] H.S. Athab, "A duty cycle control technique for elimination of line current harmonics in single-state DCM boost PFC circuit," *IEEE TENCON,* pp. 1-6, 2008.

[80] T. Nussbaumer, K. Raggl, and J. W. Kolar, "Design guidelines for interleaved single-phase boost PFC circuits," *IEEE Transactions on Industrial Electronics,* vol. 56, no. 7, pp. 2559-73, 2009.

[81] D. Weng and S. Yuvarajian, "Constant switching frequency acdc converter using second harmonic injected PWM," *IEEE Transactions on Power Electronics,* vol. 11, no. 1, pp. 115-21, 1996.

[82] Y.-K. Lo, J.-Y. Lin, and S.-Y. Ou, "Switching frequency control for regulated discontinuous conduction mode boost rectifiers," *IEEE Transactions on Industrial Electronics,* vol. 54, no. 2, pp. 760-8, 2007.

[83] C. Zhou, R.B. Ridley, and F.C. Lee, "Design and analysis of a hysteretic boost power factor correction circuit," *IEEE Power Electronics Specialists Conference,* pp. 800-7, 1990.

[84] J. Sun, D.M. Mitchell, M.F. Greuel, P.T. Krein, and R.M. Bass, "Averaged modeling of PWM converters operating in discontinuous conduction mode," *IEEE Transactions on Power Electronics,* vol. 16, no. 4, pp. 482-92, 2001.

[85] H. Y. Kanaan and , K. Al-Haddad, "Modeling techniques applied to switch-mode power converters: application to the boost-type single-phase full-bridge rectifier," *IEEE Conference on Human System Interactions,* pp. 979-83, 2008.

[86] G.W. Wester and R.D. Middlebrook, "IEEE Transactions on Aerospace and Electronic Systems," *IEEE Power Processing and Electronics Specialists Conference,* vol. AES-9, no. 3, pp. 376-85, 1973.

[87] A. Emadi, "Modeling and analysis of multiconverter DC power electronic systems using the generalized state-space averaging method," *IEEE Transactions on Industrial Electronics,* vol. 51, no. 3, pp. 661-8, 2004.

[88] A. Yazdani and R. Iravani, "A generalized state-space averaged model of the three-level NPC converter for systematic DC-voltage-balancer and current-controller design," *IEEE Transactions on Power Delivery,* vol. 20, no. 2, pp. 1105-14, 2005.

[89] M.F.N. Tajuddin, N.A. Rahim, I. Daut, B. Ismail, and M.F. Mohammed, "State space averaging technique of power converter with digital PID controller," *IEEE TENCON,* pp. 1-6, 2009.

[90] A. Davoudi, J. Jatskevich, P.L. Chapman, and A. Khaligh, "Averaged-switch modeling of fourth-order PWM DCDC converters considering conduction losses in discontinuous mode," *IEEE Transactions on Power Electronics,* vol. 22, no. 6, pp. 2410-5, 2007.

[91] M. Carpaneto, G. Ferrando, M. Marchesoni, and C. Vacca, "The average switch model of a new double-input DC/DC boost converter for hybrid fuel-cell vehicles," *IEEE International Symposium on Industrial Electronics,* vol. 2, pp. 601-7, 2005.

[92] J. Stahl, A. Bucher, C. Oeder, and T. Duerbaum, "Sampled-data modeling applied to output impedance reveals missing term in state-space averaging model," *IEEE 12th Workshop on Control and Modeling for Power Electronics,* pp. 1-8, 2010.

[93] C.-C. Fang, "Sampled-data modeling and analysis of one-cycle control and charge control," *IEEE Transactions on Power Electronics,* vol. 16, no. 3, pp. 345-50, 2001.

[94] A.J. Forsyth and G. Calderon-Lopez, "Sampled-data analysis of the dual-interleaved boost converter With interphase transformer," *IEEE Transactions on Power Electronics,* vol. 27, no. 3, pp. 1338-46, 2012.

[95] S. Singer and R. Erickson, "Canonical modeling of power processing circuits based on the POPI concept," *IEEE Transactions on Power Electronics,* vol. 7, no. 1, pp. 37-43, 1992.

[96] S. Singer, "Realization of Loss-Free Resistive Elements," *IEEE Transactions on Circuits and Systems,* vol. 37, no. 1, pp. 54-60, 1990.

[97] A. Wang, H. Yin, and S. Wang, "Realization of source with internal loss-free resistive characteristic," *IEEE Transactions on Circuits and Systems I: Fundamental Theory and Applications,* vol. 48, no. 7, pp. 830-9, 2001.

[98] H.Y. Kanaan and K. Al-Haddad, "A comparison between three modeling approaches for computer implementation of high-fixedswitching-frequency power converters operating in a continuous mode," *IEEE Canadian Conference on Electrical and Computer Engineering,* vol. 1, pp. 274-9, 2002.

[99] R. Sabzehgar and M. Moallem, "Modeling and control of a boost converter for seudo-resistive input behavior," *IET International Conference on Renewable Power Generation,* pp. 1-5, 2011.

[100] R. Sabzehgar and M. Moallem, "Modeling and control of a boost converter for irregular input sources," *IET Journal on Power Electronics,* in press, 2012.

[101] R. Sabzehgar and M. Moallem, "Regenerative vibration damping of a suspension system testbed," *IEEE International Symposium on Industrial Electronics,* pp. 1-5, 2012.

[102] R. Sabzehgar and M. Moallem, "A boost-type power converter for energy regenerative damping," *IEEE/ASME Transaction on Mechatronics,* in press, 2012.

[103] R. Sabzehgar and M. Moallem, "Modeling and control of a three-phase boost converter for Irregular Input sources," *IEEE International Conference on Industrial Electronics,* accepted, 2012.

[104] R. Sabzehgar and M. Moallem, "Modeling and control of a three-phase boost converter for resistive input behavior," *IEEE Transaction on Industrial Electronics,* revised version submitted, 2012.

[105] R. Sabzehgar and M. Moallem, "Modeling and control of a three-phase boost converter for resistive input behavior," *United States Provisional Patent,* Application no. 61/607373, 2012.

[106] F. Musavi, W. Eberle, and W.G.L. Dunford, "A high-performance single-phase bridgeless interleaved PFC converter for plug-in hybrid electric vehicle battery chargers," *IEEE Transactions on Industry Applications,* vol. 47, no. 4, pp. 1833-43, 2011.

[107] E. Firmansyah, S. Abe, M. Shoyama, S. Tomioka, and T. Ninomiya, "A critical-conduction-mode bridgeless interleaved boost power factor correction: Its control scheme based on commonly available controller," *IEEE International Conference on Power Electronics and Drive Systems,* pp. 109-14, 2009.

[108] W.-Y. Choi and J.-S. Yoo, "A Bridgeless Single-Stage Half-Bridge AC/DC Converter," *IEEE Transactions on Power Electronics,* vol. 26, no. 12, pp. 3884-95, 2011.

[109] International Rectifier, *Automotive Power MOSFET IRFP2907 Datasheet,* http://www.irf.com/product-info/datasheets/data/irfp2907.pdf.

[110] Vishay High Power Products, *Schottky Rectifier MBR4060WT Datasheet,* http://www.vishay.com/docs/94296/mbr4060w.pdf.

[111] dSPACE Inc., USA, *DS1103 PPC Controller Board,* http://www.dspace.com/en/inc/home/products/hw/singbord/ppcconbo.cfm.

[112] G.R. Wendel and G.L. Stecklein, "A regenerative active suspension system," *ASME International Congress and Exposition,* pp. 129-35, 1991.

[113] M.G. Fodor and R.C. Redfield, "The variable linear transmission for regenerative damping in vehicle suspension control," *Journal of Vehicle System Dynamics,* vol. 22, 1993.

[114] Y. Suda, T. Shiiba, "New hybrid suspension system with active control and energy regeneration," *Journal of Vehicle System Dynamics,* vol. 25, pp. 641-54, 1996.

[115] M.R. Jolly and D.L. Margolis, "Regenerative systems for vibration control," *ASME Journal of Vibration and Acoustics,* vol. 119, pp. 208-15, 1997.

[116] Y. Okada and H. Harada, "Regenerative control of active vibration damper and suspension systems," *Proceedings of the 35th IEEE Decision and Control,* vol. 4, pp. 4715-20, 1996.

[117] K. Nakano and Y. Suda, "Combined type self-powered active vibration control of truck cabins," *Journal of Vehicle System Dynamics,* vol. 41, no. 6, pp. 449-73, 2004.

[118] Y. Zhang, K. Huang, F. Yu, Y. Gu, and D. Li, "Experimental verification of energy-regenerative feasibility for an automotive electrical suspension system," *IEEE International Conference on Vehicular Electronics and Safety,* pp. 1-5, 2007.

[119] A. Stribrsky, K. Hyniova, J. Honcu, and A. Kruczek, "Energy recuperation in automotive active suspension systems with linear electric motor," *Mediterranean Conference on Control and Automation,* pp. 1-5, 2007.

[120] X. Lin, G. Xuexun, "Hydraulic transmission electromagnetic energy-regenerative active suspension and its working principle," *2nd International Workshop on Intelligent Systems and Applications (ISA),* pp. 1-5, 2010.

[121] I. Martins, J. Esteves, G. D. Marques, and F. P. d. Silva, "Permanent-magnets linear actuator applicability in automobile active suspensions," *IEEE Transactions on vehicular technology,* vol. 55, pp. 86-94, 2006.

[122] A. Kim and Y. Okada, "Variable resistance type energy regenerative damper using pulse width modelated step-up chopper," *ASME Journal of Vibration and Acoustics,* vol. 124, pp. 110-5, 2002.

[123] M. Galea, C. Gerada, T. Raminosoa, and P. Wheeler, "Design of a high force density tubular permanent magnet motor," *IEEE Int. Conf. on Electrical Machines,* 6 pages, 2010.

[124] K. Rhinefranka, E.B. Agamloha, A. von Jouannea, A.K. Wallacea, J. Prudella, K. Kimblea, J. Aillsa, E. Schmidta, P. Chanb, B. Sweenyb and A. Schachera, "Novel ocean energy permanent magnet linear generator buoy," *Elsevier International Journal of Renewable Energy,* vol. 31, no. 9, pp. 1279-98, 2006.

[125] LinMot USA, *Industrial Linear Motors Datasheet,* Edition 15.

[126] L. Zuo, J.-J.E. Slotine, and S. A. Nayfeh, "Model reaching adaptive control for vibration isolation," *IEEE Transactions on Control Systems Technology,* vol. 13, no. 4, pp. 611-7, 2005.

[127] L.H. Nguyen, S. Park, A. Turnip, and K.-S. Hong, "Modified skyhook control of a suspension system with hydraulic strut mount," *IEEE ICROS-SICE International Joint Conference,* pp. 1347-52, 2009.

[128] B. Singh, B.N. Singh, A. Chandra, K. Al-Haddad, A. Pandey, and D.P. Kothari, "A review of three-phase improved power quality AC-DC converters," *IEEE Transactions on Industrial Electronics,* vol. 51, no. 3, pp. 641-60, 2004.

[129] T. Nussbaumer and J. W. Kolar, "Improving mains current quality for three-phase three-switch buck-type PWM rectifiers," *IEEE Transactions on Power Electronics,* vol. 21, no. 4, pp. 967-73, 2006.

[130] T. Nussbaumer, M. Baumann, and J. W. Kolar, "Comprehensive design of a three-phase three-switch buck-type PWM rectifier," *IEEE Transactions on Power Electronics,* vol. 22, no. 2, pp. 551-9, 2007.

[131] V. F. Pires and J. F. Silva, "Three-phase single-stage four-switch PFC buck-boost-type rectifier," *IEEE Transactions on Industrial Electronics,* vol. 52, no. 2, pp. 444-53, 2005.

[132] G. Gong, M. L. Heldwein, U. Drofenik, J. Minibock, K. Mino, and J. W. Kolar, "Comparative evaluation of three-phase high-power-factor AC-DC converter concepts for application in future more electric aircraft," *IEEE Transactions on Industrial Electronics,* vol. 52, no. 3, pp. 727-37, 2005.

[133] R. Garcia-Gil, J. M. Espi, E. J. Dede, and E. Sanchis-Kilders, "A bidirectional and isolated three-phase rectifier with soft-switching operation," *IEEE Transactions on Industrial Electronics,* vol. 52, no. 3, pp. 765-73, 2005.

[134] S.K. Mazumder, "A novel discrete control strategy for independent stabilization of parallel three-phase boost converters by combining space-vector modulation with variable-structure control," *IEEE Transactions on Power Electronics,* vol. 18, no. 4, pp. 1070-83, 2003.

[135] M. Cichowlas, M. Malinowski, M.P. Kazmierkowski, D.L. Sobczuk, P. Rodriguez, and J. Pou, "Active filtering function of three-phase PWM boost rectifier under different line voltage conditions," *IEEE Transactions on Industrial Electronics,* vol. 52, no. 2, pp. 410-19, 2005.

[136] J. Wu, F.C. Lee, D. Boroyevich, H. Dai, K. Xing, D. Peng, "A 100 kW high-performance PWM rectifier with a ZCT soft-switching technique," *IEEE Transactions on Power Electronics,* vol. 18, no. 6, pp. 1302-8, 2003.

[137] Y. Shtessel, S. Baev, and H. Biglari, "Unity power factor control in 3-phase AC/DC boost converter using sliding modes," *IEEE Transactions on Industrial Electronics,* vol. 55, no. 11, pp. 3874-82, 2008.

[138] T.-Sh. Lee, "Input-output linearization and zero-dynamics control of three-phase AC/DC voltage-source converters," *IEEE Transactions on Power Electronics,* vol. 18, no. 1, pp. 11-22, 2003.

[139] C. Xia, Q. Geng, X. Gu, T. Shi, and Z. Song, "Input-output feedback linearization and speed control of a surface permanent magnet synchronous wind generator with the boost-chopper converter," *IEEE Transactions on Industrial Electronics,* vol. 59, no. 9, pp. 3489-3500, 2012.

[140] A. Lidozzi, L. Solero, and F. Crescimbini, "Adaptive direct-tuning control for variable-speed diesel-electric generating units," *IEEE Transactions on Industrial Electronics,* vol. 59, no. 5, pp. 2126-34, 2012.

[141] M.A. Parker, C. Ng, and L. Ran, "Fault-tolerant control for a modular generator-converter scheme for direct-drive wind turbines," *IEEE Transactions on Industrial Electronics,* vol. 58, no. 1, pp. 305-15, 2011.

[142] D. Krahenbuhl, C. Zwyssig, and J.W. Kolar, "Half-controlled boost rectifier for low-power high-speed permanent-magnet generators," *IEEE Transactions on Industrial Electronics,* vol. 58, no. 11, pp. 5066-75, 2011.

[143] R. Dayal, S. Dwari, L. Parsa, "Design and implementation of a direct AC-DC boost converter for low-voltage energy harvesting," *IEEE Transactions on Industrial Electronics,* vol. 58, no. 6, pp. 2387-96, 2011.

[144] M. Kesraoui, N. Korichi, and A. Belkadi, "Maximum power point tracker of wind energy conversion system," *Renewable Energy,* Vol 36, pp. 2655-2662, 2011.

[145] E. Koutroulis, K. Kalaitzakis, "Design of a maximum power tracking system for wind-energy-conversion applications," *Energy Conversion Congress and Exposition,* pp. 2370-2377, 2010.

[146] E. Tedeschi, M. Molinas, M. Carraro, and P. Mattavelli, "Analysis of power extraction from irregular waves by all-electric power take off," *IEEE Transactions on Industrial Electronics,* vol. 53, no. 2, pp. 486-494, 2011.

[147] M. Gopinath and D. Yogeetha, "Efficiency analysis of bridgeless PFC boost converter with the conventional method," *International Journal of Electronic Engineering Research,* vol. 1, no. 3, pp. 213-21, 2009.

[148] Harmonic Current Emissions Guidelines to the standard EN 61000-3-2, *European Power Supply Manufacturers Association,* 2010.

[149] A. maravandi, "Using algebraic screw in the car suspension system," *Ph.D. Report,* 2012.

[150] L. Segal and L. Xiao-Pei, "Vehicular resistance to motion as influenced by road roughness and highway alignment," *Australian Road Research,* vol. 12, no. 4, pp. 211-222, 1982.

[151] M.G. Fodor and R. Redfield, "The variable linear transmission for regenerative damping in vehicle suspension control," *Vehicle System Dynamics,* vol. 22, pp. 1-20, 1993.

[152] C. Squatriglia, "High-tech shocks tum bumps into power," 2009, *http://www.1evantpower.com.*

[153] W.D. Jones, "Easy ride: Bose Corp. uses speaker technology to give cars adaptive suspension," *IEEE Spectrum,* vol. 42, no. 5, pp. 12-4, 2005.

[154] Y. Kawamoto, Y. Suda, H. Inoue, and T. Kondo, "Modeling of electromagnetic damper for automobile suspension," *Journal of System Design and Dynamics,* vol. 1, no. 3, pp. 524-35, 2007.

[155] J. Prudell, M. Stoddard, E. Amon, T.K.A. Brekken, and A. von Jouanne, "A permanent-magnet tubular linear generator for ocean wave energy conversion," *IEEE Transactions on Industry Applications,* vol. 46, no. 6, pp. 2392-400, 2010.

[156] CENTROID Servo Motor Dimensions, http://www.centroidcnc.com/servo-dimensions.htm.

[157] S.J. Chapman, *Electric Machinery Fundamentals*, Fourth Second Edition, McGraw-Hill, 2005.

[158] M.L. Husty and A. Karger, "Self-motions of Griffis-Duffy type parallel manipulators," *IEEE International Conference on Robotics and Automation,* pp. 7-12, 2000.

[159] A. Karger and M.L. Husty, "Classification of all self-motions of the original Stewart-Gough platform," *Computer-Aided Design,* vol. 30, no. 3, pp. 205-15, 2007.

[160] J.D. Robinson and M.J.D. Hayes, "The dynamics of a single algebraic screw pair," *Canadian Committee for the Theory of Machines and Mechanisms Symposium on Mechanisms, Machines, and Mechatronics,* pp. 1-12, 2011.

[161] S.C. Zhi and Z. Youqun, "Multi-objective optimization design of vehicle suspension based on Stackelberg," *IEEE International Conference on Natural Computation,* pp. 2783-7, 2010.

[162] B. J. Han, X.N. Gang, C.Y. Wan, W. Lu, and S.C. Zhi, "Multi-objective optimization design of passive suspension parameters based on collusion cooperation game theory," *IEEE World Congress on Intelligent Control and Automation,* pp. 118-25, 2010.

[163] R. Alkhatib, G. Nakhaie Jazar, M.F. Golnaraghi, "Optimal design of passive linear suspension using genetic algorithm," *Journal of Sound and Vibration,* vol. 275, no. 3-5, pp. 665-91, 2004.

[164] S. Chen, D. Wang, A. Zuo, Z. Chen, W. Li, and J. Zan, "Vehicle ride comfort analysis and optimization using design of experiment," *IEEE International Conference on Intelligent Human-Machine Systems and Cybernetics,* vol. 1, pp. 14-8, 2010.